ORNL/TM-2015/332

Oak Ridge National Laboratory

# Manufacturing Demonstration Facility: Low Temperature Materials Synthesis

David E. Graham

Ji-Won Moon

**June 30, 2015**

OAK RIDGE NATIONAL LABORATORY
MANAGED BY UT-BATTELLE FOR THE US DEPARTMENT OF ENERGY

## DOCUMENT AVAILABILITY

Reports produced after January 1, 1996, are generally available free via US Department of Energy (DOE) SciTech Connect.

**Website** http://www.osti.gov/scitech/

Reports produced before January 1, 1996, may be purchased by members of the public from the following source:

National Technical Information Service
5285 Port Royal Road
Springfield, VA 22161
***Telephone*** 703-605-6000 (1-800-553-6847)
***TDD*** 703-487-4639
***Fax*** 703-605-6900
***E-mail*** info@ntis.gov
***Website*** http://www.ntis.gov/help/ordermethods.aspx

Reports are available to DOE employees, DOE contractors, Energy Technology Data Exchange representatives, and International Nuclear Information System representatives from the following source:

Office of Scientific and Technical Information
PO Box 62
Oak Ridge, TN 37831
***Telephone*** 865-576-8401
***Fax*** 865-576-5728
***E-mail*** reports@osti.gov
***Website*** http://www.osti.gov/contact.html

This report was prepared as an account of work sponsored by an agency of the United States Government. Neither the United States Government nor any agency thereof, nor any of their employees, makes any warranty, express or implied, or assumes any legal liability or responsibility for the accuracy, completeness, or usefulness of any information, apparatus, product, or process disclosed, or represents that its use would not infringe privately owned rights. Reference herein to any specific commercial product, process, or service by trade name, trademark, manufacturer, or otherwise, does not necessarily constitute or imply its endorsement, recommendation, or favoring by the United States Government or any agency thereof. The views and opinions of authors expressed herein do not necessarily state or reflect those of the United States Government or any agency thereof.

**ORNL/TM-2015/332**

Advanced Manufacturing Office

# MANUFACTURING DEMONSTRATION FACILITY: LOW TEMPERATURE MATERIALS SYNTHESIS

**Lead Authors**
David E. Graham
Ji-Won Moon

**Co-Authors**
Beth L. Armstrong
Panos G. Datskos
Chad E. Duty
Ryan Gresback
Ilia N. Ivanov
Christopher B. Jacobs
Gerald E. Jellison
Gyoung Gug Jang
Pooran C. Joshi
Hyunsung Jung
Harry M. Meyer III
Tommy J. Phelps

Date Published: June 30, 2015

Prepared by
OAK RIDGE NATIONAL LABORATORY
Oak Ridge, TN 37831-6283
managed by
UT-BATTELLE, LLC
for the
US DEPARTMENT OF ENERGY
under contract DE-AC05-00OR22725

## CONTENTS

## LIST OF FIGURES

# LIST OF TABLES

# ACRONYMS

| | |
|---|---|
| ACS | Average Crystallite Size |
| AMO | Advanced Manufacturing Office |
| APRA-E | Advanced Research Projects Agency - Energy |
| CNMS | Center for Nanophase Materials Science |
| Cys-S | Cysteine-Sulfide complex |
| CZTS | Copper-zinc-tin sulfide |
| DOE | Department of Energy |
| EERE | Energy Efficiency & Renewable Energy |
| EERE | Office of Energy Efficiency and Renewable Energy |
| FA | Formamide |
| FL | Fluorescence |
| FTIR | Fourier Transform Infrared Spectroscopy |
| $H_c$ | Coercivity |
| HEPA | High-Efficiency Particulate Air |
| HEPES | *N*-(2-Hydroxyethyl)piperazine-N'-(2-ethanesulfonic acid) |
| LSPR | Localized Surface Plasmonic Resonance |
| MDF | Manufacturing Demonstration Facility |
| MOPS | 3-(*N*-Morpholino)propanesulfonic acid |
| $M_s$ | Saturated magnetization |
| NC | Nanocrystal |
| NF | NanoFermentation |
| NIR | Near-Infrared |
| NP | Nanoparticle |
| NTA | Nitrilotriacetic Acid |
| OA | Oleic Acid |
| OM | Oleylamine |
| ORNL | Oak Ridge National Laboratory |
| PCT | Patent Cooperation Treaty |
| PEG | Polyethylene Glycol |
| PL | Photoluminescence |
| PVP | Poly(vinylpyrrolidinone) |
| QD | Quantum Dot |
| RGB | Red, Green, and Blue |
| RSS | Research Safety Summary |
| SDS | Sodium Dodecyl Sulfate |
| SEM | Scanning Electron Microscopy |
| SME | Subject Matter Expert |
| SS | Stainless Steel |
| SSL | Solid State Lighting |
| TEM | Transmission Electron Microscopy |
| UV | Ultraviolet |
| XPS | X-ray Photoelectron Spectroscopy |
| XRD | X-Ray Diffractometer |

# ACKNOWLEDGEMENTS

This Oak Ridge National Laboratory (ORNL) Manufacturing Demonstration Facility (MDF) project was funded by the US Department of Energy (DOE), Office of Energy Efficiency and Renewable Energy (EERE) Advanced Manufacturing Office (AMO). This project was managed as CPS Agreement Number: 24764. The lead organization was the Oak Ridge National Laboratory (ORNL). The project duration was from January 23, 2012 through June 30, 2015.

Other project partners included: Ferro Corp., DuPont Corp., Top Five, Inc., and NanoElements LLC.

We thank Angela Blankenship, Craig Blue, Jessica Casey, Alan Liby, Jennifer Palmer, William Peter and Hiram Rogers for their excellent assistance managing the MDF project, and Tommy Phelps for vision and leadership in launching the low-temperature materials synthesis project and designing the pilot plant.

# EXECUTIVE SUMMARY

The Manufacturing Demonstration Facility (MDF) low temperature materials synthesis project was established to demonstrate a scalable and sustainable process to produce nanoparticles (NPs) for advanced manufacturing. Previous methods to chemically synthesize NPs typically required expensive, high-purity inorganic chemical reagents, organic solvents and high temperatures. These processes were typically applied at small laboratory scales at yields sufficient for NP characterization, but insufficient to support roll-to-roll processing efforts or device fabrication. The new NanoFermentation processes described here operate at a pilot scale at a low temperature (~60 $^{\circ}$C) in low-cost, aqueous media using bacteria that produce extracellular NPs with controlled size and elemental stoichiometry. Up-scaling activities successfully demonstrated high NP yields and quality in a 900-L pilot-scale reactor, establishing this NanoFermentation process as a competitive biomanufacturing strategy to produce NPs for advanced manufacturing of power electronics, solid-state lighting and sensors.

This low-temperature materials synthesis project included three main objectives: 1) Develop new products using low temperature NanoFermentation processes; 2) Expand the NanoFermentation platform technology; and 3) Upscale NanoFermentation to industrial pilot scale. Tasks completed for each objective markedly advanced the field of NP biomanufacturing and demonstrated excellent productivity for DOE-relevant applications including ferrites and ferro-fluids (metal-doped magnetite), solid-state lighting (metal sulfides and gallates) and semiconductors or gas sensors (metal oxides).

The low-temperature NanoFermentation syntheses produced a series of high-value metal sulfide NPs and their corresponding oxides, which can form n- and p-type semiconductors and substrates for gas sensors. ZnS NPs were produced in pure form (>160 g/month), as well as Cu(0.5-0.8%) and Ag-doped forms for luminescence applications including solid state lighting. This method also produced CuS, NiS, CoS, and SnS as well as highly luminescent CdS NPs at a rate > 330 g/month. Metal-substituted Zn-gallate NPs were produced at rates > 5 g/month, and all three binary phases of copper-zinc-tin sulfide (CZTS) were produced in > 5 g batches that were shared with an industrial collaborator. Finally, a new series of magnetite NPs substituted with Co, Mn, Gd or Ho ions was produced for new materials requiring low Curie-temperature magnetites. New compositions of Zn-doped magnetite NPs were prepared as precursors for an innovative project to create strong permanent iron nitride magnets.

The NanoFermentation platform was expanded to produce elemental Cu NPs, with excellent crystallite size control and resistance to surface oxidation using chelators and surfactants. New CoS (>0.5 g) and NiS (>1 g) NP batches were produced, along with Cd particles > 1 g. These tasks also developed methods for the controlled oxidation of metal sulfides to form ZnO, a wide bandgap p-type semiconductor, as well as CuO and $SnO_2$. Organic capping agents added to the reactors during NP formation constrained crystallite size and substantially reduced NP agglomeration.

A pilot plant containing 100-L and 900-L bioreactors was constructed for this project to determine whether NanoFermentation could be scaled up to commercially relevant production rates while maintaining product quality and yields. New methods of pasteurization, temperature and pH control and NP product recovery were developed in this plant, successfully upscaling the bench-scale synthesis of representative zinc sulfides while reducing the relative production costs. Three consecutive batches from the 100-L reactor produced > 50 g ZnS each, with highly reproducible crystallite sizes. These excellent yields encouraged scaling to 900 L, where > 500 g ZnS NPs were produced. Innovations in coupling the 100-L and 900-L reactors accelerated NP production, while automatic pH adjustment dramatically reduced the cost of chemicals required for production.

These tasks produced materials that we shared with the MDF roll-to-roll processing team and ARPA-e project collaborators, as well as commercial partners from DuPont, TopFive and NanoElements. In addition to a strong list of peer-reviewed publications in widely cited journals, this project produced a series of patents, patent applications and invention disclosures that will support commercialization. Future projects may build on a new process for NP formation that used the hydrogen sulfide waste stream from microbial growth to produce high-quality, concentrated metal sulfide NPs in a second, smaller reactor while reducing hazardous waste to 1-2% of the volume from previous reactors. This technology opens the door to producing new classes of NPs with greater control over surface coatings, which directly affect particle size, agglomeration and functionality.

This report describes the chronological development of an efficient, scalable NP production process through three major objectives in this MDF project. These biological systems used low-cost chemicals, low temperatures, and aqueous media to make precursors for n- and p-type semiconductor NPs, substituted gallates for optoelectronics, substituted magnetites for iron nitride magnets, and quantum dots for sensors and optoelectronics. Twelve new nanomaterials were produced using NanoFermentation in this project, and nine previously produced nanomaterials were up-scaled or enhanced during this period (Table E-1). Future projects can build on these innovations to control the purity and surface properties of NP products and optimize particle compositions and bandgaps for specific applications.

**Table E-1. Summary of new nanoparticles manufactured by NanoFermentation.**

| Nanoparticles | Maximum scale of production | Max. reactor volume | Average crystallite size (ACS*) | Property[#] | Collaborator /Industrial partner | Application |
|---|---|---|---|---|---|---|
| **Substituted Magnetites** | | | | | | |
| Cobalt-doped magnetite ($Co_{0.3}Fe_{2.7}O_4$) | 25 g (wet) | 1 L | 25-50 nm | lower Curie temperature | ORNL Additive Manufacturing | Polymerization<br>Magnetism |
| Manganese-doped magnetite ($Mn_{0.6}Fe_{2.4}O_4$) | 20 g (wet) | 1 L | 25-50 nm | lower Curie temperature | ORNL Additive Manufacturing | Polymerization<br>Magnetism |
| Zinc-doped magnetite ($Zn_{0.6}Fe_{2.4}O_4$) | 3 × 100 g | 30 L | ~20 nm | magnetism | NPMR | Magnetic |
| Zinc-doped magnetite (Zn 1%, 5% and 10%) | 2 × ~3 g | 500ml | 15.3-30.7 nm,12.3-25 nm<br>12.6-17.7 nm | Precursor for<br>Iron nitride | ARPA-e project: AMC, Univ. of Minnesota, ORNL | Magnetic, memory |
| Ga- and Ho-doped magnetites | < 5 g | 1 L | 25-50 nm | lower Curie temperature | ORNL MDF | Polymerization<br>Magnetism |
| **Metals** | | | | | | |
| Elemental cadmium (electrochemical) | 1.07 g | 250mL | | Anti-corrosion | | Batteries, aeroplane |
| Elemental copper (capped) | 0.1 – 0.2 g | 1 L | 28 - >100 nm | Electrical conductivity | | Electric board, capacitors |
| **Metal Gallates** | | | | | | |
| Co-doped Zinc gallate | 14.8 g | 24 L | 3.0-3.4nm | Blue emission | Testing at PKNU<br>MDF R2R | Phosphor |
| Cr-doped Zinc gallate | 13.9 g | 24 L | 3.0-3.4nm | Red emission | Testing at PKNU<br>MDF R2R | Phosphor |
| Mn-doped Zinc gallate | 14.3 g | 24 L | 3.0-3.4nm | Green emission | Testing at PKNU<br>MDF R2R | Phosphor |

| Nanoparticles | Maximum scale of production | Max. reactor volume | Average crystallite size (ACS) | Property | Collaborator /Industrial partner | Application |
|---|---|---|---|---|---|---|
| **Metal Sulfides** | | | | | | |
| Cadmium sulfide (capped) | >45 g | 24 L | 4-5 nm | Emission | Testing | Quantum dots |
| Cobalt sulfide | 0.67 g | 1 L | | Precursor of metal oxide | TMDF R2R | Insulator, resistor |
| Copper antimony sulfide | | < 50mL | | Thermoelectric | Testing | Thermoelectric |
| Copper sulfide | 13.1 g | 24 L | 12.3 nm | Binary CZTS component of photovoltaic | DuPont | photovoltaic |
| Nickel sulfide | 6.7-9.2 g | 24L | 6.7-7.3 nm | Precursor for NiO | MDF R2R | High temp. insulator,<br>NiO precursor |
| Tin sulfide | 17.1 g | 24 L | 10.2 nm | Binary CZTS component of photovoltaic | DuPont | Photovoltaic, SnO precursor |
| Zinc sulfide | 2 × 300 g<br>3 × 50 g | 900 L<br>100 L | 2-3 nm<br>2.1-2.2 nm | Emission | TopFive Inc., Nano-elements LLC, MDF R2R | Solid state light, ZnO precursor |
| Zinc sulfide (NTA-treated) | 5.8 g | 24 L | <5 nm | Enhanced emission | DuPont | Solid State Light<br>Flat display |
| Zinc sulfide (capped) | 33 g | 24 L | 2.5 nm | Enhanced emission | Testing | Quantum dots |
| **Substituted Zinc Sulfides** | | | | | | |
| Copper-doped ZnS (Cu 0.8%) | 0.5-1 g | 1 L | 6.5-10 nm | Green emission | MDF R2R | Flat display |
| Silver-doped ZnS (Ag 5% and 10%) | 22.3 g<br>57 g | 100L | 6.5 nm<br>2.2 nm | Antibacterial<br>Antifungal agent precursor | CNMS<br>Iowa State Univ.<br>Texas Tech Univ. | Gels, creams, wound dressing composites |

# 1. INTRODUCTION

## 1.1 PROJECT OBJECTIVE

The objective of this project was to develop and demonstrate low temperature (~60 °C) materials synthesis, characterization and process scaling of nanoparticles (NPs) by NanoFermentation (NF) using organisms that produce extracellular crystals with controlled size and stoichiometry. The tasks were designed to demonstrate pilot-scale nanoparticle production for DOE-relevant applications including ferrites and ferro fluids (metal doped magnetite), solid-state lighting (metal sulfides and gallates) and advanced battery technologies ($LiFePO_2$, $LiCoO_2$, $LiMgO_2$, and $LiFeO_2$). This effort was divided into three tasks:

Task 1. Low Temperature NanoFermentation Synthesis
    Producing nanoparticles for energy relevant applications including ZnS for solid state lighting, Zn-gallates for phosphors and other nanoparticles including kesterite
Task 2. Expansion of the NanoFermentation Platform
    Expanding the NanoFermentation platform by expanding $E_h$/pH conditions for nanoparticle formation.
Task 3. Upscale NanoFermentation to Industrial Pilot Scale
    Scale up nanoparticle production to a pilot-scale 900-L reactor

## 1.2 PROJECT BACKGROUND

NanoFermentation represents a fundamentally new approach for producing extremely fine, highly crystalline powders of various materials. The process uses natural micron-sized bacteria that synthesize large quantities of nanoparticles external to the cells at or near room temperature. NanoFermentation technology is a promising alternative, green chemistry synthesis process for nanotechnology, and a number of applications could benefit from this enabling technology. The overall objective was to develop a low cost approach to the mass production (kg samples) of highly uniform size controlled energy- and DOE-relevant NPs that cover wide applications including magnetic, semiconducting, phosphor, photovoltaic, catalytic, and more.

Metal reducing bacteria have been known for years, and many such species have adapted to anaerobic environments ranging from the Antarctic to the ocean floor to deep subsurface geologic structures. Samples obtained 10,000 feet below ground surface in the Taylorsville Triassic Basin exhibited thermophilic metal reduction. Similar *Thermoanaerobacter ethanolicus* strains were then observed in core samples from a 1994 Piceance Basin project. The primary paper describing these results was published in *Science* in 1997, based on basic research funded by the DOE Subsurface Science Program and the DOE Geosciences Research Program. Because the electron transfer process employs specialized proteins such as metal-reductases, it was long believed that the bacteria will produce pure magnetite (the presence of pure magnetite in a rock layer is considered a possible indicator that the rock is of biogenic origin). Work under the DARPA BioMagnetics program verified this important result. Furthermore, subsequent research with the thermophiles indicated that the microbially mediated process is suitable for incorporating other metals into magnetite. NanoFermentation: A Bioprocess for Manufacturing Inorganic Nanomaterials received a 2006 R&D 100 award in recognition of its potential.

Our discovery that the bacteria can make mixed metal oxides has created a breakthrough for large-scale synthesis of nanoscale powders. Nanoparticles have been produced from many different metal oxides and mixed metal oxides, including: iron, cobalt, nickel, zinc, chromium, manganese, palladium, and rare earths (Nd, Gd, Er, Ho, and Tb). In addition, we have demonstrated that these bacteria can reduce other electron-accepting heavy metals such as chromium, cobalt and uranium, enabling the large-scale production of novel materials at the nanoscale. NanoFermentation ranks as a fundamentally new, potentially disruptive, process compared to traditional inorganic methods such as sol-gel and chemical vapor decomposition and it has definite advantages in terms of control and scalability. Two key aspects of the process are evident: First, the amount of product is very large compared to the cellular mass. Second, the product is formed externally to the cell. We have demonstrated an ability to control particle size and morphology by several means including temperature, incubation time, and choice of electron donor or additives.

The most immediate applications of NanoFermentation are based on its demonstrated ability to make highly crystalline nanoscale particles of doped ferrites. The powders can be used for magnetic media, ferrofluids, magnetorheological media, radar absorbant coatings, and xerographic toner. NanoFermentation can also create many other mixed transition metal oxides including compounds of cobalt, chromium, manganese, zinc, uranium, and the rare earths. Another possible application includes forward osmosis for water purification. In this application, the bacteria synthesize coated magnetic nanoparticles that are designed to bind and magnetically tag any bacterial component in a sample of water. It then becomes a simple matter of magnetic separation to remove all bacteria from any water sample. Clearly, due to the size of the particles, there are a number of potential applications in terms of additives beyond the traditional approach of adding magnetic NPs to paint for stealth. Specific control of the additives can potentially act as a catalyst in paints using different oxides so as to enable immediate decontamination of chemical warfare agents. The bacteria’s ability to survive and operate in hostile (high temperature, high radiation) environments may enable the development of new nanoscale fuels (e.g. coated U-238 nanoparticles).

Recent experiments have uncovered the bacteria’s ability to synthesize other forms of nanoparticles beyond ferrites. As an example, preliminary analysis has shown that these same bacteria are capable of synthesizing CdS and ZnS semiconducting materials. If the bacteria can synthesize these materials in the sub-10 nm range with a similar efficiency as has been demonstrated with the ferrites, this will enable a complete game changer in terms of low cost scalable green synthetic process. While there are other approaches for the synthesis of NPs, NanoFermentation represents a new disruptive manufacturing technology in terms of low cost, highly consistent nanoparticle synthesis.

# 2. RESULTS AND DISCUSSION

## 2.1 LOW TEMPERATURE NANOFERMENTATION SYNTHESIS

This task was initiated in January 2012 to investigate nanoparticle production most important to industrial applications while gaining an understanding of the bounds and constraints of NanoFermentation (NF). Subtasks explored precursors and processes for producing innovative high performance products and developed new DOE-relevant NPs using NanoFermentation.

### 2.1.1 Produce ZnS and Other Sulfide Nanoparticles by NanoFermentation

The first product from NanoFermentation was ZnS NPs, and three distinct batches of 0.5–1 g of ZnS were provided to the MDF roll-to-roll processing team for evaluation in the area of solid-state lighting (SSL). These samples included ZnS as well as Cu-doped ZnS with the Cu dopant concentration ranging from 0.5–8% to examine if Cu inclusion caused a shift in the fluorescence spectrum. There was a significant shift to longer wavelengths with dopants up to 2% Cu with an observed red-shift in fluorescence from blue (~340 nm) to green (up to ~ 400nm) (Figure 1-1a), suggesting a desired shift in fluorescence that could be useful in SSL. Among pure ZnS batches, variations in the doping routine were examined as well as incubation times of 5 or 10 days. With respect to dosing, single doses of 5 mM $ZnCl_2$ resulted in the desired smaller particle sizes of 6-7 nm, compared to >7 nm sizes resulting from multiple doses of $ZnCl_2$. Five days of incubation for CdS NP production resulted in smaller particles, while 10 days incubation exhibited a larger particle size consisting of a core and shell-like coating as shown in Figure 1-1b where the outer molecular layers are at different planes from the initial core structure.

In other experiments we examined future potential candidate NF processes such as binaries of copper indium gallium selenide (CIGS) of interest to our industrial partner, Ferro. Precipitates have been formed from Cu-S, and using Cu(II) appeared better than Cu(I). However, indium and gallium precipitates appear as $In_2Se_3$ and $Ga_2S_3$ rather than the desired InS and GaS forms.

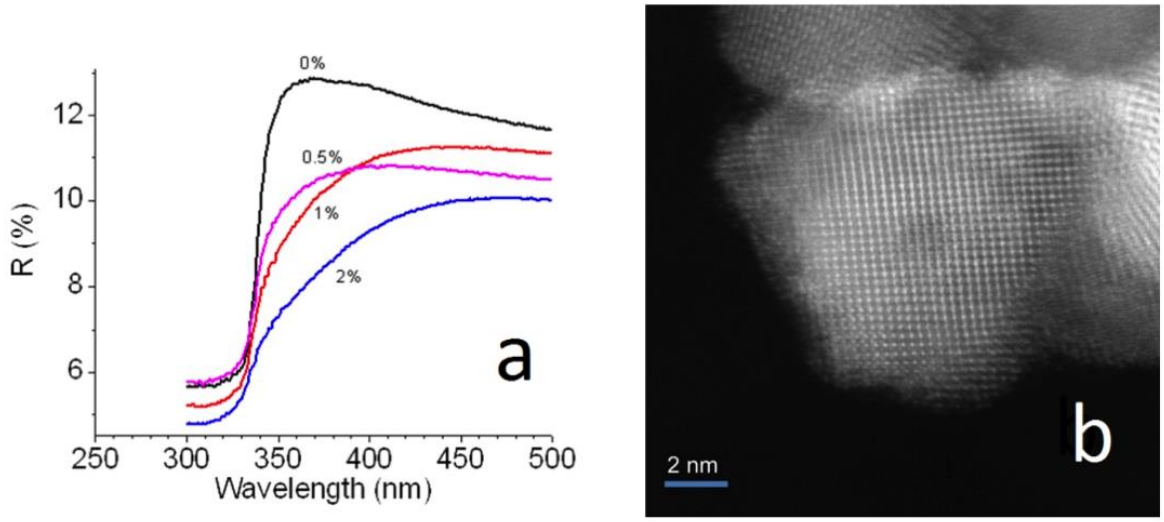

**Figure 1-1. a) Red-shift of optical band gap of ZnS:Cu with increased Cu dosing on diffuse reflectance and b) Transmission electron microscopy identified a core/shell structure of cadmium sulfide NPs**

### 2.1.2 Produce ZnS gallate or additional metal sulfide nanoparticles

NanoFermentation technology was used to produce Zn-gallates at rates of 5 g/month. Freeze dried samples of each red, green, and blue-emitting Zn-gallate phosphors had masses of 1.9, 2.0, and 1.7 g, respectively (Figure 1-2a), produced in 3-L batches after only one week of incubation. The milestone was exceeded with production being 6 g during 1 week. Freeze dried samples were sintered and mixing ratio was considered to produce white light in 2.1.3 section. Red, green, and blue (RGB) phosphors were also produced and stored in deionized water after washing. These were also >5 g quantities produced in a week demonstrating repeatability of the milestone. As a side note, Mn(4%)-substituted Ga-phosphor had a slightly lower yield, so another green light source was added by producing Mn(4%) replacing Zn (Figure 1-2b). This represented a new green phosphor for future consideration.

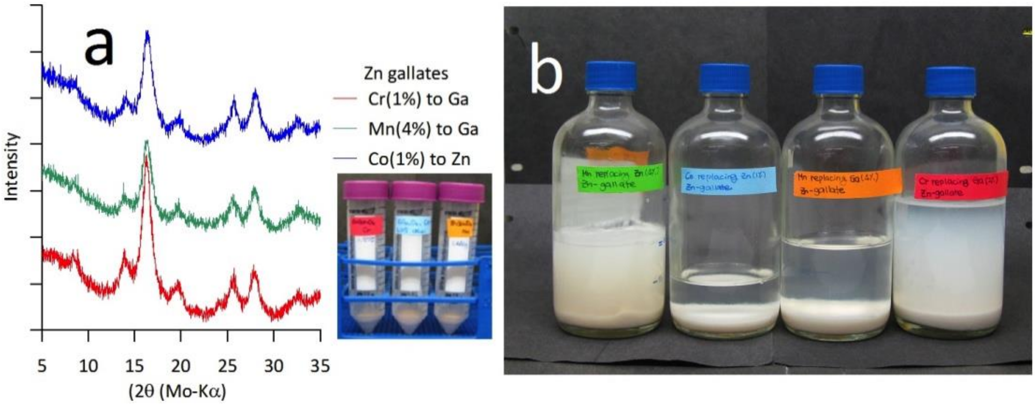

**Figure 1-2. Metal-substituted zinc gallates to produce RGB and white colors**

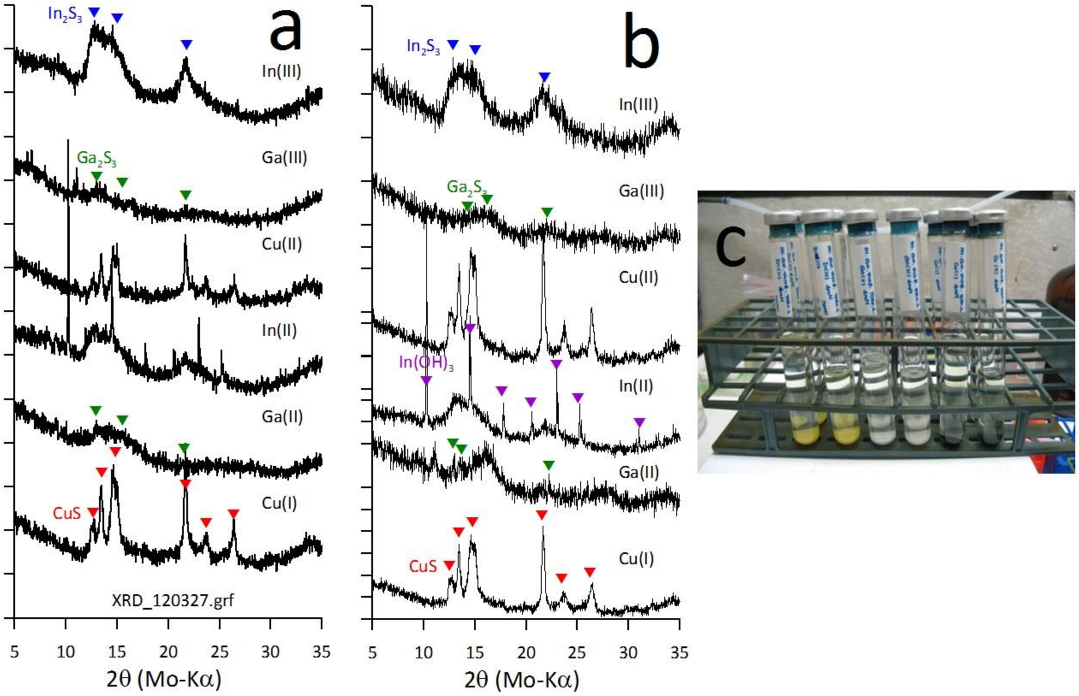

**Figure 1-3. Binary composition of CIGS. a) discrete pulsed dosing, b) single impact dosing, and c) nanomaterials in culture tubes**

In other experiments we examined future potential candidate NF processes such as binaries of CIGS. Both discrete pulsed and impact single dosing were applied (Figure 1-3a and b, respectively), and valence-varied metal salts were examined such as In(II) and In(III), Ga(II) and Ga(III), and Cu(I) and Cu(II). Among these ions, In(III) produced a phase close to $In_2S_3$ but In(II) precipitated unexpected indium hydroxides. Regardless of copper source and dosing method CuS was successfully produced.

### 2.1.3 Characterize nanoparticle size and chemistry

Nanoparticles produced using NanoFermentation (Zn sulfides and gallates) were characterized in terms of size and chemistry. The properties were appropriate for functional thin films including 6–10 nm sizes, desired fluorescence peaks, and good suspension in 10% aqueous suspensions for Roll-to-Roll processing tasks.

Low temperature zinc-sulfide synthesis was accomplished in scalable batches from 10 mL to 24 L followed by successful concentration into 10 and 15% aqueous inks (Figure 1-4), with the 10% inks proving to be better for thin film development. Average crystallite sizes (ACS) of the zinc sulfide produced biologically using NanoFermentation (Bio-ZnS) could be controlled by dosing concentrations as shown in Figure 1-5a with very clean XRD spectra indicating high quality and high purity product with ACS estimates of 2–12 nm. As shown in Figures 1-5b and c the particles exhibited sizes of 4 nm to 16 nm as determined by TEM, which was in good agreement with the XRD estimates.

**Figure 1-4. Scale-up experiment for bio-ZnS from 10mL to 24L (a-d) and 10% and 15% ink (e)**

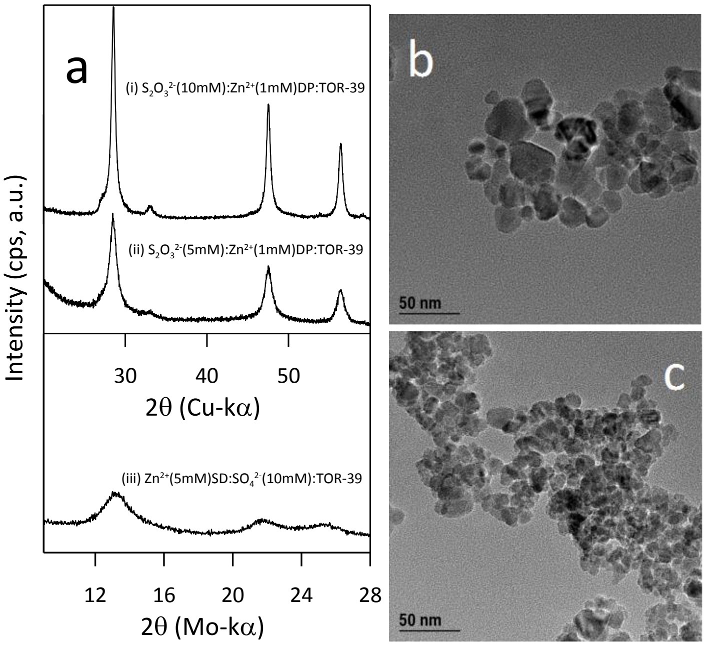

**Figure 1-5. a) X-ray diffraction patterns for bio-ZnS depending on dosing method, b) and c) TEM image from sample i and ii of part a.**

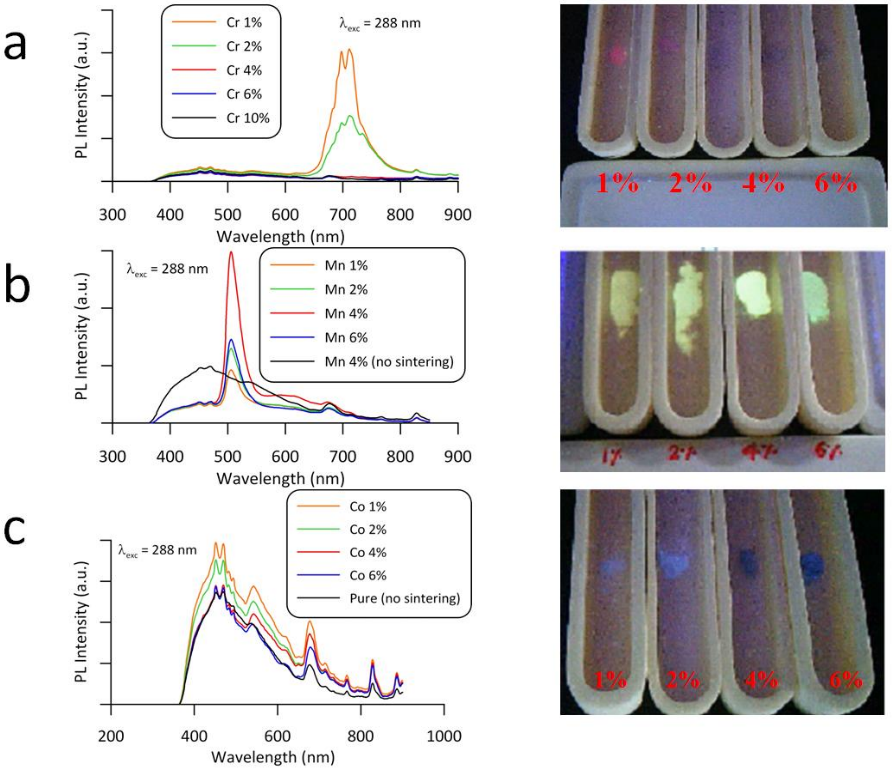

**Figure 1-6. Biologically produced zinc gallates doped with various metals emitted a) red, b) green, and c) blue photoluminescence, illustrated by spectra and photographs**

Nano-dimensioned zinc gallate phosphors emitting RGB colors were synthesized by doping various transition metals (Figure 1-6). Precursor compositions containing Cr (1–10%) replacing Ga led to red colors.  When Mn (1–6%) was used to replace Ga the nanoparticles produced a green luminescence, and Co replacing Zn (1–6%) produced blue luminescence. The metal-doped bio-zinc gallate NPs were 3–6 nm in size, emitted light with the expected peaks, and were reproducibly produced at rates of more than 5g/month in the last quarter. The doped NPs with highest efficiency RGB emission (Figure 1-7) were selected for mixing to produce white light for solid state lighting.

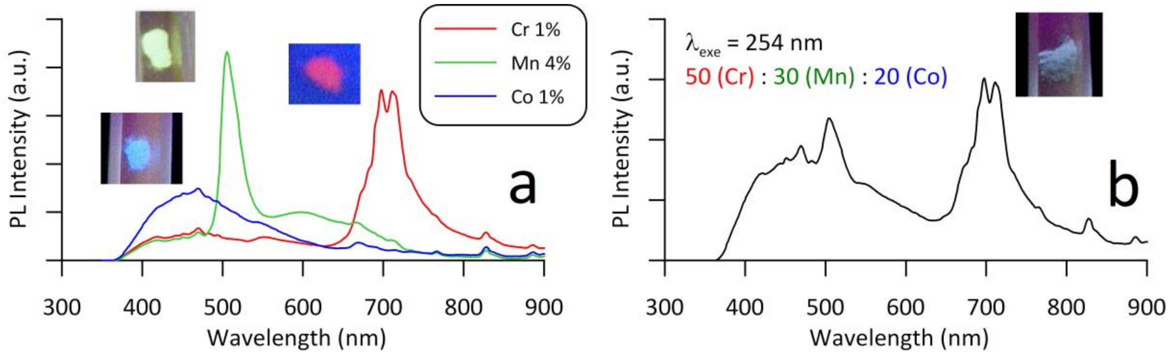

**Figure 1-7. Photoluminescence spectra of a) most efficient metal-doped zinc gallate emitting RGB colors and b) their one mixing example**

### 2.1.4 Demonstrate up-scaling to 10 g/month batch size for nanoparticles

Up-scaling in bench-size bioreactors was demonstrated, producing >11 g batches of ZnS NPs in only three days at more than twice the expected yield. The NP properties remained consistent with scaling, making them appropriate for thin films including 6–10 nm sizes, desired fluorescence peaks, and suspension into 10% aqueous suspensions for thin film processing tasks. Smaller sized nanoparticles are needed to enhance quantum efficiency or improve coating and deposition properties for device fabrication.

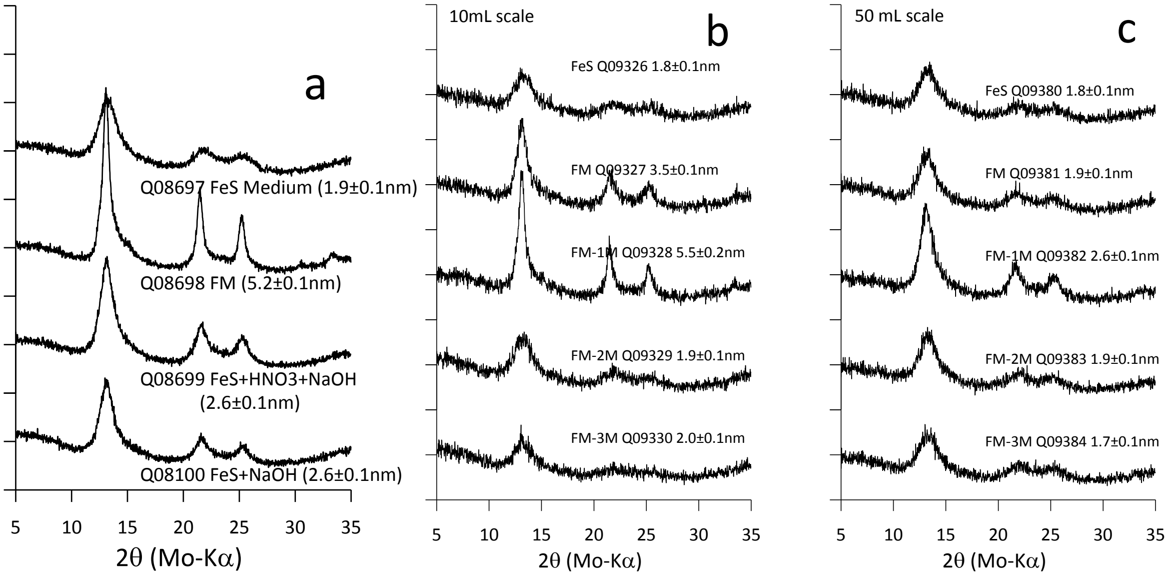

**Figure 1-8. X-ray diffraction patterns of ZnS from various buffer conditions. a) Controlled FeS medium with HEPES compared to FM medium, b) and c) controlled FM medium with basic or acidic MOPS in 10 mL and 50 mL, respectively, compared to FeS medium**

The media used to grow bacteria and produce NPs typically contains organic buffer salts to control the pH decrease caused by organic acids produced during fermentation. These buffers can affect NP size, yield and agglomeration in aqueous solution. ZnS NPs (5.2 nm ACS) from FM medium containing 3-(*N*-morpholino)propanesulfonic acid (MOPS) pH buffer exhibited a larger ACS compared to NPs (1.9–2.6 nm) from FeS medium containing 4-(2-hydroxyethyl)-piperazine-1-ethanesulfonic acid (HEPES) pH buffer (Figure 1-8a). We then compared the effects of addition MOPS buffer as the free acid (MOPS-$H^+$) or basic sodium salt (MOPS-$Na^+$).

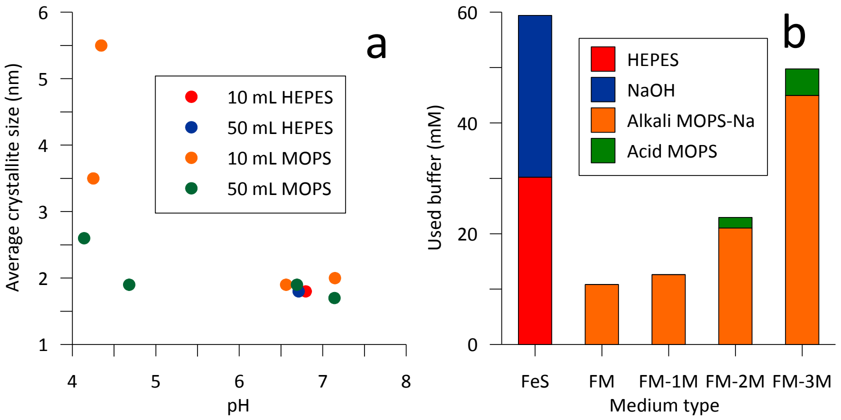

**Figure 1-9. a) The relationship between final pH and ACS, b) used buffer contents and types**

Replicate batches of 10 mL and 50 mL exhibited that different buffer formulations can produce ZnS NPs with the same small ACS observed in FeS medium (Figure 1-8b and c). A plot of pH vs. ACS indicates an inverse relationship between the two variables (Figure 1-9a). To make ZnS NPs we dose 5 mM $ZnCl_2$ stock solution into media that contains 10-60 mM organic buffer (Figure 1-9b). Therefore we can surmise that the effects of HEPES and MOPS were primarily due to their roles as pH buffers. In Figure 1-9a, samples which had final pH values between 6.7-7.2 cluster together with 2 nm ACS NPs regardless of buffer. However, when the pH decreased below 4.5, the ZnS size increased up to 6 nm (200% increase), which indicated that the final medium pH is key to controlling the ACS.

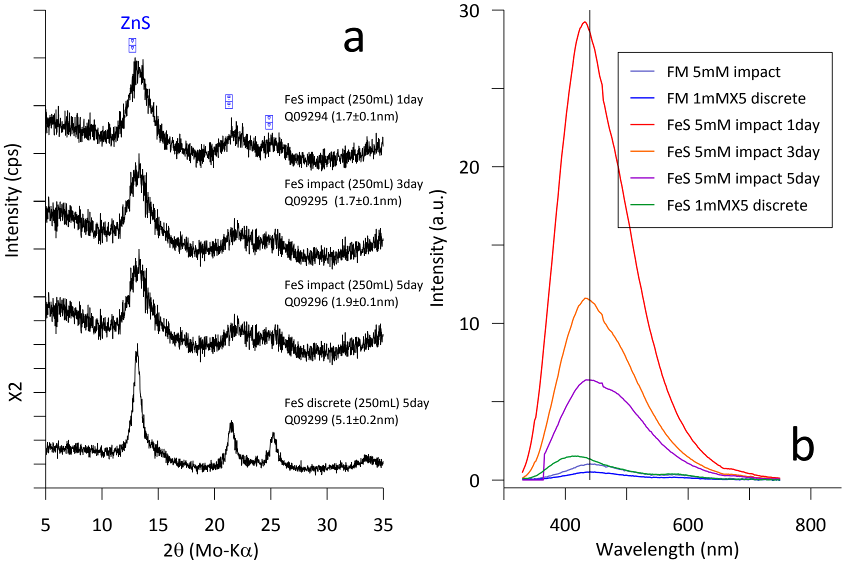

**Figure 1-10. a) X-ray patterns and b) photoluminescence of ZnS nanoparticles derived from different dosing methods and incubation times**

We next examined the effects of incubation time and dosing methods on ACS and luminescence properties. The initial 2.1 g/L/month yield was based on 2 days of cell growth, followed by 5 days incubation after 5 mM $ZnCl_2$ (impact) dosing or 1mM $ZnCl_2$ 1mM/day for 5 days (discrete) doing. Therefore we compared dosing methods to FeS medium as well as the effects of impact dosing at different time schedule. Based on XRD results, impact dosing influenced ACS so that irrespective of incubation days most samples exhibited around 2 nm size compared to discrete dosing of 5 nm (Figure 1-10a). However, the photoluminescence from these samples dramatically changed depending on incubation time (Figure 1-10b). This might be caused by crystal growth over time even though ACS values are similar. TEM analysis demonstrated that the ACSs were similar, 5.5–6.5 nm, but the size distribution and standard deviation of sizes became wider over time (Figure 1-11). We then produced 11.8 g ZnS from a 24 L reactor in 3 days, which is equivalent to 4.9 g/L/month, and we achieved more than 100% increased yield with enhanced luminescent properties.

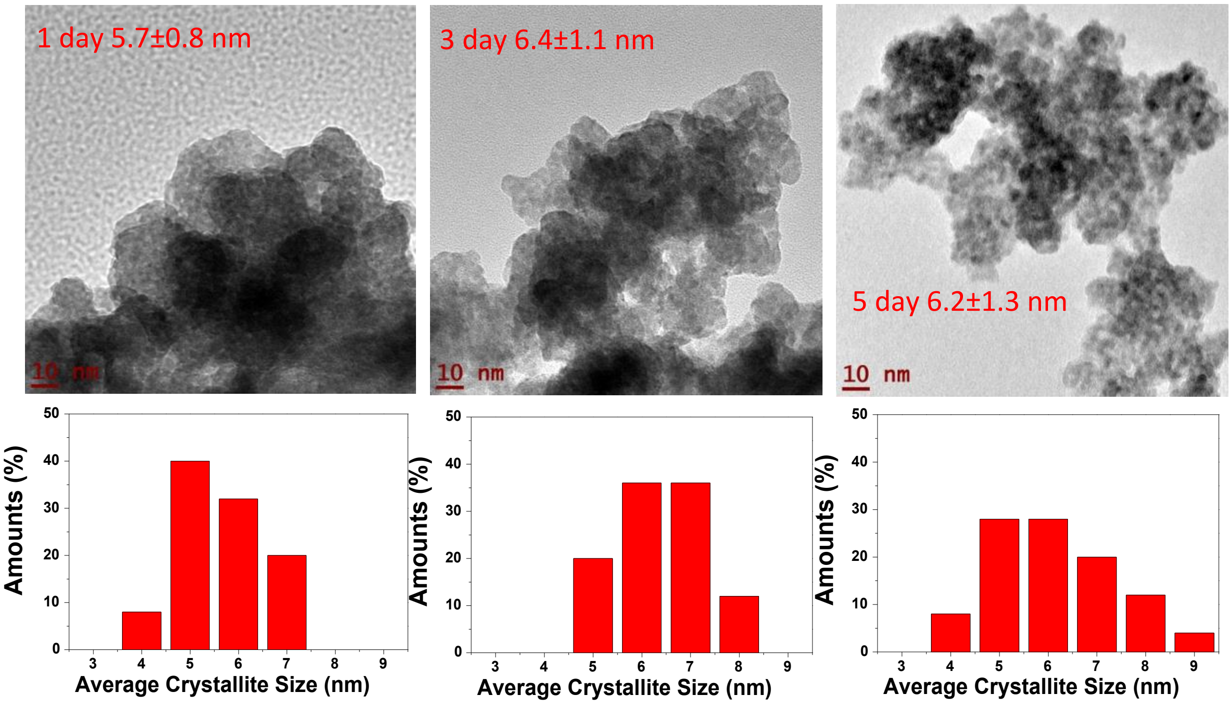

**Figure 1-11. TEM analysis of biotic ZnS nanoparticles produced at different incubation time in impact dosing for 5 days**

### 2.1.5 Identify 2-5 candidate particles for FY2013 investigation

An additional Task 1 milestone was to identify 2–5 candidate nanoparticles for detailed bench-scale production and investigation in FY13. ZnO NPs, first produced in Task 2 activities, was selected as one candidate. Its high fluorescence coupled with small crystallites makes it a promising material for producing thin-film electronics and capacitors. ZnS NPs produced by NanoFermentation were oxidized to make fine crystallites of ZnO. The other candidates for bench scale investigation in FY13 were metal sulfides for energy conversion such as tin sulfide, copper sulfide, copper tin sulfide (Figure 1-12) in addition to well-characterized zinc sulfide. A number of industrial companies have been working to produce these metal sulfide nanoparticles with the desired stoichiometries. We observed evidence of copper sulfide production by employing combinations of media composition and pH buffering capacity. Tin sulfide exhibited an unknown impurity.

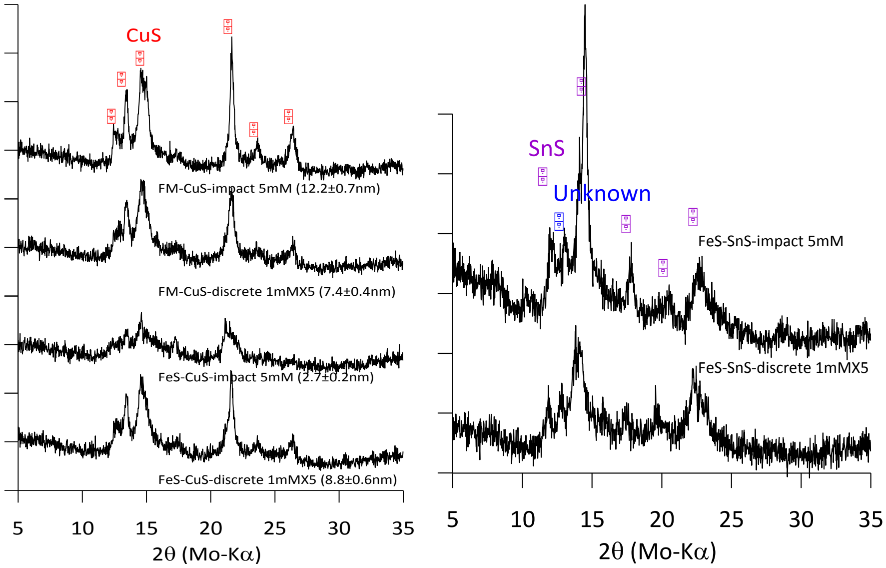

**Figure 1-12. X-ray diffraction patterns of copper sulfide and tin sulfides**

Surfactants had been used previously for both NF and conventional abiotic chemical syntheses to enhance crystallite properties and limit agglomeration. However, we additionally applied high-energy sonication using smaller diameter sonication probe tips, (2 mm and 6 mm diameter) to obtain more dispersed ZnS nanoparticles using a cycle composed of 1 second on- and 1 second off-duty at >100 watt/20 KHz for 5 min. After 20 hr, suspensions of all the sonicated samples including a control sample without surfactant maintained their optical densities, indicating the NPs resisted agglomeration and precipitation. The most turbid samples were selected for particle size analysis (Figure 1-13).

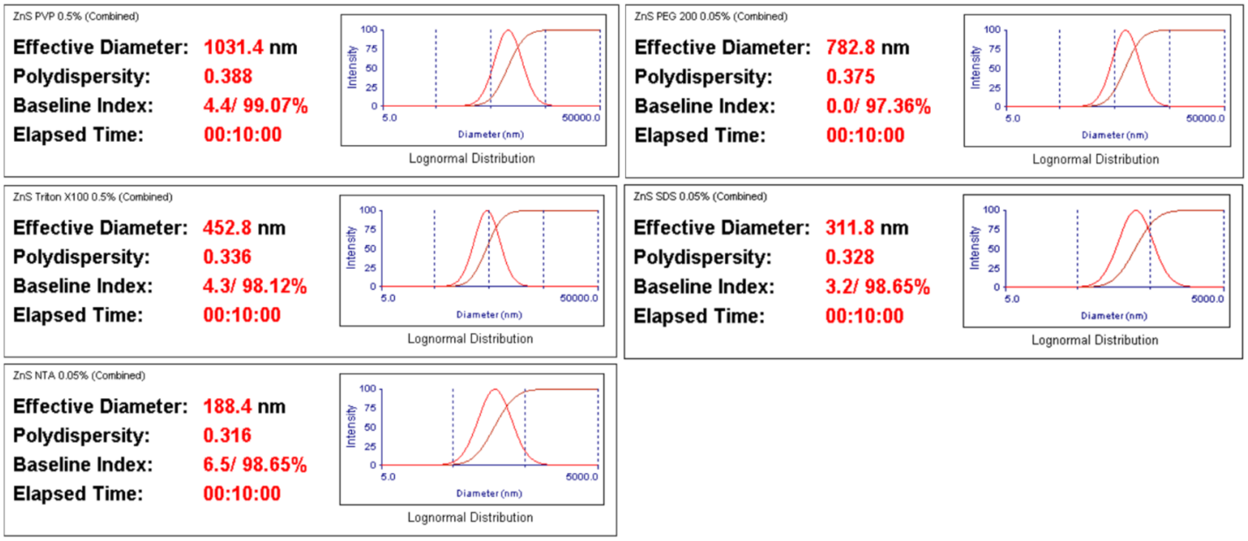
ZnS PVP 0.5% (Combined)

**Effective Diameter:** 1031.4 nm
**Polydispersity:** 0.388
**Baseline Index:** 4.4/ 99.07%
**Elapsed Time:** 00:10:00

ZnS PEG 200 0.05% (Combined)

**Effective Diameter:** 782.8 nm
**Polydispersity:** 0.375
**Baseline Index:** 0.0/ 97.36%
**Elapsed Time:** 00:10:00

ZnS Triton X100 0.5% (Combined)

**Effective Diameter:** 452.8 nm
**Polydispersity:** 0.336
**Baseline Index:** 4.3/ 98.12%
**Elapsed Time:** 00:10:00

ZnS SDS 0.05% (Combined)

**Effective Diameter:** 311.8 nm
**Polydispersity:** 0.328
**Baseline Index:** 3.2/ 98.65%
**Elapsed Time:** 00:10:00

ZnS NTA 0.05% (Combined)

**Effective Diameter:** 188.4 nm
**Polydispersity:** 0.316
**Baseline Index:** 6.5/ 98.65%
**Elapsed Time:** 00:10:00

**Figure 1-13. Particle size analysis of dispersed samples with surfactants and sonication. NTA–treated ZnS samples exhibiting average agglomerate size of 188 nm was better than PVP (1,031nm), PEG200 (783nm), Triton X100 (453 nm), or SDS (312 nm). NTA-treated ZnS remained stable even after 4.5 days**

To examine effects of sonication, surfactant, and pH, we varied each factor. We added 0.20 mL of a ZnS stock solution to 9.8 mL deionized water. The final concentration was ~0.06 wt.% of ZnS. The longer sonication was applied, the smaller the sizes of particles that were formed. Increasing nitrilotriacetic acid (NTA) concentration resulted in larger particle sizes. To evaluate the combined effect of surfactant and sonication, the original medium solution with ZnS was investigated as a control, compared with NTA-only, sonication only, and combined NTA-sonication. The pH also can impact agglomeration, so we added a fixed 0.125% NTA concentration and adjusted samples from an initial pH of 11.25 to pH values of 3.78, 4.53, 5.72, 6.73, 7.76, 9.05, and 10.04. After sonication the pH was slightly raised to 3.86, 5.08, 6.50, 7.44, 7.84, 8.96, and 9.96, respectively. After 30 min, acidic conditions resulted in immediate NP precipitation at pH 3.86 and 5.08. The particle sizes of the other samples above neutral pH were measured and shown below.

Copper antimony sulfide can be applied to thermoelectric devices to directly convert thermal gradients to electric current. This property could conserve energy from waste heat released by from hot sources. We investigated antimony oxidation state (either $Sb^{3+}$ or $Sb^{5+}$) and stoichiometry between copper and antimony at 50-mL medium scale. Copper sulfide was dominant when we used $Sb^{3+}$. A stoichiometric balance between $Cu^{2+}$ and $Sb^{5+}$ produced antimony oxide with either surplus or shortage of copper. An ideal molar ratio between $Cu^{2+}$ and $Sb^{5+}$ unexpectedly produced thermoelectric $Cu_3SbS_4$ with very little antimony oxide and minimal copper sulfide (Figure 1-14).

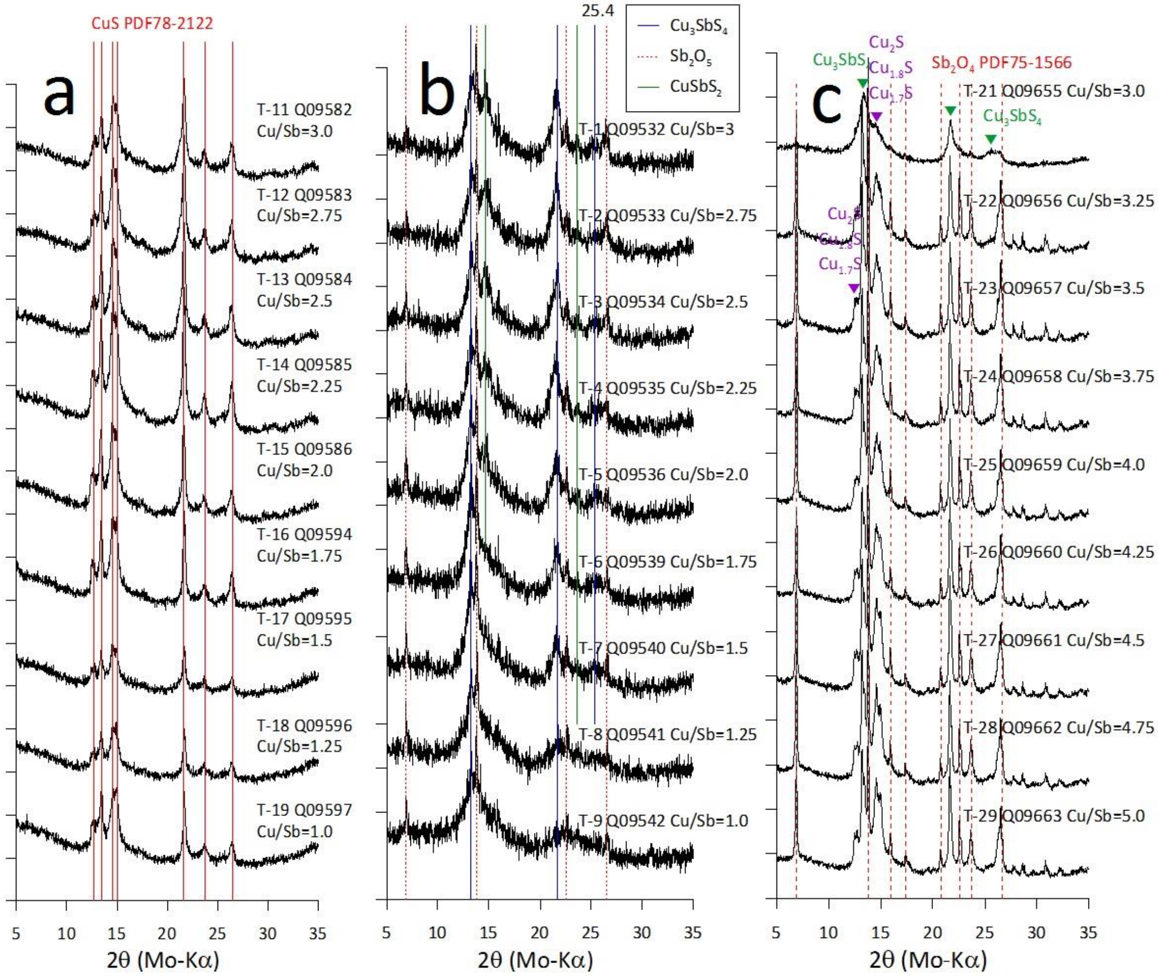

Figure 1-14. X-ray diffraction patterns of thermoelectric material precipitates. a) Cu/Sb=1.0–3.0 with $Sb^{3+}$, b) Cu/Sb=1.0–3.0 with $Sb^{5+}$, and c) Cu/Sb=3.0–5.0 with $Sb^{5+}$

### 2.1.6 Produce two new nanoparticle at bench scale of 5 g batches

We produced two new industrially-relevant nanoparticles in >5 g batches at bench scale including binary and tertiary components of kesterite (copper zinc tin sulfide, CZTS) such as CuS, ZnS, SnS, and $Cu_2SnS_3$ consisting of earth abundant elements. These binary samples were successfully produced by upscaling from 10 mL of growth medium through 1-L and 24-L reactors (Figure 1-15). Average crystallite sizes were less than ~10 nm based on XRD.

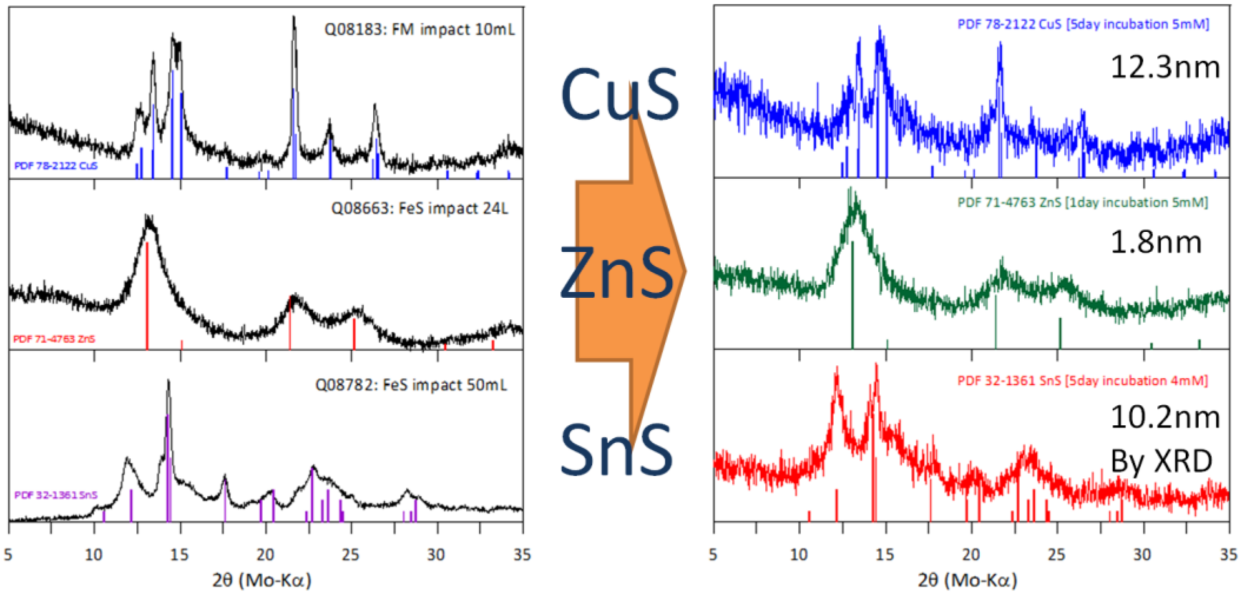

**Figure 1-15. Scale up of binary phase of CuS, ZnS, and SnS up to 24-L scale**

All three binary phases were produced in >5 g batches, with CuS yielding 13.1g, ZnS 11.8g, and SnS 17.1g (Figure 1-16). Samples of these CZTS binary components were shared with an industrial collaborator under a Materials Transfer Agreement for evaluation.

**Figure 1-16. Samples shared with DuPont**

We also continued work on efficient and stable dispersion of our representative target nanomaterial, ZnS. Several common aqueous phase surfactants and chelators were added during post-treatment. Samples treated by sonification were sedimented for 7 days, and only supernatant solutions were examined without further treatment. A small 3-mm diameter sonication tip and NTA were found to be the most effective combination from the previous results. Therefore we optimized properties of NTA-coated ZnS NPs holding constant the pH, surfactant concentration per mass of NPs, and total concentration during sedimentation.

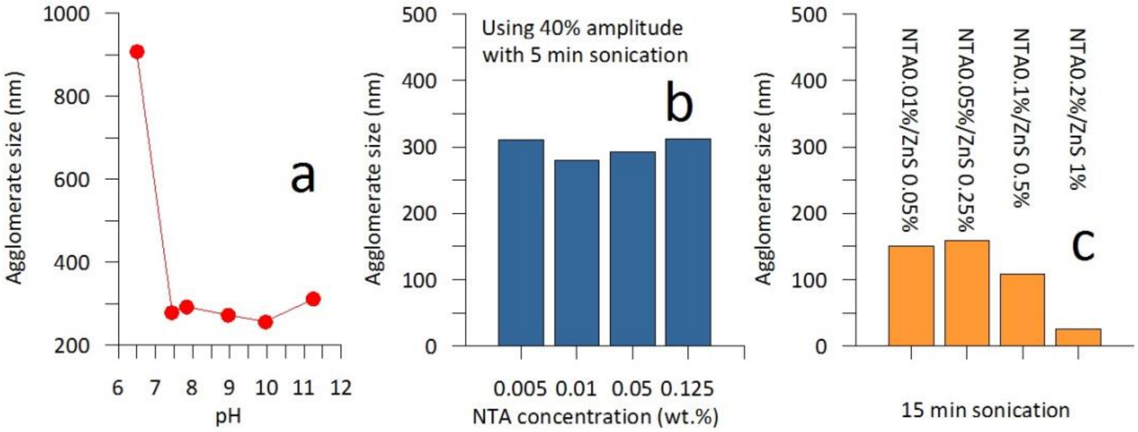

**Figure 1-17. Agglomerate size analysis of dispersed samples with NTA and sonication. Efficiently tuned NTA–treated ZnS samples exhibited an agglomerate size of 25.5 nm vs. a control sample at 1,041 nm**

pH values above neutral (~7) resulted in almost the same agglomerate size (pH 7.76, 9.05, 10.04, and 11.25 shown in Figure 1-17a). These experiments used ZnS solid particles at 0.05 wt.%. Variation of surfactant concentrations such as 0.005%, 0.01%, 0.05%, 0.125%, 0.25%, 0.5%, and 1% to 0.05 wt.% ZnS loadings revealed that surfactant:solid ratios of ~ 1:5 produced the smallest aggregate size (Figure 1-17b). With the last consideration as to the collision interference of overloaded NPs during the free-falling in the sedimentation, the total mass was changed while keeping the surfactant:solid ratio of 1:5 (Figure 1-17c). The smallest agglomerate size was identified at 0.2% NTA and 1% ZnS loading. This combined process of post-treatment with capping agents and sonication reduced the control sample (without any treatment) from 1,041 nm to 25.5 nm. The most efficiently suspended samples were prepared in multiple batches and shared with an industrial collaborator (Figure 1-18).

**Figure 1-18. Most efficiently supended ZnS with NTA (a) that was shared with an industrial collaborator (b)**

We extended our collaboration with the Additive Manufacturing Polymer Systems team (led by Lonnie Love and Orlando Rios). We delivered magnetite NPs substituted with 2% rare-earth gadolinium (Gd) and holmium (Ho), which will be applied to creating new materials requiring low Curie-temperature magnetites mixed with epoxy. With simple substitution of lanthanide into the magnetite crystal structure, the saturated magnetism at around room temperature dropped to half of that for non-substituted magnetite. Estimated Curie-temperatures declined 50–55%. The vials in Figure 1-19a have been provided to them for evaluation. Figure 1-19b & c show the supporting information from a small scale preparation described **previously (Moon et al., Extremophiles 11:859–67).**

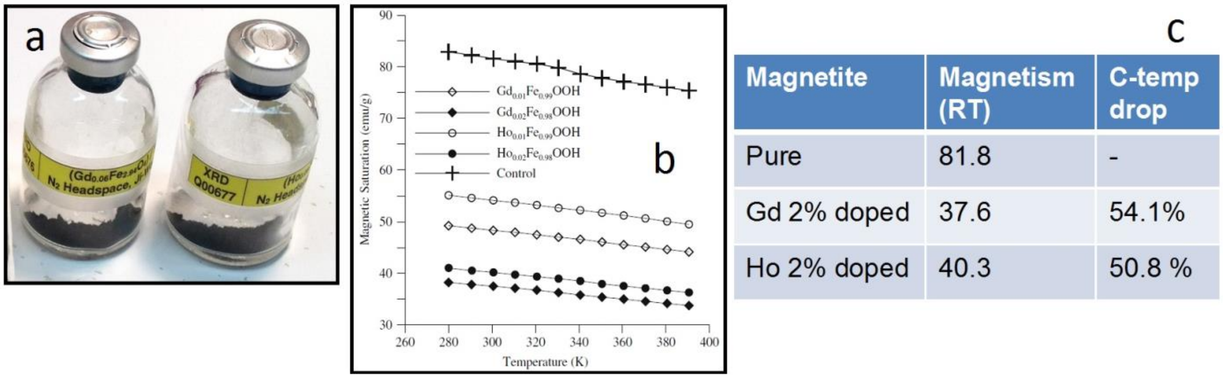

| Magnetite | Magnetism (RT) | C-temp drop |
|---|---|---|
| Pure | 81.8 | - |
| Gd 2% doped | 37.6 | 54.1% |
| Ho 2% doped | 40.3 | 50.8 % |

**Figure 1-19. Delivered samples of a) Gd and Ho 2% substituted magnetite and b) their saturated magnetism, c) Lanthanide-doped magnetite drops the Curie temperature approximately 50–55%**

### 2.1.7 Upscaling zinc gallate yield to > 50 g/month

Upscaling production of zinc gallate NPs to >50 g/month was accomplished using a 24-L reactor. Zinc-gallates are well-known phosphor materials, which can emit RGB colors depending on doping elements. These materials have a great potential for smart building programs. We successfully produced more than 50 g/month NPs with luminescence in each of the RGB colors (Table 1-1 and Figure 1-20).

**Figure 1-20. Scale up of zinc gallate phosphors up to 24-L scale**

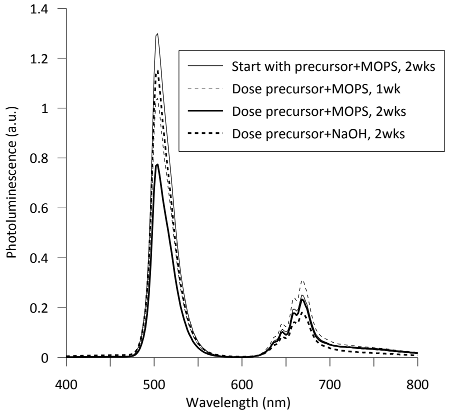

**Figure 1-21. Photoluminescence variation according to dosing methods, buffer types, and incubation time**

**Table 1-1. Produced RGB zinc gallates more than 50g/month**

| Zinc-gallate synthesis conditions | Yield (g/month) |
|---|---|
| Co 1% replacing Zn-1wk incubation for BLUE | 59.1 g/month |
| Mn 4% replacing Ga-1wk incubation for GREEN | 57.2 g/month |
| Cr 1% replacing Ga-1wk incubation for RED | 55.8 g/month |

We also compared photoluminescence depending on the dopant dosing methods, buffer types, and incubation period using a 325 nm laser (Figure 1-21). All samples using Mn (4%) replacing Ga exhibited strong photoluminescence peaks at ~505 nm. Quantum efficiency (QE) measurements on the third sample of the zinc gallate resulted in 1.02±0.01% QE, Average crystallite size fell into the range between 3.0-3.4 nm and photoluminescence was highest when all components were added to the medium at the initial time.

Work continued on efficient and stable dispersion of our representative target nanomaterial, ZnS, based on the finding that the NTA:ZnS at a 1:5 ratio produced the smallest agglomerate sizes at 0.2%/ZnS 1% loading. This combined process of post-treatment with capping agents and sonication reduced the control sample (without any treatment) from 1,041 nm to 25.5 nm (Figure 1-17c) using post recovery treatment. In situ treatment with NTA resulted in 147–183 nm aggregates (Figure 1-22a). Another set of candidate capping agents including thioglycerol, mercaptoethanol, and thioglycolic acid was tested for both post recovery and in situ treatments. Thioglycerol with in situ treatment produced smallest particle aggregates of 145 nm (Figure 1-22b). The most ZnS nanoparticle aggregates were around 150 nm using a size analyzer. In contrast, SEM observation that most aggregates were not found to be less than 300 nm likely due to the more aggregation while dried sample preparation (Figure 1-22c). This is supported by the fact that other investigators (Moreau et al., American Mineralogist, 2007, 89:950-960) reported that inorganic aggregation of ZnS initially occurred rapidly to form ~100 nm diameter aggregates but them slowed greatly or ceased after 1 week.

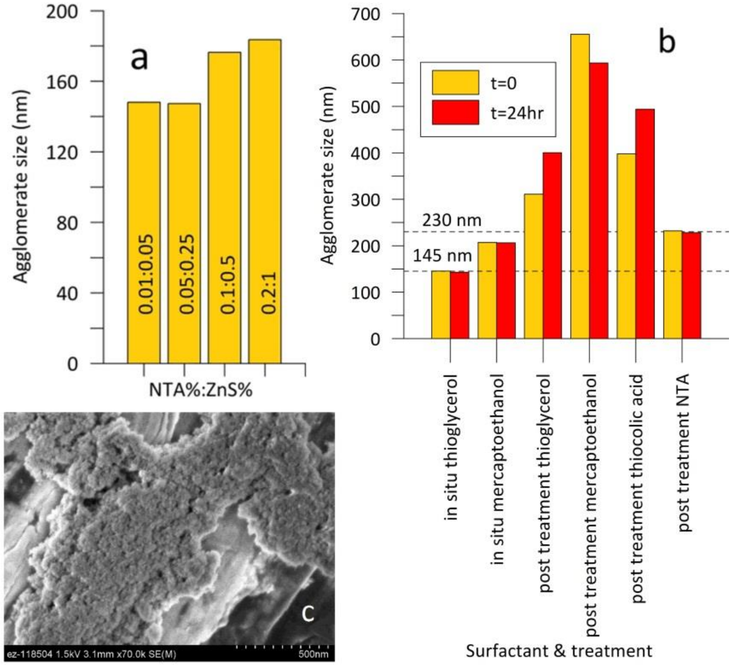

**Figure 1-22. Agglomerate size analysis of dispersed samples. a) in situ treatment with NTA, b) in situ and post treatment using thioglycerol, mercaptoethanol, and thiocolic acid, and c) Scanning electron micrographs of ZnS slurry/particles. The sample was prepared by putting a droplet onto the aluminum stub**

#### 2.1.7.1 Transition metal-doped magnetites

We began another collaboration producing transition metal-doped magnetites for an ARPA-E project led by U. Minnesota researchers and ORNL staff Edgar Lara-Curzio and Michael Brady. We shared manganese- and cobalt-doped magnetites, which were tested as precursors for iron nitrides that could replace rare earth magnets. Desired dopants of Mn, Co, C, Re, Ti, W, and Ta should exist in the water stability zone with fairly high concentration without forming oxides, but all except Mn and Co had low solubility in forms of ionic species, forming stable oxides around circumneutral pH in aqueous phase. The vials in Figure 1-23 have been provided to the team for evaluation. Figure 1-24 shows supporting information from a previous study (Moon *et al*., *J. Magn. Magn. Mater*. 313:283–92) about different coherency depending on doping elements.

**Figure 1-23. Co- and Mn-doped magnetite (nominal composition 10% and 20% substitution, respectively) in serum bottles. Mn-doped magnetites in microcentrifuge tubes with 5–30% substitution**

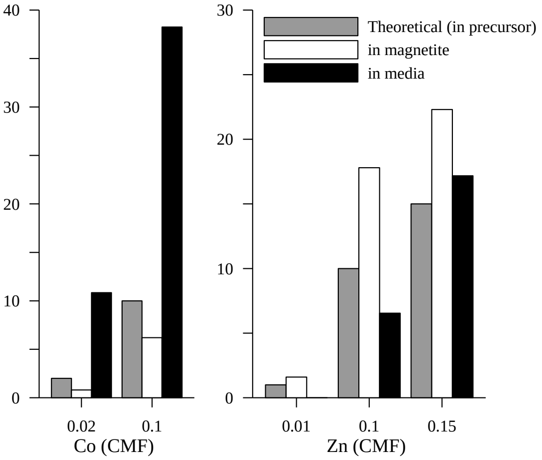

**Figure 1-24. Comparison of transition metal (TM) cation mole fraction in precursor theoretically, TM-substituted magnetite and final media where equal heights of bars indicate uniform incorporation**

### 2.1.8 Upscale low-carbon medium for ZnS >100 g/month

An abiotic process for producing ZnS with reduced organic contamination was developed for comparison with the NanoFermentation process. The upscaling of low-carbon medium for ZnS to >100 g/month was realized using a cysteine-sulfide (Cys-S) complex. We used 27 mM cysteine-sulfide as a sulfur source and chelator into anoxic deionized water, and then dosed 5 mM $Zn^{2+}$/day at a room temperature for 5 days (Figure 1-25). The initial pH of low-carbon medium with cysteine-sulfide was 9.40 and dropped to 2.39 after the first $Zn^{2+}$ dose. During incubation with discrete doses for 5 days the pH was adjusted with 10 N NaOH to maintain pH ~6. The final product weighted 31.75 g/12 L/5 days, so that we can produce 190 g/mo. This indicates that we successfully scaled up low-carbon medium for zinc sulfide with 200% productivity (Inset of Figure 1-25).

**Figure 1-25. Scale up of low-carbon medium to produce 100 g/month of zinc sulfide in 12 L**

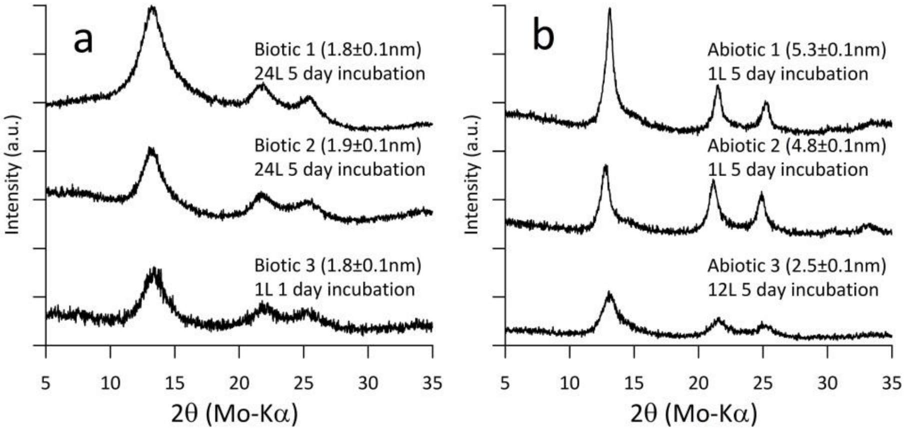

**Figure 1-26. Comparison of scale-up ZnS from a) NanoFermentation medium and b) low-carbon medium in 12 L**

**Table 1-2. Compared results from NanoFermented ZnS and low carbon medium ZnS**

| Group | Samples | ACS (nm) | Yield | Normalized Yield |
|---|---|---|---|---|
| NanoFermented ZnS | Biotic 1 | 1.8±0.1 | 12 g/24L/5days | 2.14 g/L/month |
| *(Green and economic)* | Biotic 2 | 1.9±0.1 | 10.97 g/24L/5days | 1.96 g/L/month |
| | Biotic 3 | 1.8±0.1 | Not measured | |
| Low-carbon medium ZnS | Abiotic 1 | 5.3±0.1 | 9.6 g/4L/5days | 14.4 g/L/month |
| *(expensive and more toxic)* | Abiotic 2 | 4.8±0.1 | 4.7 g/2L/5days | 14.1 g/L/month |
| | Abiotic 3 | 2.5±0.1 | 31.8 g/12L/5days | 15.9 g/L/month |

We then compared NanoFermented bio-ZnS with ZnS produced in low-carbon medium under various conditions including batch size, incubation time, and carbon content in the medium. As shown in Table 1-2, bio-ZnS had smaller ACS of ~2 nm rather than 2–5 nm ZnS in low-carbon medium (Figure 1-26). Bio-ZnS can also be produced at 3–5% of the raw material cost for abiotic synthesis (Moon *et al.*, J. Ind. Microbiol. Biot. 2013;40:1263–71). In contrast, low-carbon medium resulted in relatively higher normalized yields using more expensive and more hazardous chemicals.

The surfaces of freeze-dried bio-ZnS samples were examined using X-ray photoelectron spectroscopy (XPS). XPS spectra (Figure 1-27a) clearly exhibited the dominant carbonyl carbon (C=O, 288.1 eV) and hydroxyl carbon (C–O, 286.5 eV). Another spectrum (Figure 1-27b) exhibited a prominent main peak at 400.3 eV that likely corresponded to a primary amine (–$NH_2$) and a smaller peak at 401.8 eV, which could be a secondary amine (–NH). These results support our model that the final end products of bacterial fermentation including lactate and acetate, as well as microbially derived extracellular protein including amines and carboxylic acids, likely constrain the crystallite sizes of ZnS NPs, but also increase aggregation up to 100 nm particles.

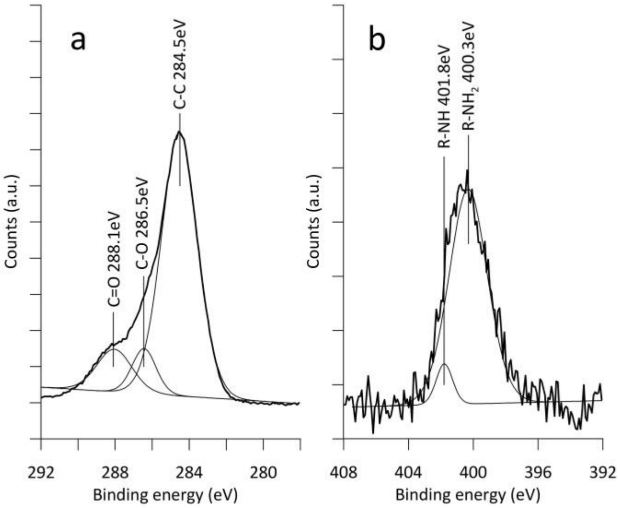

**Figure 1-27. XPS measurement of the surface of ZnS NP formed by *Thermoanaerobacter* X513 bacteria. a) XPS spectrum showing C=O and C–O bonds and b) XPS spectrum showing amines (–$NH_2$ and –NH)**

We also compared total nitrogen and total carbon contents depending on the media using a RICO C, N, S analyzer (Figure 1-28). Triplicates samples from Table 1-1 were analyzed using conventional soil analysis methods. NPs from low-carbon medium had lower nitrogen (22.3%) and carbon (13.2%) compositions compared to nitrogen and carbon from NanoFermented bio-ZnS. Using a low carbon medium we successfully reduced nitrogen and carbon contents in the final NPs.

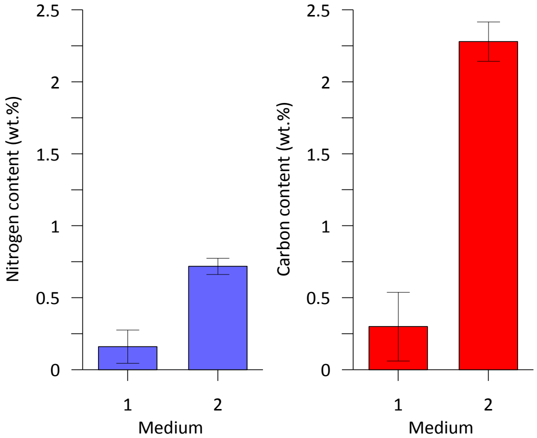

**Figure 1-28. C-N analysis of ZnS NP from different medium (1, abiotic, low-carbon medium; 2, biological NanoFermentation medium)**

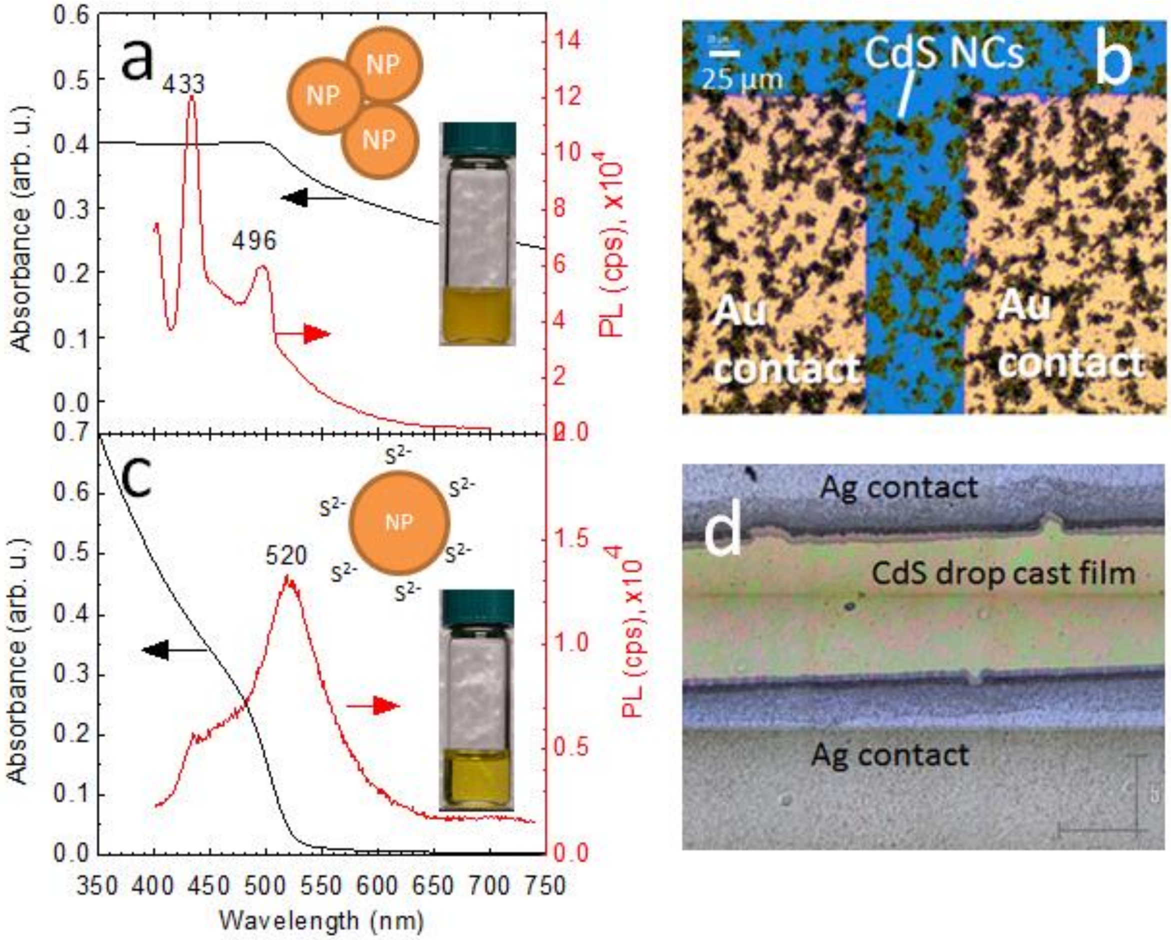

**Figure 1-29. Development of inorganic ligands for optoelectronic devices. Absorbance and photoluminescence of CdS a) before and c) after introduction of ligands, with insets of cartoon illustrations and photographs of NP samples. Optical microscope images of CdS thin-films fabricated from solution are shown b) before and d) after the introduction of ligands**

NanoFermented cadmium sulfide (CdS) nanoparticles were also examined for the fabrication of uniform thin films and optoelectronic devices requiring dispersible stable NP inks. A new method of functionalizing CdS NPs with inorganic ligands to produce stable colloidal "inks" was developed. Figure 1-29 shows a summary of the results. The functionalization was achieved through addition of ammonium sulfide ($(NH_4)_2S$) to a suspension of CdS NPs in a highly polar solvent (i.e. formamide). Upon addition of $(NH_4)_2S$, the solution changed from cloudy to an optically clear colloid (Figure 1-29). The absorption spectrum of a turbid, unfunctionalized CdS suspension (measured in a 1-cm quartz cell) was dominated by high absorbance due to light scattering (Figure 1-29a) below the band gap (~510 nm) (inset). For CdS surfaces-functionalized with $S^{2-}$ ligands the absorbance below the band gap reduces to zero (Figure 1-29c) and the yellow solution turned transparent (inset). Functionalized CdS particles exhibited photoluminescence (PL) with an emission maximum at 520 nm (Figure 1-29a and c) for excitation at 350 nm, which is characteristic for a band gap transition. The PL spectrum of turbid solutions of unmodified CdS NP shows 433 and 496-nm peaks attributed to the above-band gap transitions.

Thin films were fabricated using $S^{2-}$ modified CdS NP with controlled thickness of 10–100 nm, by changing the concentration of the NPs in the solvent. Figure 1-29b shows CdS NPs assembled in a film consisting of large (1–20 µm) agglomerate networks. Figure 1-29d shows an agglomerate-free, uniform

~200 nm thick film prepared from $S^{2-}$ modified CdS NP. Small inorganic ligands are assumed to improve NP-NP electronic coupling, thus improving overall charge mobility and increasing conductivity of NP networks. NP modification with inorganic ligands is highly adaptable and can be applied as an approach to create stable inks of other nanomaterials synthesized via NanoFermentation.

We extended our collaboration with ARPA-E team using microbially produced magnetites via NanoFermentation. Our collaboration was extended to share more magnetites with wide composition and a larger quantity (>10 g) of cobalt-doped magnetites for initial trial. The vials in Figure 1-30 have been provided for various experiments with wider composition of magnetite precursors. We continuously strengthened collaborations determining appropriate dopants and then upscaling to provide sufficient materials for their product development, testing and optimization.

**Figure 1-30. Freeze dried and NanoFermented cobalt 10 %-doped magnetites attached to handheld magnet**

### 2.1.9 Identify 2+ candidates for FY2014 – selenides, optics, thermal, electrical

To identify 2+ candidate NPs for bench scale-up based on industry and EERE-relevance such as metal selenide, optics, thermal, or electrical properties, we completed this series of metal chalcogenide nanoparticles, characterizing them, and thermally transforming them into metal oxides using controlled oxidation. We focused on SnS and CuS as precursors for $SnO_2$ and CuO as final products.

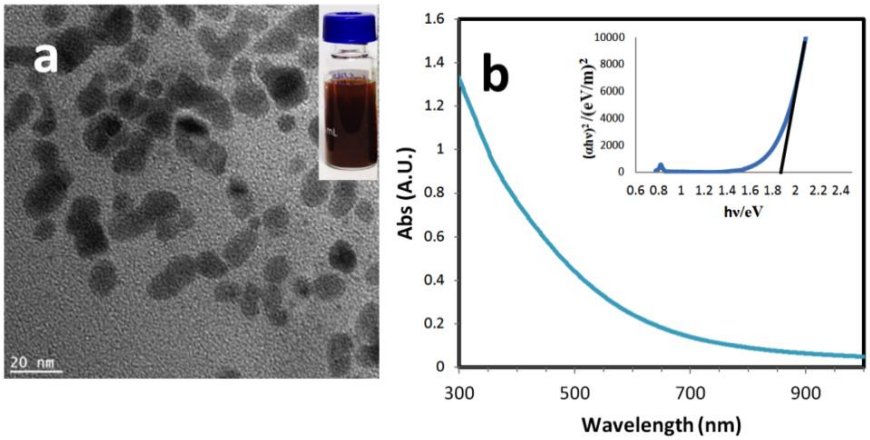

**Figure 1-31. a) TEM image of SnS NPs (Inset is SnS NPs dispersed in formamide solution), b) Optical absorption spectrum of SnS NPs (Inset is a plot of $(\alpha h\nu)^2$ versus hν for direct band gap estimation)**

The first candidate nanoparticle was tin oxide ($SnO_2$) that could be produced from tin sulfide (SnS) nanoparticles that were synthesized by a biological process during 5 days incubation. The harvested NPs exhibited SnS nanocrystals with ~15 nm diameter (XRD ACS = 4.3 nm) (Figure 1-31a). Figure 1-31b shows the UV-vis-NIR absorption spectrum of as-synthesized SnS NP: the inset plot shows a direct estimation of the SnS NPs band gap at 1.85 eV. For bulk SnS the direct band gap transition is at 1.3 eV. The observed blue shift of 0.55 eV was attributed to the quantum size confinement effect.

The SnS NPs were thermally annealed at 400 ºC, 600 ºC, and 800 ºC in air for 1 hr (Figure 1-32). At 400 ºC, SnS was thermally transformed to $SnO_2$ with 4.5 nm ACS, while the crystal size did not increase relative to SnS NP. The corresponding TEM image shows $SnO_2$ formed irregular rods and non-spherical shapes. At increasing annealing temperatures, the ACS of $SnO_2$ increased to 13.0 nm at 600 ºC and 19.3 nm at 800 ºC). TEM images confirmed that higher temperature annealing formed more spherical shapes with increased crystal sizes at 600 ºC and 800 ºC.

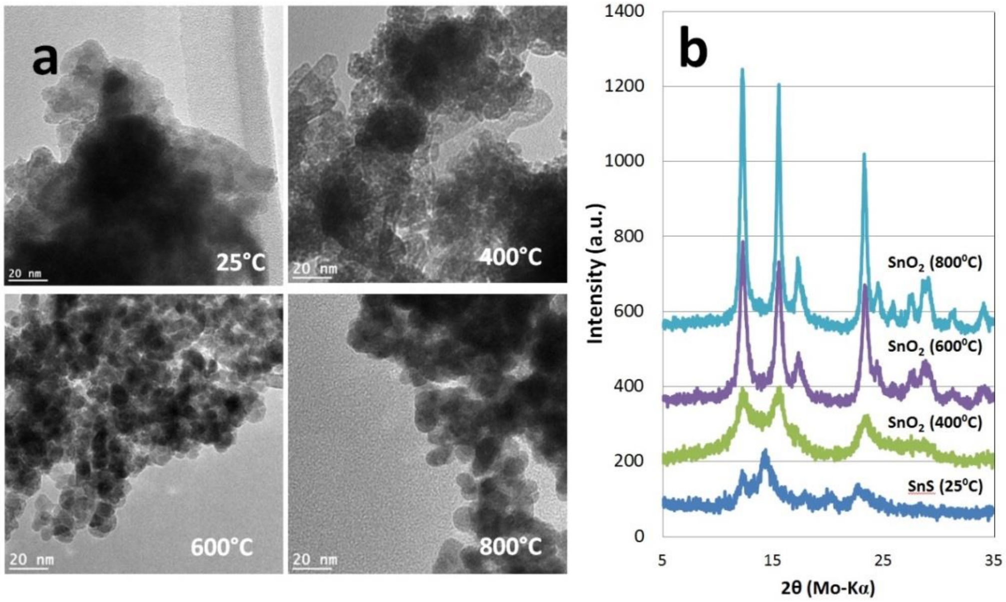

**Figure 1-32. Controlled annealing of SnS in the air. a) TEM pictures and b) corresponding XRD patterns of as-synthesized and thermal annealed nanoparticles at 400 ºC, 600 ºC, and 800 ºC**

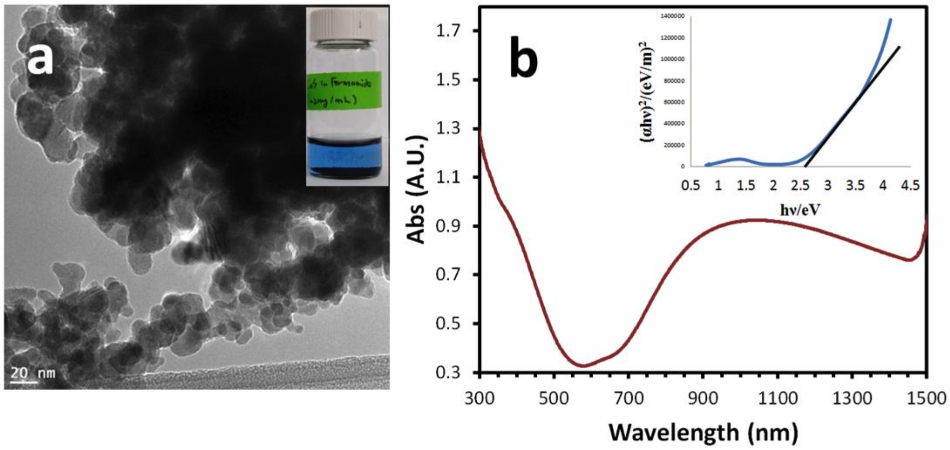

**Figure 1-33. a) TEM image of CuS NPs (Inset is CuS NPs dispersed in formamide solution), b) Optical absorption spectrum of CuS NPs in (Inset is a plot of $(\alpha h\nu)^2$ versus hν for direct band gap estimation)**

The second candidate NP was copper oxide (CuO) that could be produced from copper sulfide (CuS) NPs that were synthesized by biological process during 5 days incubation. The harvested NPs exhibited CuS nanocrystals with ~15 nm of diameter (ACS = 7.9 nm) (Figure 1-33a). Figure 1-33b shows the UV-vis-NIR absorption spectrum of CuS NP. Interestingly, it showed a strong and broad absorption peak at 1000 nm, which is an intense localized surface plamson (LSP) band in the NIR. (It was reported that the LSP tuning via surface sulfide amount controlled photoluminescence intensity.) The inset plot shows a direct band gap estimation of 2.52 eV for the as-synthesized CuS NPs. For bulk CuS the direct band gap transition is at 2.36 eV. The observed blue shift of 0.16 eV was attributed to a quantum size confinement effect.

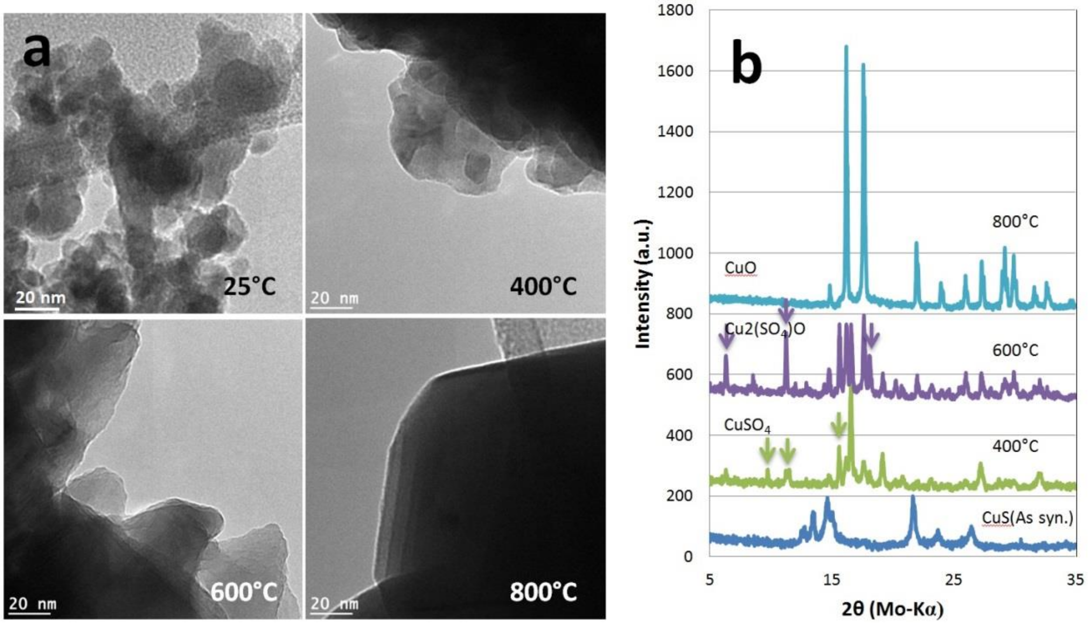

**Figure 1-34. Controlled annealing of CuS in the air. a) TEM pictures and b) corresponding XRD patterns of as-synthesized and thermal annealed nanocrystals at 400 ºC, 600 ºC, and 800 ºC.**

The CuS NPs were thermally annealed at 400 ºC, 600 ºC, and 800 ºC in air for 1 hr. At 400 ºC and 600 ºC, CuS NPs were thermally transformed to mixture of CuO, $CuSO_4$, and $Cu_2(SO_4)O$. The highest annealing temperature at 800 ºC fully transformed the precursor to CuO with a 69.1 nm ACS. TEM images also confirmed the CuO consisted of well crystallized particles (Figure 1-34).

A Raman spectrum confirmed the crystal structure of thermally transformed CuO (Fig. 1-35). Three Raman bands at 289 ($A_g$), 341($B_g$) and 626 $cm^{-1}$($B_g$) were detected. The CuO belong to the C62h space group with two molecules per primitive cell. There are nine zone-center optical phonon modes with symmetries $4A_u+5B_u+A_g+2B_g$; three Ag+2Bg modes were Raman active in our sample. These wavenumbers are close to Raman spectra of CuO nanocrystals reported in the literature (288, 330 and 621 $cm^{-1}$)

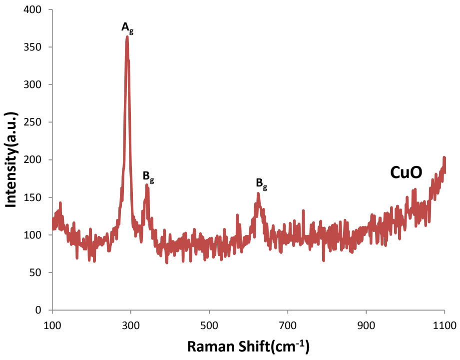

**Figure 1-35. Raman spectrum of CuO.**

### 2.1.10 Two new nanoparticle products > 10g

For the gas diffusion process developed to convert magnetite NPs to iron nitride, small crystallite sizes are advantageous. Therefore we produced Zn-doped magnetite NP samples that formed smaller crystals compared to pure magnetite (Figure 1-36). This task also upscaled production quantum-dot sized ZnS NPs to produce quantum dot-sized NPs using organic capping agents resulting in ~26-fold higher luminescence.

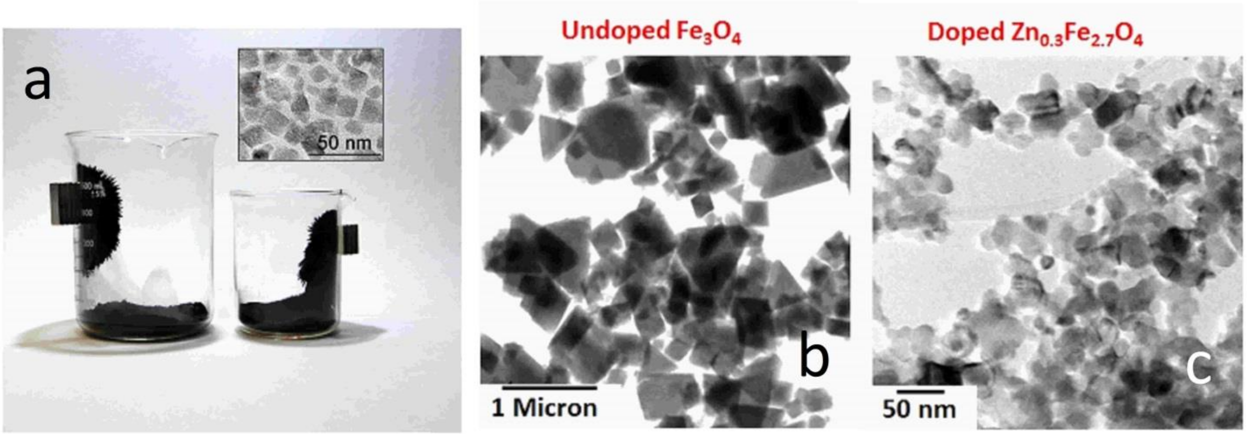

**Figure 1-36. Pure and Zn-doped magnetites. a) Fine magnetic particles from a 30 L reactor demonstrate paramagnetic activity in the presence of permanent magnets, Moon et al., 2010, b) straight magnetite and c) Zn-doped magnetite evaluated for current collaboration**

**Table 1-3. Produced Zn-doped magnetites**

| Doping | Input concentration (mM) | Average crystallite size (nm) | Reactor volume | Reference |
|---|---|---|---|---|
| Zn 1% | 60 | 15.3±0.8 | 250 mL | This study, MDF |
| Zn 5% | 60 | 12.3±0.6 | 250 mL | This study, MDF |
| Zn 10% | 60 | **12.6±0.5** | 250 mL | This study, MDF |
| Zn 1% | 30 | 30.7±2.1 | 1 L | This study, MDF |
| Zn 5% | 30 | 25.0±1.6 | 1 L | This study, MDF |
| Zn 10% | 30 | **17.7±1.0** | 1 L | This study, MDF |
| Zn 10% | 107 | **28.4±0.1** | 30 L | Moon et al., 2010 |
| Zn 20% | 80-120 | 13.0±0.8 | 30 L | Moon et al., 2010 |

Iron nitride formation from Zn 10%-doped magnetite demonstrated the Zn was not extensively incorporated into the target structure. Therefore the precursor NPs should have a lower Zn-doping concentration, while maintaining the small crystallite and particle size. Therefore we investigated a new synthetic route for both lower Zn-doped and smaller magnetite NPs. This new method combined previously published, patented, and patent-pending techniques to reduce crystallite size by 30–50%, even at low input concentration (Table 1-3). As a another advantage, this new process did not require precursor aging or long waiting periods that were required in our previous processes (described in patents US6,444,453 and US7,060,473). Samples of the new Zn-doped magnetites have been shared with ORNL collaborators for testing in the iron nitride production process (Figure 1-37). This innovation further distinguishes magnetite nanoparticle synthesis by NanoFermentation from alternative methods, by creating smaller, high-value nanoparticles.

**Figure 1-37. Zn-doped (1, 5, and 10%) magnetites from 1 L of media using a new method that produced 3.63g, 6.55g, and 3.40g, respectively**

### 2.1.10.1 Elemental copper

Task 1 also focused on completing the upscaling elemental copper nanoparticle production and characterization of electrical properties from annealed films. The scalability of bacterial elemental Cu NP production was tested by increasing the medium volume 100-fold using a 1000-mL reactor with the same dosing ratio of glucose, Cu salt and capping molecules. Yields of four capped Cu NPs such as CuNO, CuNA, CuNM and CuNC NPs were 0.176 g/L, 0.154 g/L, 0.198 g/L and 0.088 g/L, respectively. For comparison, the yield of Cu NPs from a 10-mL reactor was less than 0.001 g. Scaling showed no significant influence on the morphological (SEM), crystalline structural (XRD), or chemical structural (XPS, FTIR) properties of colloidal Cu NPs.

The electrical properties of Cu NPs were further studied using CuNC and CuNO NP pastes which were re-dispersed in toluene with a particle content of 30 wt. %. The prepared Cu pastes were deposited on platinum electrodes on plastic substrates, and annealed at 150, 200, 250, 300, and 350 ºC for CuNC NP film and 300 ºC for CuNO under an Ar atmosphere. Figure 1-38 shows the Current (I)-Voltage (V) curves exhibiting the increased current response to increased temperature. The calculated resistivity values were $5.1\times10^4$, $1.8\times10^4$, $4.4\times10^3$, $1.0\times10^2$, and 16.0 Ω·cm, respectively. Also, the resistance (Rs) of the annealed CuNC films at low frequency impedance was measured to be 3.4, 3.4, and 0.14 MΩ at 250, 300, and 350 ºC, respectively. The preliminary resistivity of CuNO was $1.84\times10^3$ Ω·cm, which was higher than CuNC at 300 ºC.

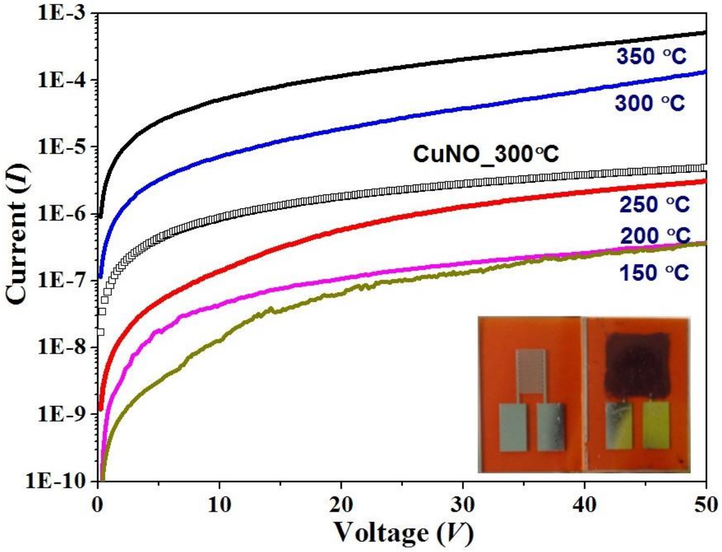

**Figure 1-38. Current(I)-Voltage(V) curves of annealed CuNC and CuNO NP films. Inset are photographs of a**

**bare platinum finger electrode on plastic substrate (left) and Cu NP deposition on electrode (right)**

Figure 1-39 shows the corresponding SEM images with annealing temperatures. The thermal decomposition of capping molecules and biomaterials started above 150 ºC and densification of neighbors with removal of capping molecules was observed at 350 ºC (Figure 1-39a, b, and c). The CuNO sample exhibited a different morphology due to small size and residual carbon molecules. (Figure 1-39d) The high resistance suggests that annealing at 300–350 ºC may partially remove capping molecules and fermentative organics and form surface oxidation through exposed surfaces. XPS analysis demonstrated that further oxidation occurred after annealing.

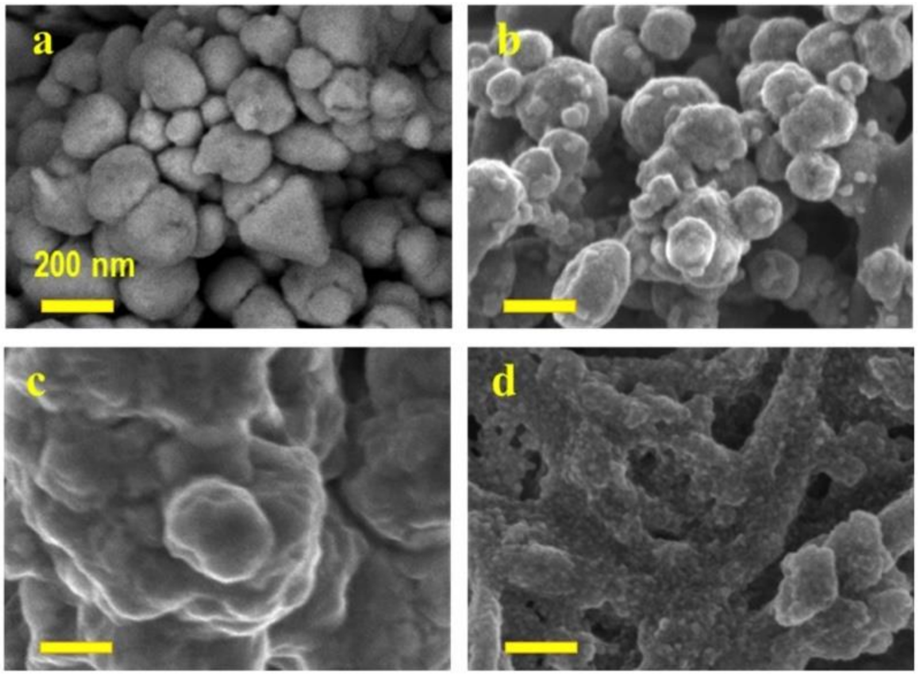

**Figure 1-39. SEM images of corresponding Cu NP films with increasing annealing temperature. a) CuNC at 150 ºC, b) CuNC at 250 ºC, c) CuNC at 350 ºC, and d) CuNO at 300 ºC**

**Table 1-4. Electrical properties of annealed drop-casted Cu NP thin films**

| Sample | Temp. (ºC) | Thickness | Measured raw resistivity | Corrected resistivity **(×0.1)** | Referential Cu NPs |
|---|---|---|---|---|---|
| CuNO | 200 | 25μm | Not measured | Not measured | 1.Glycolic acid capped Abiotic Cu:25.5±8.0 μΩ·cm<br>2. Abiotic Cu:17.0 μΩ·cm |
| | 300 | - | $6.7\times10^4$ Ω·cm | $6.7\times10^3$ Ω·cm | |
| | 400 | - | $7.5\times10^3$ Ω·cm | $7.5\times10^2$ Ω·cm | |
| | **500** | (4~5 μm) | **456.8±63.9μΩ·cm** | **45.68±6.39μΩ·cm** | |
| CuNC | **350** | (30 μm) | **551.4±70.8μΩ·cm** | **55.14±7.08μΩ·cm** | |
| Ref. Cu foil | 25 | 30 μm | **34.1 μΩ·cm**<br>**(1.7 μΩ·cm**<br>: literature value) | **3.41 μΩ·cm** | |

High temperature annealing up to 500 °C was performed to remove adsorbed extra capping molecules and organics residues. Table 1-3 shows that at 500 °C of annealing, the measured raw resistivity values were 456.8±63.9μΩ·cm or 45.68±6.39μΩ·cm or less, which may be comparable to abiotic Cu NPs. Bacterial organics and excess capping molecules on the surface of NPs resulted in strong binding for high resistivity. Thus, harvesting and following post-treatment such as washing with organic solvents and other chemical additives were planned in follow-on work.

### 2.1.10.2 ZnS

The in-situ addition of an organic surfactant (oleic acid) during NanoFermentation was demonstrated to control the size and optical properties of ZnS nanoparticles. As a result, highly luminescent oleate-bio ZnS quantum dots were synthesized by adding oleic acid during the NanoFermentation process, which we have demonstrated at reactor volumes from 10 to 24,000 mL. Optical, crystalline and chemical structural characterizations using spectrofluorometry, TEM, XRD, XPS, FTIR and UV-vis absorption methods indicated that oleic acid capping exhibited significant size-confinement effects to produce zero-dimensional QDs with 2.5 nm of particle size. This enhancement in oleate-bio ZnS resulted in ~26-fold higher luminescence than a control suspension of untreated bio ZnS nanoparticles. The bio ZnS NPs in turn exhibited higher emission than L-cysteine capped abiotic ZnS (Figure 1-40a). The upscaling conditions for the process were evaluated in a 24,000-mL reactor for the mass production of 33 grams of NPs (Figure 1-40b).

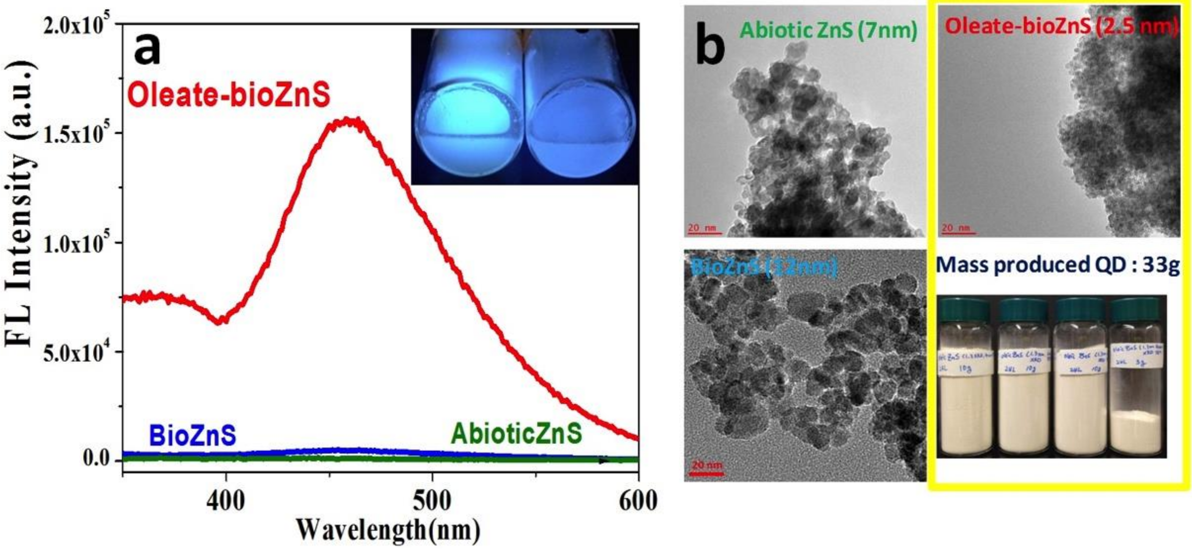

**Figure 1-40. a) Sensitive FL measurement of oleate-bio ZnS colloidal particles in formamide (inset left) compared with bio ZnS (inset right) and abiotic NP (L-cysteine capped) and b) Using the optimized synthesis condition, the 24-L scale-up experiment produced 33 g of oleate-bio ZnS QD**

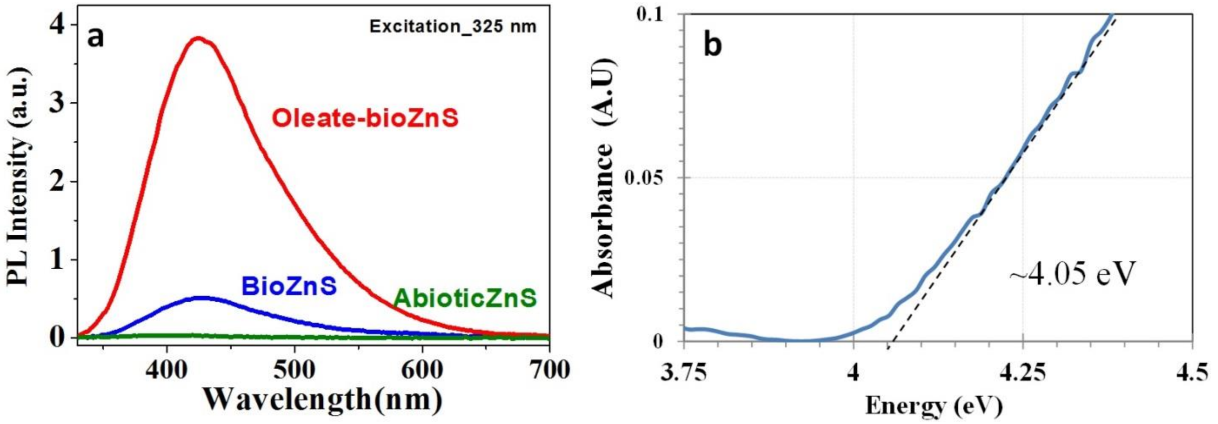

**Figure 1-41. a) PL measurement of oleate-bio ZnS dry powders compared with bio ZnS and abiotic NP (L-cysteine capped) and b) Band gap calculation of oleate bio ZnS using a Tauc plot**

The photoluminescence (PL) and UV-vis reflectance of oleate-bio ZnS QD dry powders were investigated (Figure 1-41a) and it was ~8 time higher than bio ZnS exhibiting higher PL than L-cysteine capped abiotic ZnS powders. The band gap of oleate-bio ZnS QD was determined to 4.05 eV (ex. bulk ZnS : 3.6 eV), shown in Figure 1-41b.

We also evaluated the emission enhancement factor (e.g. dispersion effect for QD ink formula) in different solvent matrixes. The dry ZnS QD powders were re-dispersed in several polar and non-polar solvents such as hexane (dielectric constant (Ɛ)=1.89), toluene (2.38), ethanol (24.6), water (80) and formamide (106). We found water is the most appropriate solvent to disperse ZnS QD, resulting in the highest FL intensity and suspending it for the longest time (Figure 1-42). In toluene, a non-polar solvent, the oleate-bio ZnS QD aggregated in the matrix. The toluene-washed ZnS QD mixture was re-dispersed in formamide (FA), but its FL intensity was not recovered.

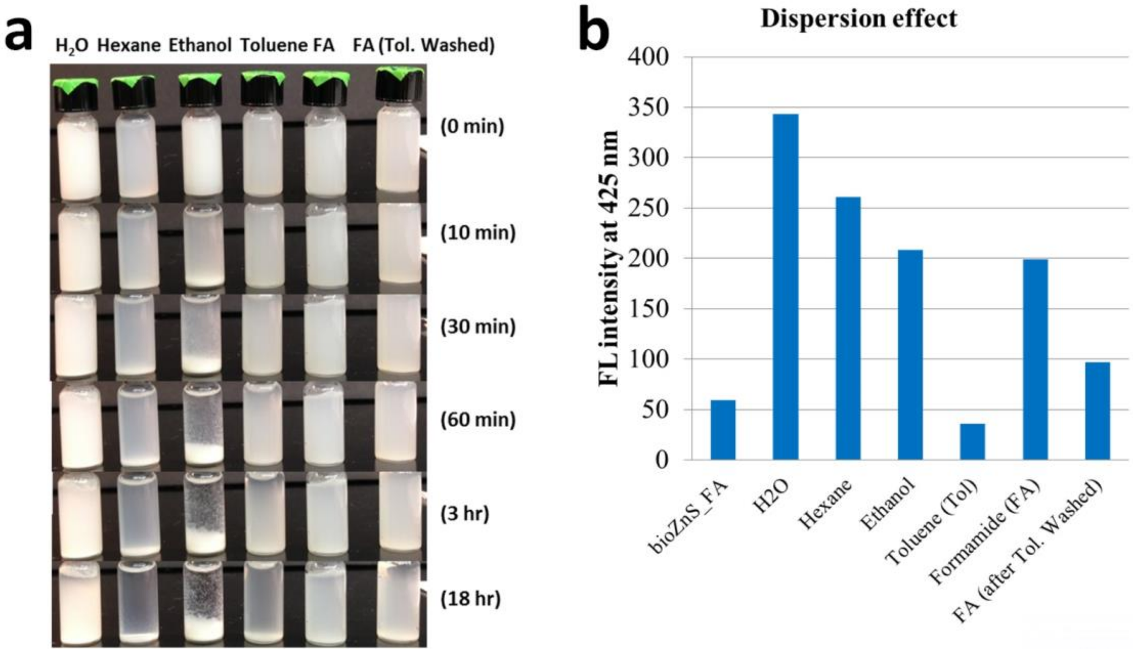

**Figure 1-42. a) Time-course photographs illustrate the precipitation behaviour of colloidal oleate-bio ZnS QD via aggregation. b) Corresponding FL measurement at 0 min**

### 2.1.11 Two new materials at 1 g batches appropriate for characterization

More than 1 g of homogeneous final product of new materials is requirement for the characterization. We controlled the crystallite size of NPs using organic capping agents and measured enhanced optical properties of several quantum-dot NPs including CdS and SnS. The crystallite sizes of zinc-doped magnetite as an iron nitride precursor for higher nitridation were also controlled.

For magnetic NP precursors for iron nitride production, collaborators tested a stock sample (US-7) in the first attempt to form iron nitride. This powder was partially nitrided at around 40% with secondary phases of 44% Zn-Fe oxide, and 16% elemental iron. For the suggested gas diffusion process, small crystallite sizes are advantageous. Therefore we continuously provided ORNL collaborators with test samples of Zn-doped magnetite nanoparticles that formed smaller crystals compared to straight magnetite (Table 1-5).

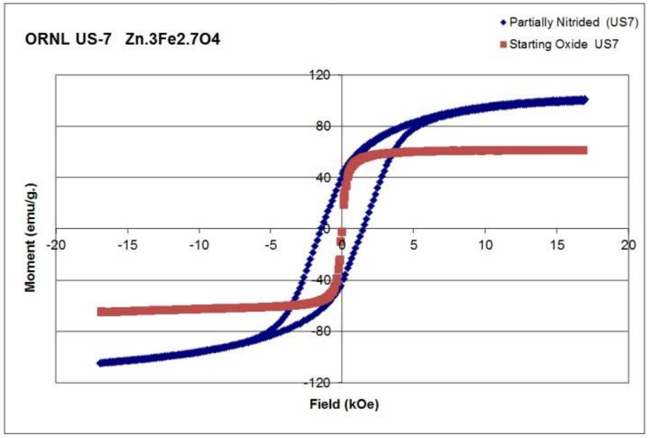

**Figure 1-43. 1st attempt at nitriding ORNL 10% Zn-doped magnetite powder yields ~1500 Oe coercivity**

Fresh Zn-doped (1, 5, and 10%) magnetites biosynthesized in 500 mL of media using a new method for lowering the Zn level and controlling smaller crystallite sizes produced 2.94 g and 3.00 g for Zn 1% and 5% doping, respectively (Figure 1-44a and b). 10% Zn in amorphous phase might have produced toxic conditions for the *Thermoanaerobacter* cells.

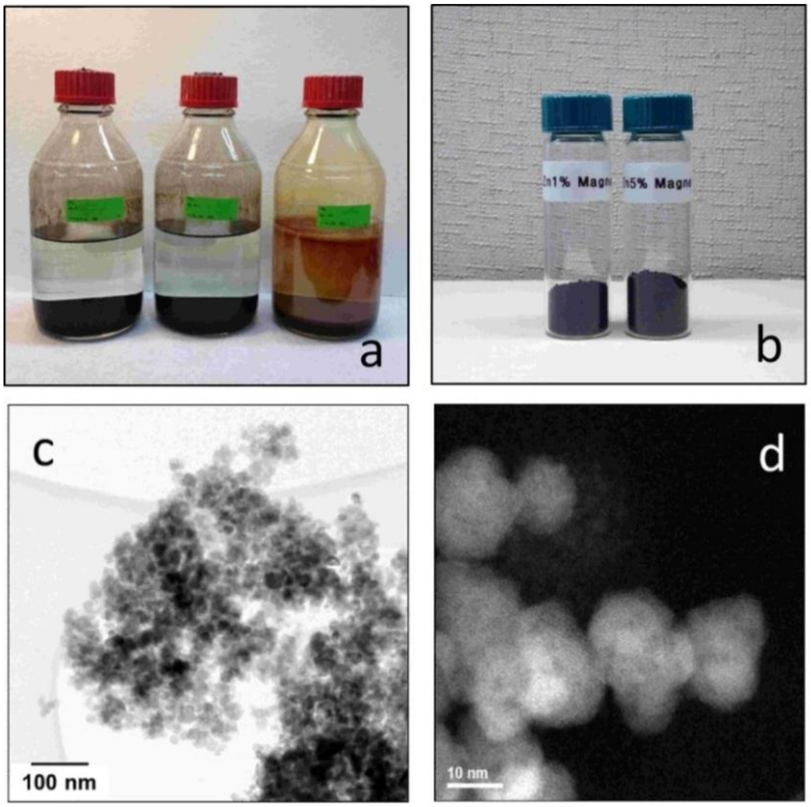

**Figure 1-44. Samples for collaboration to synthesize iron nitride. a) the latest batch for Zn 1, 5, and 10% doped magnetite using the new protocol, b) final product after freeze drying. c) & d) TEM images showing fine uniform Zn-doped magnetite NPs with less than 20-nm size**

### 2.1.11.1 Zn-doped magnetite

Produced samples were also delivered to an industrial partner in the ARPA-E REACT project, for testing. The particles were confirmed to be very fine, uniform Zn-doped magnetite particles (Figure 1-44c and d), and EDS showed a lower Zn concentration than the initial 10% Zn batch. The REACT team studied the nitridation of magnetite batches with different proportions of Zn-doping to optimize iron nitride yield and measure saturated magnetization (Ms) and coercivity (Hc).

**Table 1-5. Produced Zn-doped magnetites**

| Doping | Input concentration (mM) | Average crystallite size (nm) | Reactor volume | Reference |
|---|---|---|---|---|
| Zn 1% | 60 | 15.3±0.8 | 250 mL | Q3Report, MDF |
| Zn 5% | 60 | 12.3±0.6 | 250 mL | Q3Report, MDF |
| Zn 10% | 60 | 12.6±0.5 | 250 mL | Q3Report, MDF |
| Zn 1% | 30 | 30.7±2.1 | 1 L | Q3Report, MDF |
| Zn 5% | 30 | 25.0±1.6 | 1 L | Q3Report, MDF |
| Zn 10% | 30 | 17.7±1.0 | 1 L | Q3Report, MDF |
| Zn 1% | 60 | **18.5±1.0** | 500 mL | *Q4 study, MDF* |
| Zn 5% | 60 | **17.2±0.2** | 500 mL | *Q4 study, MDF* |
| Zn 10% | 60 | Not responded | 500 mL | *Q4 study, MDF* |

### 2.1.11.2 CdS

Another new nanoparticle is highly luminescent cadmium sulfide (CdS) nanocrystals (NCs) produced by the in-situ addition of oleylamine before adding the cadmium salt precursor during NanoFermentation that controls the size and optical properties of CdS NCs with quantum dot (QD) dimensions (< 5 nm). The harvested oleylamine-capped CdS NCs material had approximately 10-times enhanced fluorescent (FL) intensity at 550 nm, compared to previous biologically produced CdS (Figure 1-45a) and had a very broad and strong FL peak intensity attributing to quantum size confinement and surface defects. However, the harvested NC products showed mixtures of cadmium carbonate (otavite: $CdCO_3$), organic byproducts and CdS NCs after an ordinary washing procedure (i.e. $H_2O$ and ethanol) (Figure 1-45b).

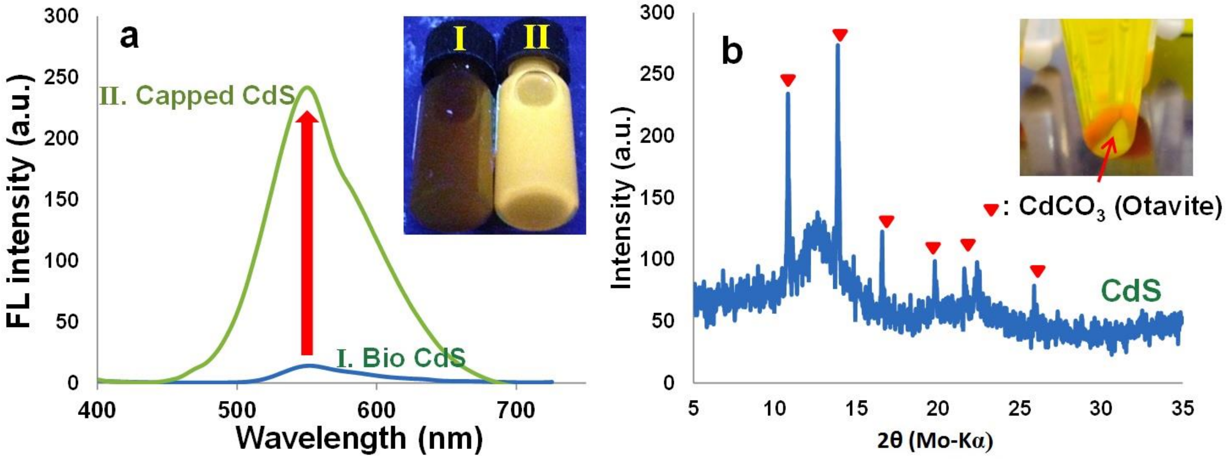

**Figure 1-45. a) Fluorescence spectra comparison between bio CdS NCs(I) and as-synthesized oleylamine capped CdS NCs(II). Inset is a comparison of two samples illuminated with a UV lamp b) XRD pattern of as-**

**synthesized oleylamine capped CdS NPs exhibiting a mixture of $CdCO_3$ byproducts**

Therefore, CdS QDs was separated from the as-synthesized mixture of oleylamine-capped CdS NCs and otavite by organic solvent extraction with toluene. The harvested sample was redispersed in toluene, and it was centrifuged at 8000 rpm for 3 min. The white otavite powders and large size or aggregated oleylamine-capped CdS NCs precipitated on the bottom (Inset of Figure 1-45b). The toluene extracted QD material forms a clear yellow solution that does not form precipitates (Figure 1-46a), while bio CdS in toluene showed precipitation after 1 day. It appears very small and high quality capped CdS QD materials were extracted by toluene. The toluene extracted CdS QDs exhibit two additional strong absorption peaks at 320 nm and 395 nm, compared to the suspended bio CdS NCs in toluene (Figure 1-46b). The absorption peak at 395 nm is a characteristic CdS QD peak that was reported from several abiotic CdS QDs. Interestingly, the fluorescence spectrum of CdS QD (red dot in Figure 1-46b) shows approximately 16-times higher intensity at 550 nm than bio CdS NCs. The FL intensity was 60% higher than as-synthesized CdS QD mixture materials. X-ray photoelectron spectroscopy (XPS) confirmed the existence of Cd2p and S2p peaks from the extracted QD material (Figure 1-46c). FTIR spectra showed the strong transmission depth at 2950 $cm^{-1}$ and below 1500 $cm^{-1}$ representing carbon complex binding of oleylamine on CdS QD surface (Figure 1-46d). The resulting QD have a band gap of 3.1 eV, similar to the band gap of 3–4 nm CdS QDs (versus bulk CdS: 2.44 eV).

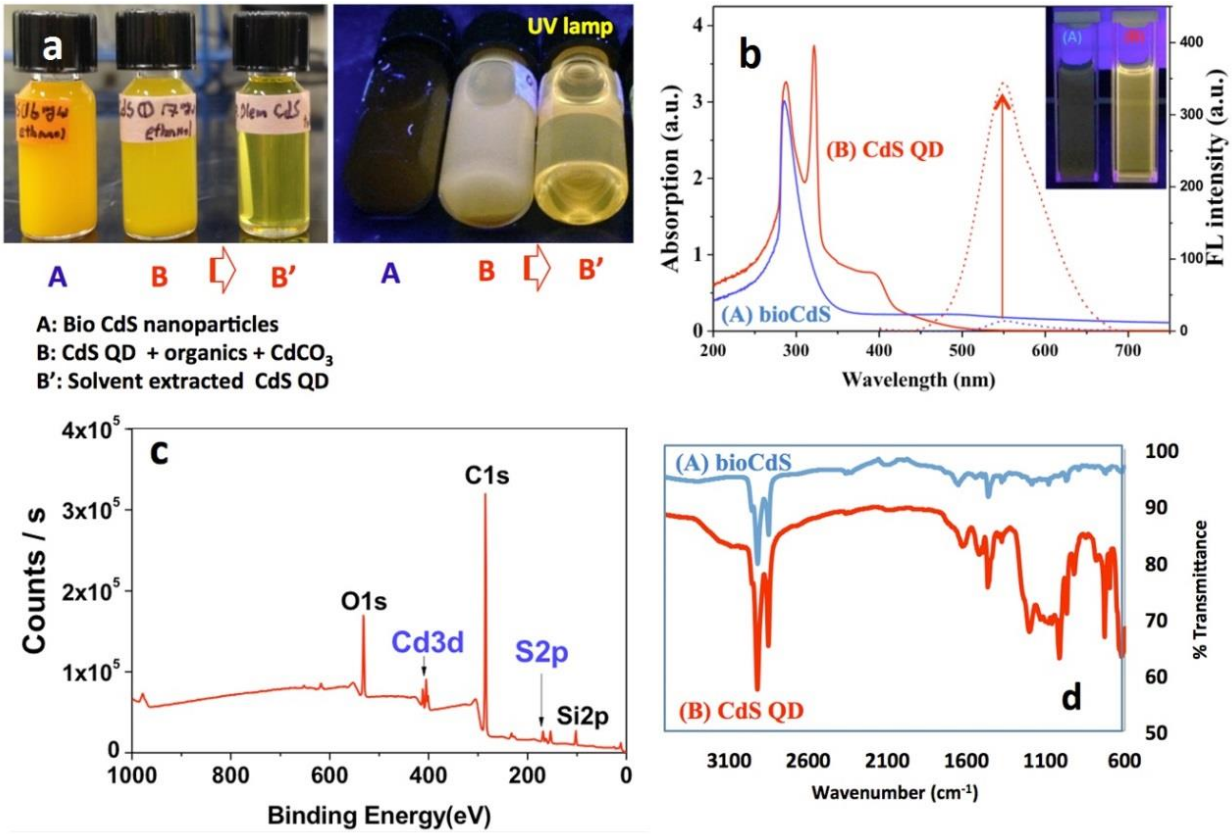

**Figure 1-46. a) Solvent extraction of high quality CdS QDs from the harvested CdS and $CdCO_3$ mixture. b) Optical features (UV-vis absorption (solid line) and fluorescence (dot line)) of bio CdS NCs (A) and the extracted CdS QDs (B). Inset is a comparison of two colloidal samples under UV lamp c) Survey scanning of XPS pattern of the extracted CdS QDs d) FTIR spectra of bio CdS NCs and the extracted CdS QD**

The electrical properties of the extracted CdS QDs were investigated using the deposition of a drop casted film on a finger-type platinum electrode (Inset Fig. 1-47a). The CdS QD film showed high luminescence under a UV-lamp. Figure1-47a shows the Current(I)-Voltage (V) curves exhibiting 6 order of magnitude increased current response for the CdS QD films, compared to a bio CdS NC reference film.

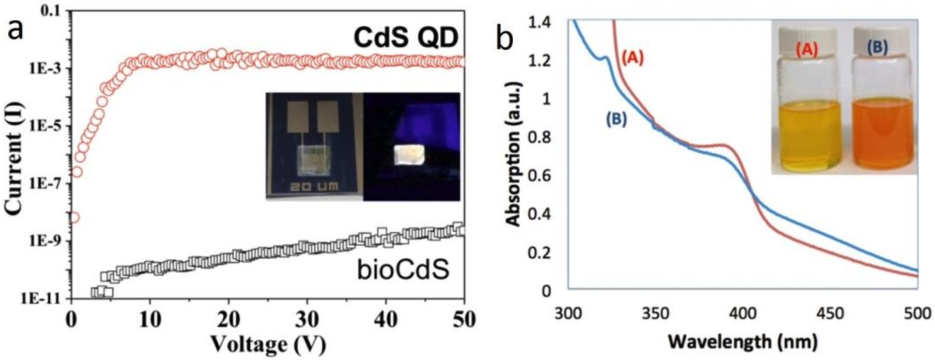

**Figure 1-47. a) I-V curves of dropcasted CdS QD and bio CdS NC films. Inset is a deposited CdS QD film on the electrode (left) and its emission feature under UV-lamp (right). b) Absorption spectra of toluene extracted CdS QD materials from a mixture of CdS and $CdCO_3$ (A) and otavite free CdS (B)**

Otavite-free oleylamine-capped CdS NCs were produced by modifying the method for adding cadmium precursor into the reaction mixture. An injection needle was immersed in the bacterial medium to avoid initial contact with the organic layer of capping molecules on the surface: this surface reaction was believed to promote otavite formation. Cd ions in precursor solution reacted with $HS^-$ ions in the media, and the color of the reaction mixture changed to a deep orange, potentially due to the large crystal size. After washing with $H_2O$ and ethanol, a toluene extraction was carried out, and it separated the high quality CdS QD materials from the larger, carbonate-free CdS NCs. The color of the extracted CdS is deeper orange than the yellow color of the previously extracted CdS QD despite the same precursor concentration [Inset Fig. 5b-B]. This difference in color was attributed to the high CdS reaction yield without the otavite byproduct. The absorption spectrum of the resulting CdS NCs showed a similar absorption peak at 390 nm.

### 2.1.11.3 SnS

Quantum dimensional tin sulfide (SnS) nanocrystals were also synthesized as the second new nanoparticle candidate by adding a long chain oleylamine during NanoFermentation. The crystal growth incubation time was reduced to 1 day, compared to 5 days for bio SnS NC production. The harvested SnS NCs showed high solubility in ethanol. The TEM analysis resulted in that the capped SnS NC had 2.3±0.8 nm, compared to 6.0±1.4 nm of bioSnS (Figure 1-48). XRD of capped SnS had an ACS of 0.7 nm, compared to 4.3 nm ACS for bio SnS. It corresponds to TEM analysis. FTIR shows no difference between capped NC and bio NC. No fluorescence or absorption features in the UV-Vis-NIR region were observed from bioSnS and oleylamine capped SnS samples consistent with indirect semiconductor behavior. The oleylamine capping reduced the size of bioSnS (1.3 eV) resulting in a higher bandgap (1.6 eV) compared to bulk SnS (1.0 eV). XPS confirmed oleylamine capped SnS.

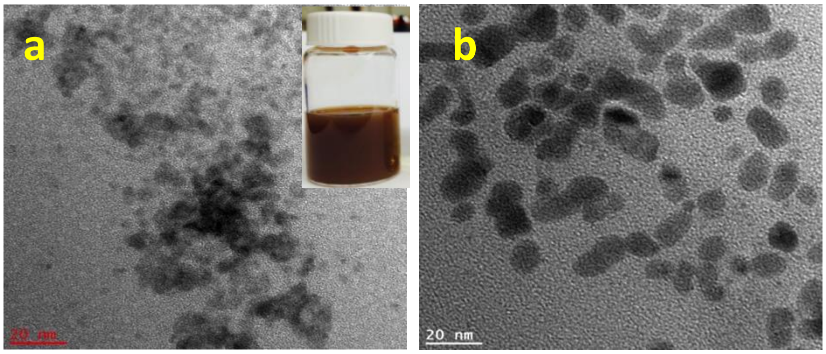

**Figure 1-48.TEM image of oleylamine capped SnS (a) and bio SnS nanocrystals (b). The inset picture shows capped SnS NCs in ethanol, where the colloids were suspended for 5 days**

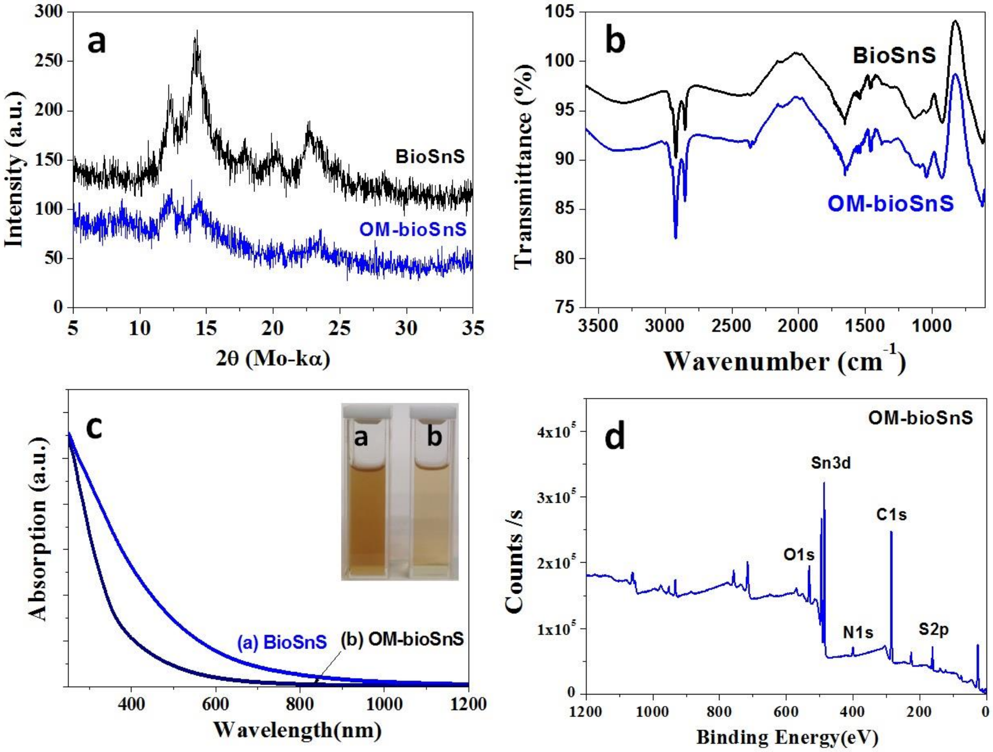

**Figure 1-49. Characteristics of bio and oleylamine capped SnS NCs a) XRD patterns b) FTIR spectra, c) Absorption and emission spectra d) XPS scanning spectra**

### 2.1.12 Produce >50g/month for 2 new materials from 2014

The milestone to “produce >50 g/month for 2 new materials from 2014” was accomplished by successfully producing optical property-enhanced oleylamine-capped CdS quantum dots at >330 g/month and $Ni_3S_4$ as precursor for p-type semiconducting NiO at 50 g/month.

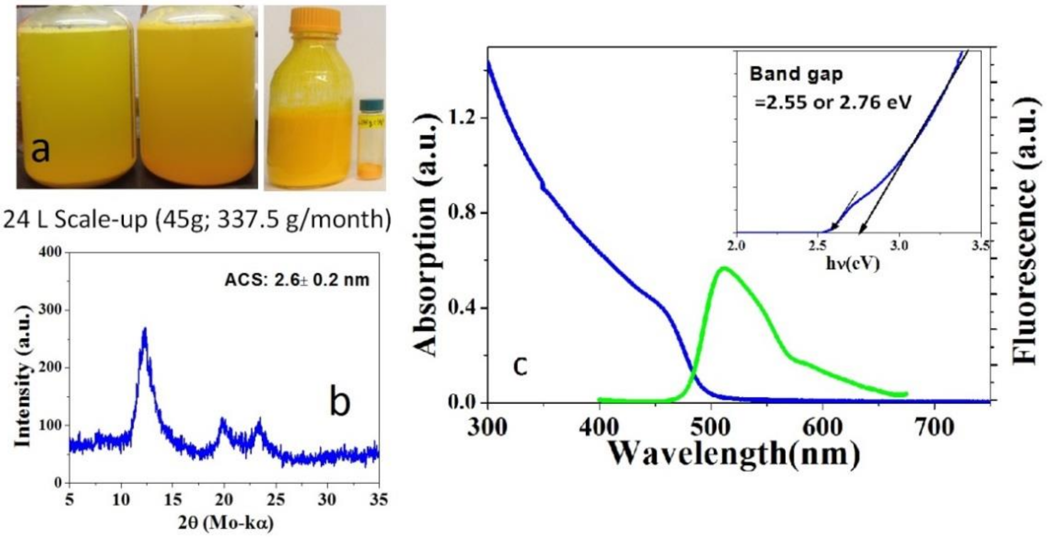

**Figure 1-50. a) 24L scale-up of oleylamine capped CdS NCs and harvested wet and dry samples, b) XRD pattern of as-synthesized oleylamine capped CdS NCs, and c) Absorption and fluorescence spectra of the suspended CdS NC colloid. Inset is a band-gap determination**

The mass production of oleylamine-capped CdS nanocrystals (NCs) for > 50 g/month was carried out in a 24-L reactor. Incubation of bacterial strain X513, 10mM glucose, and 5 mM thiosulfate as an electron acceptor followed by in-situ oleylamine addition (final volume 0.02%) before dosing with 5 mM Cd salt resulted in production of CdS NCs. After 1 day incubation (total 4 days process reaction, 0.5 days preparation, 2 day enrichment, 1 day incubation and 0.5 day harvesting) and following modified harvesting with $H_2O$ and ethanol washing steps (6 times of $H_2O$ rinse for precipitate, 2 times of $H_2O$ centrifuge and 2 times of ethanol centrifugation), the harvested product resulted in 45.0 g of freeze dried powder (Figure 1-50a). This CdS NC method would produce 337.5 g/month. XRD analysis showed the CdS NC powder is the phase of cubic hawleyite without otavite byproducts. It has 2.6 nm of average crystal size (ACS) (Figure 1-50b).

The dried CdS NCs powder was re-dispersed in organic solvents. It appears that fine NCs were soluble in toluene, hexane, formamide and chloroform while agglomerated crystals precipitated in a day. The colloidal CdS NCs suspension in toluene exhibits a characteristic CdS absorption edge at 450 nm and bandgaps at 2.55 or 2.76 eV (vs bulk CdS = 2.42eV) (Figure 1-50c). Depending on the calculation method such as indirect, direct or band edge, the bandgap determination could be variable. The fluorescence emission peak was exhibited at 510 nm (excitation at 350 nm).

**Table 1-6. Characteristics of oleylamine capped CdS NCs according to scale-up process**

| | **BioCdS_24L** | **1st batch_1L** | **2nd batch_1L** | **batch_24L** |
|---|---|---|---|---|
| Cation Dose | 5mM | 5mM | 5mM | 5mM |
| Capping | - | Oleylamine | Oleylamine | Oleylamine |
| TEM (nm) | 16 | 4.5 | - | - |
| XRD (nm) | 6.1 | N/A (CdS+$CdCO_3$) | 2.7 | 2.6 |
| Bandgap(eV) | - | 3.1 | 3.0 | 2.78 |
| Absorption | - | 390 nm | 390 nm | 490 nm |
| Emission (Ex_350nm) | 552nm | 550 nm | 550 nm | 510nm |
| Mass production | 8.1g | - | - | 45g |

Table 1-6 summarizes characteristics of oleylamine capped CdS NC according to scale-up process. The 24 L scale-up produced powder with similar crystallite size to powder from the 1-L scale; however, it showed different optical features. Quantum dot size confinement effect of CdS is very sensitive within 1 nm of size difference for < 4 nm particles.

The second candidate nanoparticle, nickel sulfide in the form of $Ni_3S_4$ as a precursor for p-type semiconducting NiO was produced in a series of metal chalcogenides along with ZnS, CuS, and SnS at a >50 g/month rate and contributed towards roll-to-roll MDF collaborations. As an industry- and EERE-relevant candidate nanoparticle, NiO produced from nickel sulfide through controlled oxidation was tested in 2014. The solubility product of NiS ($3\times10^{-19}$) is higher than those for CdS, CuS, SnS, and ZnS ($10^{-37}$–$10^{-25}$), making it more difficult to control the reaction between dissolved Ni and sulfide ions. A previous synthesis in early 2014 resulted in steep variation in yield and average crystallite size from dual parallel 24-L reactors composed of two 12-L glass carboys (Table 1-7).

The first batch exhibited the improved $Ni_3S_4$ formation by adjusting the stirring speed (rpm) when dosing the Ni precursor and the dosing rate, resulting in narrow yield gap, even though their different suspension behavior was confirmed by difference crystallite size using XRD. However, three recent batches at the 24-L scale had ~10.1 g/6-day reaction yield and successfully achieved the 50 g/month production milestone for Low Temperature Synthesis.

**Table 1-7. Nickel sulfide production as a precursor for NiO**

| NIS | Yield(g) | ACS (nm) | Comment |
|---|---|---|---|
| 131104A01 | 4.62 | 4.7±0.3 | |
| 140224A01 | 1.99 | - | Poor crystallinity |
| 140224B01 | 7.15 | 4.7±0.3 | |
| 140916A01 | 5.12 | 7.3±0.8 | }1st 24L total: 9.2g |
| 140916B01 | 4.08 | 1.2±1.0 | |
| 141004A01 | 11.03 | 7.1±0.7 | 2nd batch |
| 141018A01 | 9.99 | 6.7±1.2 | 3rd batch |

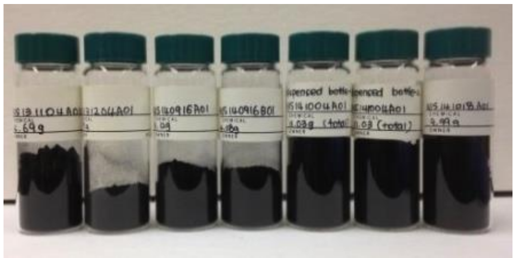

**Figure 1-51. Harvested nickel sulfides**

### 2.1.12.1 Iron nitrides

We continued collaborations with the ARPA-E REACT project team to produce iron nitride using magnetite nanoparticles that were synthesized through NanoFermentation. Two representative magnetite samples for reduced crystallite size of Zn-doped magnetite by doping with 1% and 10% zinc were randomly selected, and their compositions were measured to compare the nominal and actual doping ratio in materials with small crystallite size. At a low doping ratio (1% of Zn) the difference between nominal and tested doping level was small, with 2% variation. However at 10% doping there was a 15% difference due to the different coherency in the magnetite crystal structure caused by different ionic radii and solubility products in the growth medium (Table 1-8).

**Table 1-8. Stoichiometry of Zn-doped magnetite as iron nitride precursors**

| Sample | ICP measurement | | Doping ratio | | | |
|---|---|---|---|---|---|---|
| Zn Doping | Fe (wt%) | Zn (wt%) | by wt % | Δgap | by mol % | Δgap |
| 10% | 58.2 | 6.37 | 9.87 | 0.01 | 8.55 | 0.15 |
| 1% | 62.2 | 0.722 | 1.15 | 0.15 | 0.98 | 0.02 |

The goal is at least 2000 Oe of coercivity and ~200 emu/g of magnetization. An additional production batch of Zn-Fe oxide powder did not improve the iron nitride yield, which decreased from 40-45% to 20%. However, the coercivity remained high (from 1500 Oe to 1100 Oe). The delivered samples contained smaller particles than previous ones, and smaller crystallites are advantageous for gas diffusion. We will continue to adjust reduction and nitridation to get at least ~70% yield.

### 2.1.12.2 ZnS QDs

Using oleylamine as a capping molecule to produce ZnS QD nanocrystals (NCs), we confirmed the expected differences in luminescent and physicochemical features. Comparing to the previous oleate-ZnS QD results, the colloidal QD NCs were more readily suspended in a polar solvent (e.g. ethanol). Furthermore, the concentration was reduced from 0.1 to 0.02 vol.% of oleylamine, while similar sized oleate-ZnS QDs (4 nm) were synthesized (Figure 1-52b). The resulting oleylamine-capped ZnS (olem-ZnS) NCs washed with water and ethanol. In order to remove excess oleylamine and organics, the harvested NCs were subsequently washed with toluene. The resulting colloidal olem-ZnS NCs were re-dispersed in ethanol, and the NCs remained suspended for several days while oleate-ZnS NCs precipitated in a day (Figure 1-52a).

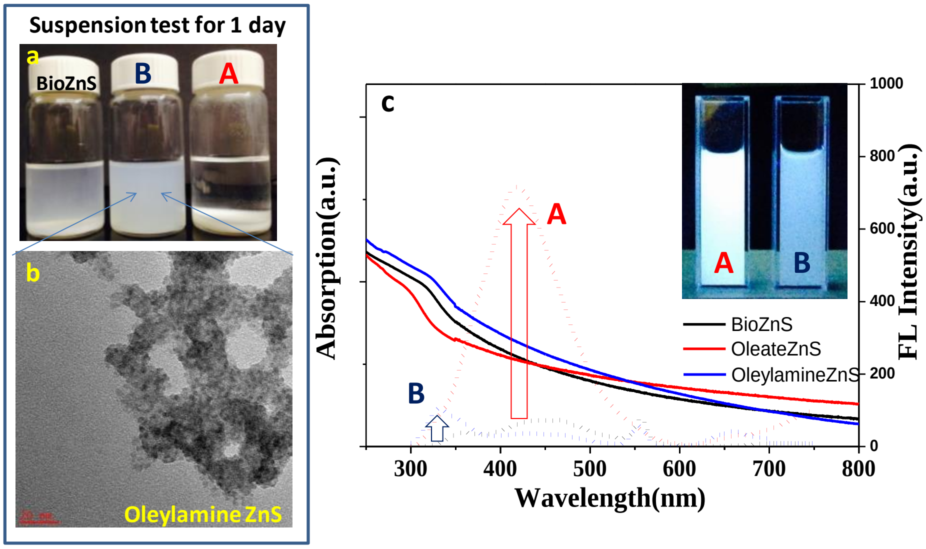

**Figure 1-52. Comparison of biologically produced ZnS nanoparticles. a) Photograph of uncapped, oleylamine (B)- or oleate (A)-capped bio-ZnS; b) TEM image showing oleylamine-capped bio-ZnS; c) Absorption and emission spectra of capped bio-ZnS. Inset shows dispersed oleylamine (B)- or oleate (A)-capped bio-ZnS in deionized water**

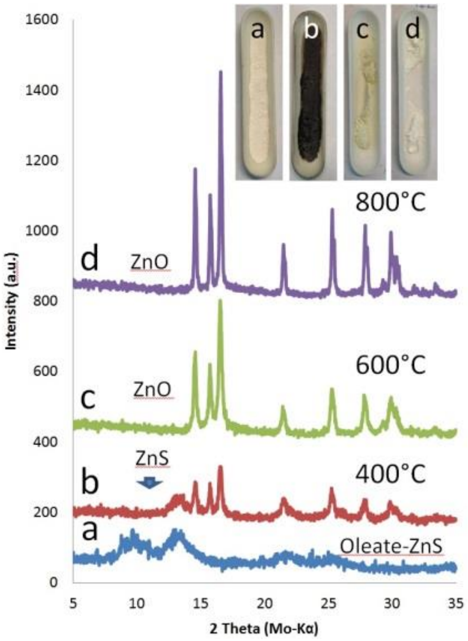

**Figure 1-53. XRD patterns of as-synthesized oleate-ZnS QD and thermal annealed ZnO crystals**

The absorption spectrum of oleylamine-ZnS QDs was different from oleate-ZnS and bio-ZnS. The absorption edge of oleate-ZnS QDs at 325nm shifted red in spite of smaller size (2.4 nm), compared to 10–20 nm of bio-ZnS at 320 nm and 3 nm of oleateZnS at 300 nm. This difference is attributed to a surface passivation of the ZnS NCs due to amine group functionalization and /or its reflective index change by long chain of carbon bond. Interestingly, the fluorescence (FL) emission peak at 330 nm is higher than oleate-ZnS and bio-ZnS; however, the broad peak between 370 and 550 nm is lower than the others. This broad peak between 350 and 550 nm is assigned to three luminescent peaks from surface defects, such as Zn vacancies at 450 nm, S vacancies at 490 nm and the transition of electrons from sulfur vacancy state to zinc states at 515 nm. The FL peak at 330 nm is attributed to the size confinement effect. Therefore oleylamine capping results in size confinement in the quantum dimension, while inducing fewer crystal defects on the NC surface.

Previously made oleate-zinc sulfide QDs were thermally converted to zinc oxide (ZnO) at 600 ºC in air. The ZnS NCs were thermally annealed at 400 ºC, 600 ºC, and 800 ºC in air for 1 hr (Figure 1-53). As-synthesized oleate-ZnS quantum dots showed ZnS crystal XRD pattern with an additional crystal peak at 10º 2θ. This second peak may be due to a carbonate crystal from oleic acid aggregation. At 400 ºC, ZnS was thermally transformed to a ZnO and ZnS mixture. Also, the annealed samples showed a black color due to incomplete combustion of oleic acid and organics, and the additional XRD peak at 10º 2θ disappeared. As annealing temperatures increased, the XRD pattern of single crystalline ZnO increased to 21 nm of ACS at 600 ºC and 47 nm at 800ºC

### 2.1.13 Progressive upscaling 2+ new products at 10g

We exceeded the milestone of “progressive upscaling 2+ new products/y at >10 g” task by producing 1) highly luminescent oleylamine-capped ZnS nanocrystals (ZnS NCs) for > 10 g and 2) ZnS with reduced surface coating and higher dispersivity using an improvised complementary NanoFermentation process.

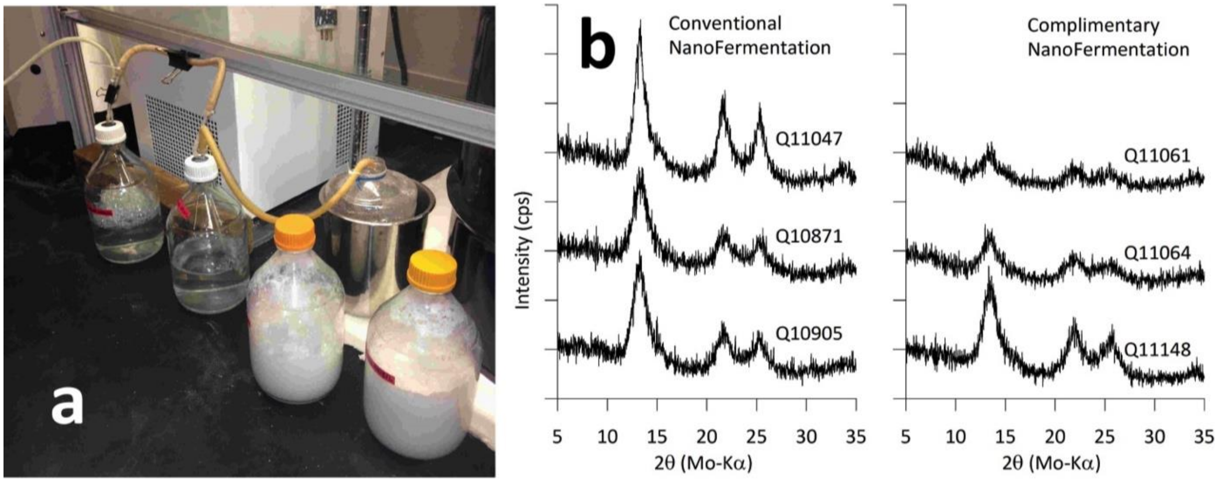

**Figure 1-54. a) Sparging remaining hydrogen sulfide and hydrosulfide in the medium while cooling reactors, b) XRD patterns from conventional and complementary NanoFermentation process**

NanoFermentation occurring in aqueous phase requires microbial activity to reduce metal or sulfur ions and nucleate the formation of various nanoparticles such as magnetic, semiconducting, phosphoric, photovoltaic, and catalytic materials. Generally the surfaces of nanoparticles are covered by fermentation by-products, adsorbed via hydroxyl carbon (C–O) and carbonyl (C=O) groups of acetate and lactate as well as the amine group of amino acids and proteins. During the termination of 100-L and 900-L pilot reactors with cooling, we sparged the vessels with $N_2$ gas to transfer remaining hydrogen sulfide and hydrosulfide into the zinc acetate trap, to protect the final nanoparticle products and avoid discharging a toxic gas as waste.

Within this waste stream ZnS was produced abiotically by the reaction between dissolved zinc acetate and nitrogen-purged hydrogen sulfide gas or dissolved hydrogen sulfide or hydrosulfide as aerosol (Figure 1-54a). The products were comparable to nanomaterials produced using the NanoFermentation technique (Figure 1-54b and Table 1-9). Based on the XRD patterns, average crystallite size (ACS) values for these abiotic ZnS nanocrystals were very similar to nanocrystals producing by NanoFermentation with FeS medium. ZnS nanocrystals produced by cells growing in FM medium were larger, possibly due to a lower pH that increased ACS.

**Table 1-9. Average crystallite size (ACS) and yield from both conventional NanoFermentation and complementary NanoFermentation**

| Sample Name | ACS | Description | Yield | Comment |
|---|---|---|---|---|
| NanoFermentation | | | | |
| Q11047 | 3.0 ± 0.2 nm | FM medium in 900-L | 322g | FY2015Q1 |
| Q10871 | 2.1 ± 0.1 nm | FeS medium in 100-L | 50.2g | FY2014Q4 |
| Q10905 | 2.2 ± 0.1 nm | FeS medium in 100-L | 53.4g | FY2014Q4 |
| Complementary NF | | | | |
| Q11061 | 2.3 ± 0.2 nm | 1M Zinc acetate in DI water | 40.5g | ***FY2015Q2*** |
| Q11062 | 2.0 ± 0.1 nm | 1M Zinc acetate in DI water | 9.17g | ***FY2015Q2*** |
| Q11063 | 1.9 ± 0.1 nm | 1M Zinc acetate in DI water | 13.8g | ***FY2015Q2*** |
| Q11064 | 1.8 ± 0.1 nm | 1M Zinc acetate in DI water | 21.5g | ***FY2015Q2*** |
| Q11148 | 2.1 ± 0.1 nm | 1M Zinc acetate in DI water | 52.7g | ***FY2015Q2*** |

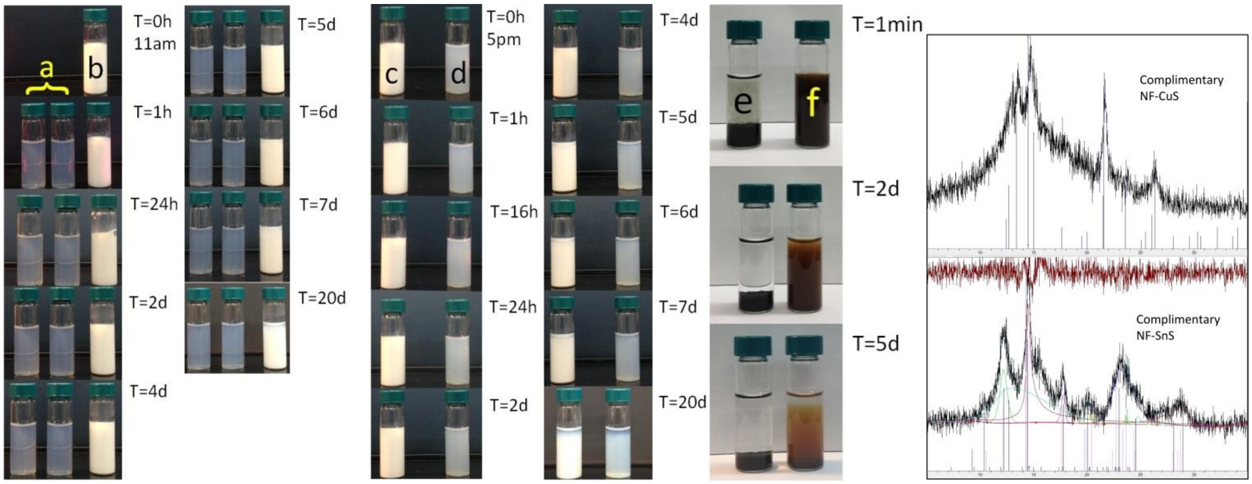

**Figure 1-55. Suspension experiment using ZnS, CuS, and SnS from complementary NanoFermentation. ZnS supernatant from centrifuge of (a) 30 min at 8,000 rpm, (b) 1 min at 3,000 rpm, (c) 1 min at 2,000 rpm, (d) 15 min 8,000 rpm. Sediments of (e) CuS and (f) SnS from sediment of centrifuge of 15 min at 8,000 rpm. XRD patterns from sample (e) CuS and (f) SnS**

Recently ZnS samples produced using the complementary NanoFermentation method (Figure 1-55a to d) had relatively larger ACS (7.3 ± 0.4 nm) size compared to ZnS from the conventional NanoFermentation. This result is similar to the abiotic low carbon medium result we reported previously (See *FY14Q1* report). The abiotic low carbon medium process produced ZnS of 2.5–5.3 nm compared to 1.8–1.9 nm ACS from conventional NanoFermentation. This implies that the microbes act as catalytic nucleation site on their cell surfaces facilitating the production of small crystallites rather than crystal growth. However, the new ZnS nanoparticles generally remained suspended up to 20 days, even though there was some precipitation. In contrast, the new CuS and SnS nanoparticles, as shown in Figure 1-55e and f, respectively, rapidly aggregated and precipitated. Some SnS nanoparticles (6.0 ± 0.4 nm) remained suspended after 2 days. These results suggest that acetate from the Zn acetate precursor constrained the the formation of fine ZnS nanoparticles and reduced aggregation, but it was not effective for SnS and particularly CuS nanoparticles. Future work will investigate alternative capping molecules for CuS and SnS nanoparticle production using complementary NanoFermentation to reduce crystal growth. A large mound of 2 theta 10–20 degree X-ray diffraction from the CuS sample indicates a large amorphous phase, which could help to explain the rapid precipitation.

Three complementary NF ZnS samples were selected from Table 1-9 and their total nitrogen and carbon contents were analyzed using conventional combustion methods. These values were compared to previous NF samples with calibration of gamma $Al_2O_3$ reference material values. Triplicates of complementary NF ZnS samples had lower nitrogen (0.017%) and carbon (0.308%) composition (Figure 1-56) compared to conventional NF ZnS with nitrogen (0.718%) and carbon (2.28%). The complementary NF successfully reduced surface nitrogen and carbon contents in the final nanoparticles at a fraction of 2.3% (N) and 13% (C) of ZnS from conventional NF.

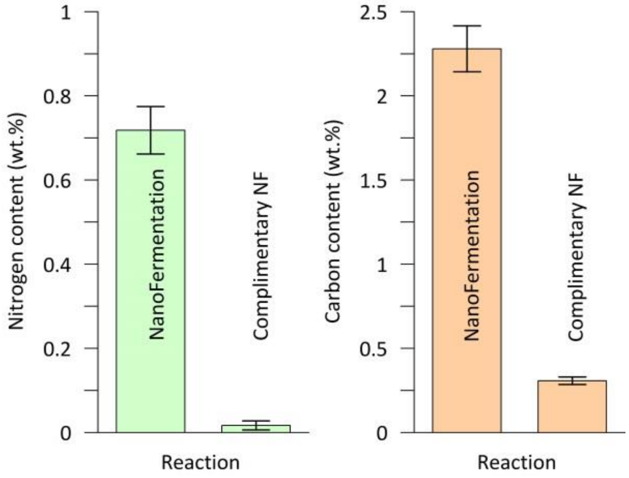

**Figure 1-56. Total nitrogen and carbon analysis of ZnS to compare conventional and complementary NanoFermentation**

The complementary NF samples showed a 98% reduction in N composition compared to an 86% reduction in C. FTIR analysis, as shown in Figure 1-57, demonstrated a significant reduction in the absorbance peak corresponding to primary amines in the complementary NF samples, with relatively larger peaks corresponding to carboxylate bands at 1425 cm$^{-1}$ and 1550 cm$^{-1}$. ZnS from conventional NF showed primary amine (1640 cm$^{-1}$) and shifted carboxylate peaks (1530 cm$^{-1}$ and 1450 cm$^{-1}$) that could easily be shifted by the weak interactions like hydrogen bonding.

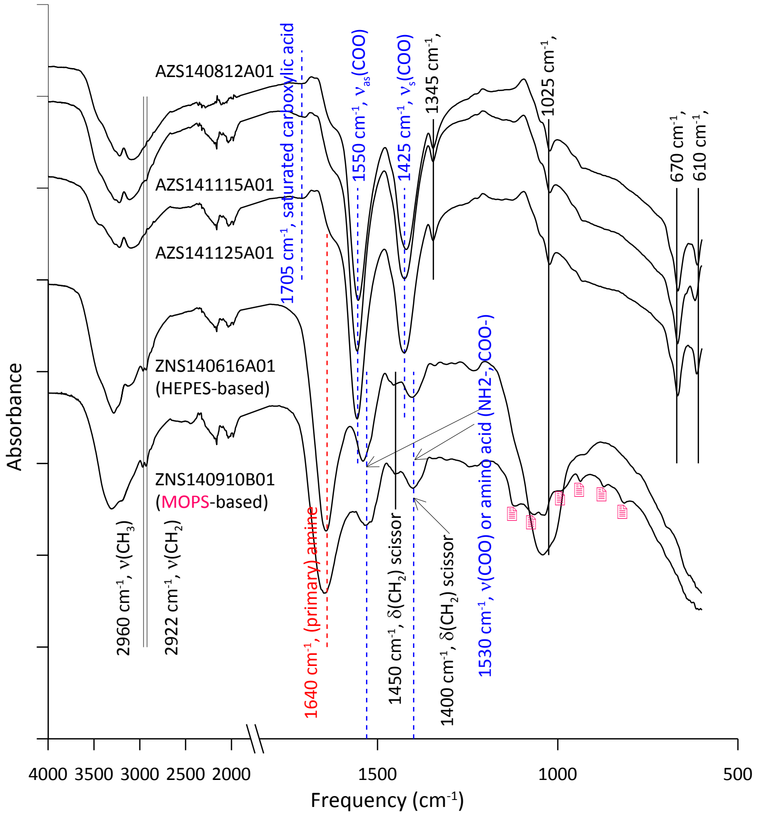

**Figure 1-57. FTIR analysis of ZnS to compare surface coating materials from conventional and complementary NanoFermentation.**

Even though complementary NF ZnS (7.3 nm) and SnS (6.5 nm) had similar ACS; the ACS of ZnS was larger than ZnS from the conventional NF (i.e., 2–3 nm). This difference may be due to the medium composition and pH difference following by different modes of hydrosulfide development. The fact that the ZnS suspension was fairly improved with well-dispersed ZnS despite larger ACS indicates that this ZnS did not form the large aggregates (100–200 nm particles) that we often see in abiotic syntheses. Well dispersed ZnS was confirmed through enhanced optical properties and a blue-shifted bandgap from <3.4 eV to > 3.8eV.

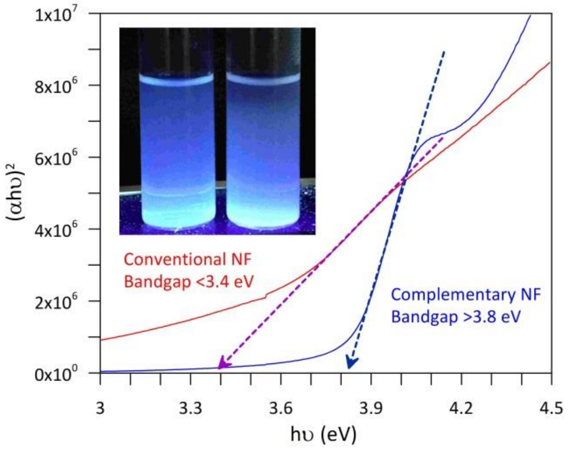

**Figure 1-58. Optical properties and bandgap change. Insets are a and d samples in Figure 1-55 showing similar emission to organic molecule capped bio ZnS**

Considering previous art in U.S. patents, US5,833,855 (Saunders. 1998) used only gene-related sulfate reducing bacteria in the groundwater; US6,337,062 (Akiba, 2002) produced nanoparticles with bubbling very large amounts of expensive $H_2S$ gas from a gas cylinder through metal hydroxide in organic solvents; US8,551,442 (Umino. 2013) used instant formation of $H_2S$ using gasified S and H. Our complementary NF method will also significantly reduce waste streams from NF that require special handling of mixed biohazard and nanomaterials waste (Figure 1-59a). Compared to conventional NanoFermentation (Figure 1-59b) we filed another ORNL invention disclosure titled "*Improved properties of nanomaterials using complementary NanoFermentation technique*" in that gaseous $H_2S$ formation by metal-reducing bacteria with thermodynamic consideration, followed by metal sulfide precipitation in another reaction vessel which can include metal salt and capping molecules controlling the surface and size as well as any chemicals supposed to be toxic to bacteria (Figure 1-59c).

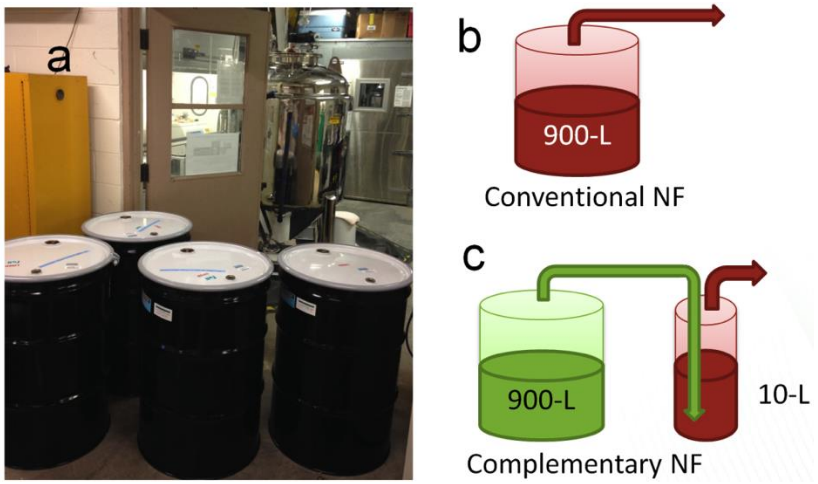

**Figure 1-59. a) Mixed biohazard waste and nanomaterials in large volume, b) conventional NanoFermentation (NF) leaving the whole reaction solution as mixed waste, c) complementary NF leaving small volume of hazardous waste**

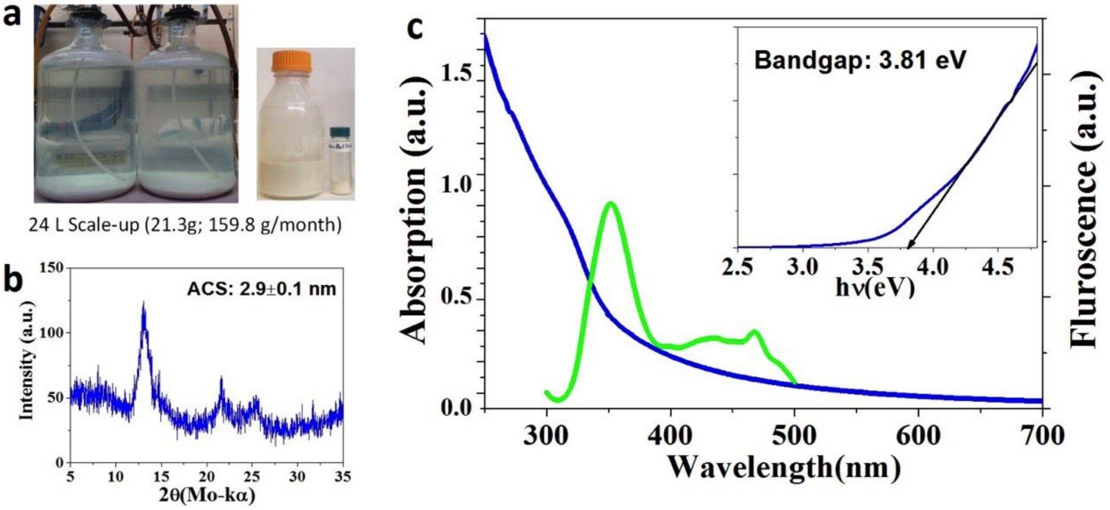

**Figure 1-60. a) 24 L scale-up of oleylamine capped ZnS NCs and harvested wet and dry samples, b) XRD pattern of as-synthesized oleylamine capped ZnS NCs, c) Absorption and fluorescence spectra of the suspended CdS NC colloid. The inset figure shows the band-gap determination**

The mass production of oleylamine capped zinc sulfide nanocrystals (ZnS NCs) for > 10 g yield was carried out in a 24-L reactor. Incubation of metal-reducing bacteria with 5 mM thiosulfate electron acceptor and the *in situ* addition of oleylamine before Zn ion dosing resulted in oleylamine capped ZnS NCs.

After incubation, harvesting and washing, we collected 21.3 g of freeze-dried powder in a 4-day process. This yield corresponds to a productivity of almost 160 g/month. XRD patterns showed the ZnS NC powder was a pure cubic phase of sphalerite (2.9 nm). The ZnS NC powder was re-dispersed in ethanol. The colloidal ZnS NCs suspension exhibited a quantum transition peak at 318 nm with 3.81 eV of bandgap. The NCs have a strong fluorescence emission peak at 365 nm and a relatively low broad peak between 400 and 500 nm, due to quantum size confinement and fewer surface defects, respectively. The optical features corresponded to 1 L scale-up samples. The following Table 1-10 summarizes characteristics of ligand capped ZnS NCs synthesized at large scales.

**Table 1-10. Characteristics of capped ZnS NCs according to scale-up process (*: highest emission)**

| | BioZnS_24L | ZnS_24L | 1st batch_1L | 2nd batch_24L |
|---|---|---|---|---|
| **Cation Dose** | 5mM | 6mM | 5mM | 5mM |
| **Capping** | No | Oleic acid | Oleylamine | Oleylamine |
| **TEM (nm)** | 11.8 | 4 | 4 | - |
| **XRD (nm)** | 6.5 | 1.5 | 1.2 | 2.9 |
| **Bandgap(eV)** | 3.56 | 4.1 | 3.84 | 3.81 |
| **Absorption** | 318 | 300 | N/A | N/A |
| **Emission (Ex_250nm)** | 365/435/468*/506 | 365/435*/468/506 | 365*/435/468/506 | 365*/435/468/506 |
| **Mass production** | 8.1g | 33.0g | - | 21.3g |

### 2.1.13.1 Iron nitrides

We filed an invention disclosure titled "*Low-Cost Precursor for Synthesis of Fe-N Magnet Powders*" devoted to improved synthesis of $Fe_{16}N_2$ nanopowders to be used in Fe-N magnets, specifically by using low-cost, Zn doped Fe-oxide precursors produced by NanoFermentation. The present invention is directed to the use of doped bacteria fermentation Fe-oxide precursors as an improved, low-cost precursor for synthesis of $Fe_{16}N_2$ phase nanopowder. The precursors have been previously developed at ORNL: US Patent 7,060,473 Phelps et al. (June 13, 2006) Fermentative process for making inorganic nanoparticles and US Patent Application 20100184179 Rondinone; Adam J. et al. (July 22, 2010) Microbial-mediated method for metal oxide nanoparticle formation. We have discovered that

1) NanoFermentation-derived nano Fe-oxide precursors show good potential to form $Fe_{16}N_2$ using conventional reduction and nitridation approaches.
2) Low-cost Zn-doped Fe oxide precursors are of an ideal precursor size, and yield high coercivity (> 1500 Oe) $Fe_{16}N_2$ containing powder. This is a surprising result as Zn is diamagnetic and has not previously been considered a candidate dopant to enhance $Fe_{16}N_2$ formation. A further potential advantage of a Zn doped precursor is that the Zn is anticipated to protect the resultant $Fe_{16}N_2$ containing powders from corrosion, particularly when stored prior to consolidation in bulk form. Zn is well known as a galvanizing material to protect steels from corrosion.

## 2.2 EXPANSION OF THE NANOFERMENTATION PLATFORM

This task was designed to expand the $E_h$ (reduction potential) and pH regime of NanoFermentation by adding chemical and electrochemical reducing capacity. Having this capability would enable production of currently unavailable NPs, creating high performance low cost materials for roll-to-roll processing, ferrites, solid state lighting (SSL) and energy storage.

### 2.2.1 Perform initial experiments with reducing agents and characterize yield and product types

The Task 2 was initiated to execute experiments with reducing agents and characterize yield and products. Most experiments have used biomass as a reducing agent and poising agent for Eh. These can also be viewed as control tests to which more stringent experiments will be compared. Experiments using deceased biomass as the reductant are still undergoing analysis but magnetite was produced, though no great benefit has been observed. Experiments where fermentation broth was used as the reducing agent but where biomass had been removed by 0.2 μm filtration did produce very small magnetite nanoparticles – but the particles were of poor crystallinity. Importantly, this showed that used fermentation broth could produce magnetite but because of scarce nucleation sites and paucity of microbial activity the particles were poorly crystalline in short range order.

Magnetite formation had routinely been accomplished by using a ferric iron-composed akaganeite-suspended solution, which had been aged for weeks. This aged ferric source-precursor consistently resulted in high quality magnetites, and this process also facilitated incorporation of other metals as dopants. As an experiment using reduced ferrous iron (ferrous chloride) in addition to freshly dissolved ferric chloride, high quality magnetite was formed. This was the first time highly crystalline magnetite was formed from freshly dissolved salts and the first time reduced (ferrous) iron precursors were used for nanoparticle formation. This success is significant in showing the ability of NanoFermentation to utilize reduced species for direct incorporation into magnetite- utilizing more reduced conditions than previously attained. This also makes the production process more efficient, less costly and open new avenues for nucleation research.

A higher reduction potential experiment was conducted with nitrate to make cerium oxide. However, cerium carbonate precipitated, even though nitrogen gas continuously purged $CO_2$ produced by glucose fermentation.

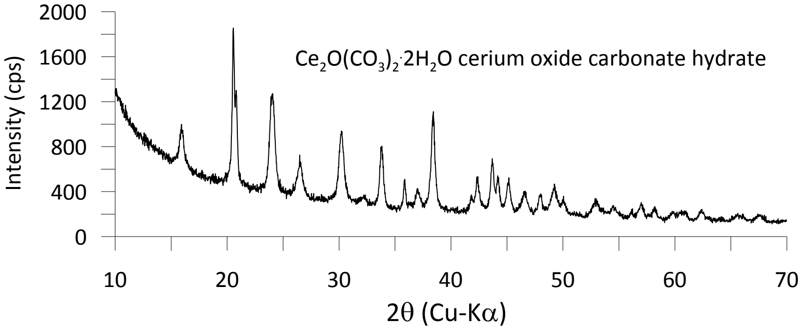

**Figure 2-1. XRD patterns of cerium carbonate while cerium oxide was target**

### 2.2.2 Perform initial experiments by adding electrochemical reductants and characterize yield and product types.

The electrochemical reduction experiments were initiated but metal contamination in the product side of the reaction rendered product examination irrelevant. As expected, our control experiments attempting to abiotically reduce thiosulfate, sulfite or sulfate did not produce nanoparticulates but did reveal metal contamination from the disintegration of the nickel-based anode. The experiments were redesigned to avoid the contamination electrochemical reaction.

Synthesis of NanoFermentation nanoparticles can be also achieved by a chemical reaction in a media including bacteria and a well-controlled nucleation/growth of particles. The driving force of the chemical reaction can be determined in the regime of Pourbaix diagram [potential $E_h$/pH diagram], which describes the equilibrium phases in the reaction. The applicability of the NanoFermentation process to synthesize various nanoparticles significantly depends on the manipulability of Eh and pH in the reactor. This task is to control the regime of $E_h$ and pH to build a wide NanoFermentation platform.

A new elemental copper (Cu) nanoparticle product was made using NanoFermentation, representing an expansion of the $E_h$ regime to +0.340 mV. Although the $E_h$ expansion was in the positive direction the reaction did not occur in controlled experiments and only occurred in low concentration experiments, likely indicating advantages of bacterial metabolism and perhaps nucleation. The elemental Cu was produced at the suggestion of an industrial entity with an active ORNL-material transfer agreement. Various concentration ranges of $Cu^{2+}$ were examined in hopes of producing elemental Cu ($Cu^0$) (Figure 2-2a and b). Only 2mM dosing of $Cu^{2+}$ samples produced elemental Cu. At dosing levels of more than 10 mM samples produced copper ($Cu^{2+}$) chloride. A second batch was examined in attempts to make smaller particles with shorter incubation times. A time course experiment with 2mM single dosing resulted in the appropriate phase change to Cu between 48 and 72 hrs (Figure 2-2c). Our products roughly ranged between 100–150 nm ACS as estimated using XRD patterns. This compared favorably to commercial products, which contain 700 nm and 7 micron elemental Cu products. Initial experiments performed at the test tube scale had production times less than 72 hr at yields approximating 130 mg/L suggesting approximate monthly yields could easily be in the g/L/mo range typical of many of our products.

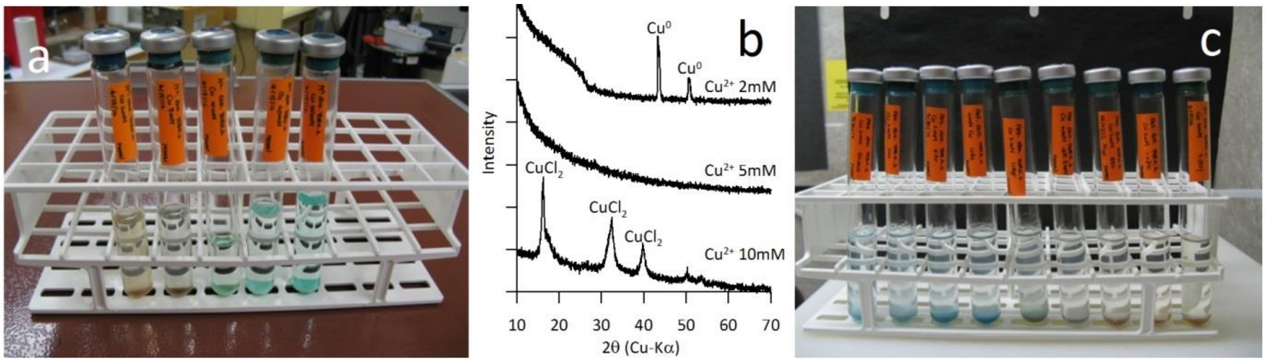

**Figure 2-2. Elemental copper synthesis using microbial activities with a) various input concentrations and b) their XRD patterns, and c) time course experiment with 2mM $Cu^{2+}$ dosing. Precipitation of nanoparticulate elemental copper was evidenced by a beige-to-brown precipitate**

In experiments expanding the $E_h$ towards the more reduced end we observed ZnS nanoparticles in a lower $E_h$ regime with the addition of exogenously added reducing agents supplemented with sodium sulfide. We investigated the influence of a reducing agent, cysteine-sulfide in abiotic conditions on the expansion of the regime of $E_h$. XRD patterns indicated the potential presence of ZnS nanoparticles. Cellular metabolism likely had no involvement with sulfide formation and this production (if valid and reproducible) of ZnS nanoparticles may represent a nucleation pathway with potentially higher yields. Figure 2-3 shows the XRD patterns of ZnS nanoparticles prepared in the media with bacteria including sodium thiosulfate and in the media without bacteria including cysteine-sulfide. The unexpected evidence suggests that there was potential for ZnS to be synthesized in the media including cysteine-sulfide even at low or perhaps even no biomass.

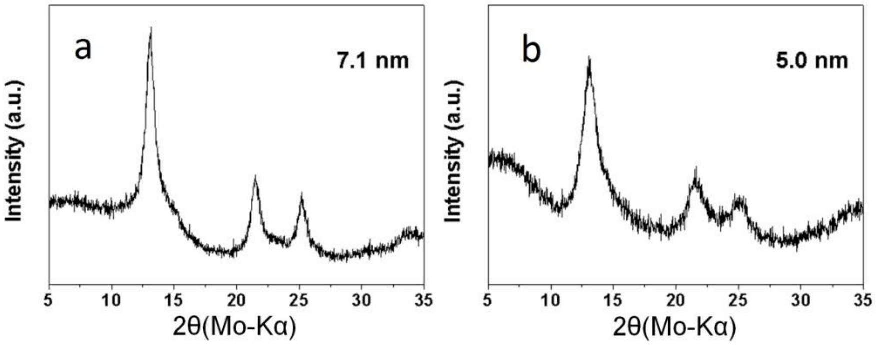

**Figure 2-3. XRD patterns from a) traditional bio-synthesized ZnS and b) XRD pattern of media without bacteria including cysteine-sulfide**

### 2.2.3 Demonstrate a new product from electrochemical reduction experiment at >1 g scale

The development of expanded $E_h$ conditions was continued to produce high purity ZnS by taking advantage of low redox conditions. As shown in Figure 2-4, synthesis of ZnS has been achieved in a low organic carbon medium with less than 0.3 g/L of soluble organic carbon at a pH value less than 6.6. utilizing low redox conditions poised by cysteine-sulfide, compared to traditional microbiological medium had ~9.5g/L soluble organics. Figure 2-5 also shows that crystallite size formed in the low organic medium exhibit slightly larger size, averaging ~10 nm by XRD and likely in the ~15 nm range by TEM compared to NanoFermented ZnS after pH conditioning.

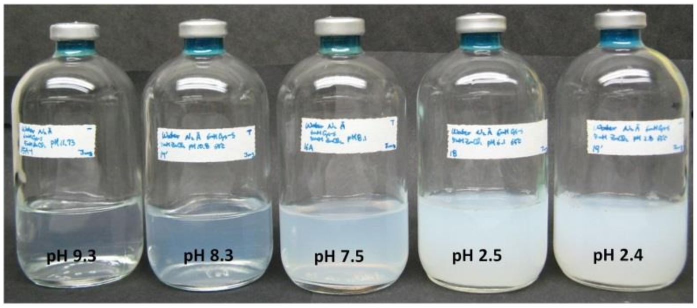

**Figure 2-4. Picture of ZnS from the low carbon medium according to different pH conditions**

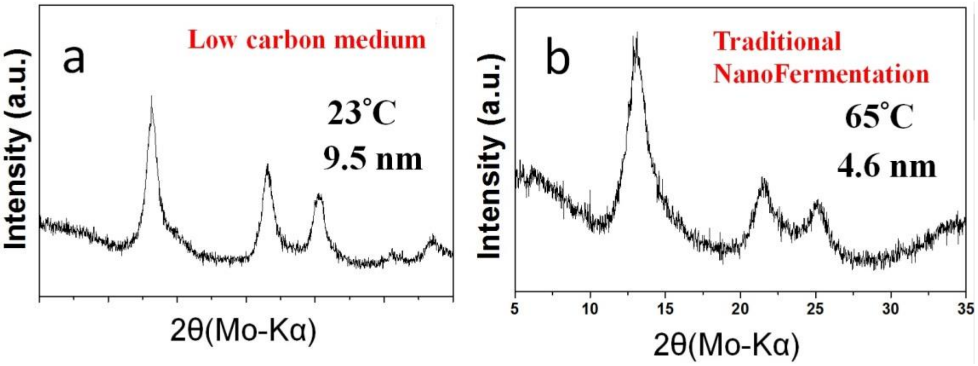

**Figure 2-5. XRD patterns of ZnS from either low carbon medium abiotically or traditional NanoFermentation**

Synthesis of ZnS nanoparticles using a low organic carbon medium was initiated by adding 5–25 mM cysteine-sulfide into degassed deionized water by controlling pH to ~5.5 and then adding discretely 5 or 25 mM zinc chloride into the solution for 5 days.

Figure 2-6 below shows the cleaner FTIR scans for the ZnS produced in low organic media in contrast to the numerous organic peaks associated with traditional NanoFermentation ZnS. It appears the ZnS produced in the low organic route has significantly fewer peaks as well as less area under each of the peaks associated with organics.

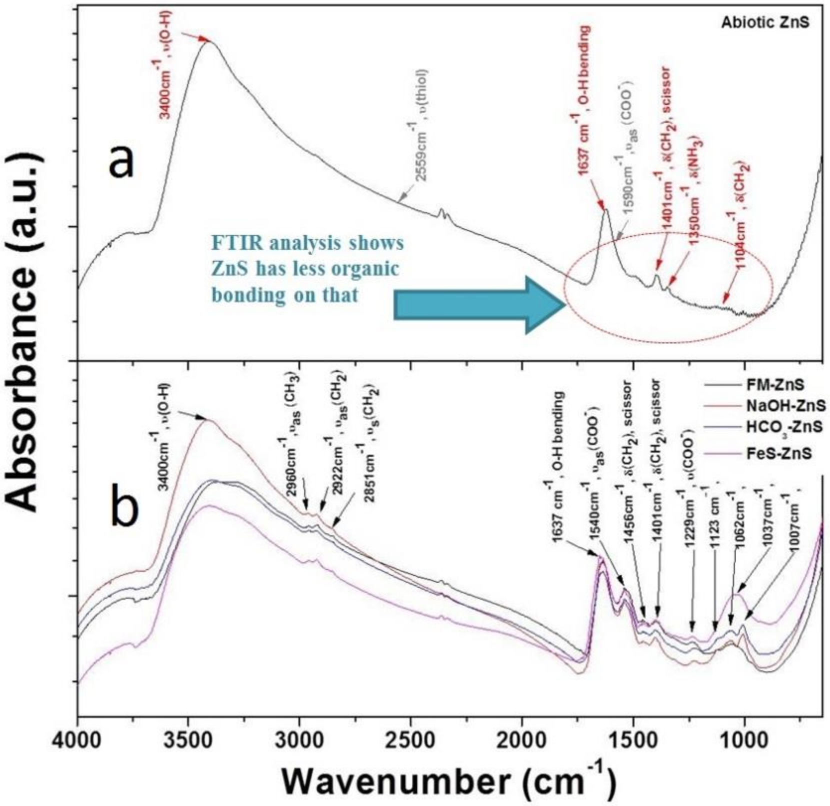

**Figure 2-6. FTIR analysis of the ZnS produced using a) the low organic carbon medium and b) the traditional NanoFermentation medium. The former indicated significantly reduced organics in the range of 1,000–1,750 $cm^{-1}$**

The evidence suggests potential for ZnS to be synthesized and scaled in the media including cysteine-sulfide even at low or perhaps even no biomass. A 10% ink of the newly produced ZnS from low carbon media has been provided to collaborators for assessment as inks and utility for making films.

### 2.2.4 Demonstrate greater than 50% increase in yield or new product type from altered $E_h$/pH

We demonstrated >50% increase yield per liter of fermentor volume or time as a result of advances derived from the altered $E_h$/pH experiments. This milestone was exceeded with an increase of about 500% in yields of ZnS nanoparticles from 2.1g/L/month at 65°C (based on previous protocol) to abiotically produced ZnS nanoparticles of 10.4 g/L/month.

The $E_h$/pH production of ZnS has been explored with the size of ZnS controlled by the concentration of reducing agents, which have a dual role of surfactant. ZnS nanoparticles were synthesized by dosing of

$ZnCl_2$ precursors in degassed water with cysteine-sulfide (Cys-s) under careful pH control. As shown in Figure 2-7, the reactions were carried out at different temperatures. The yields of ZnS nanoparticles were not dependent of the reaction temperature. The ACS was slightly reduced with decrease in reaction temperature. The reaction time and the concentration of $ZnCl_2$ precursors in the reactor of the fixed volume have been investigated to enhance the yield. Figure 2-8 shows the yields and ACS of prepared ZnS nanoparticles depending on reaction time up to 18 hours. The yields and ACS were saturated after the reaction of 18 hours.

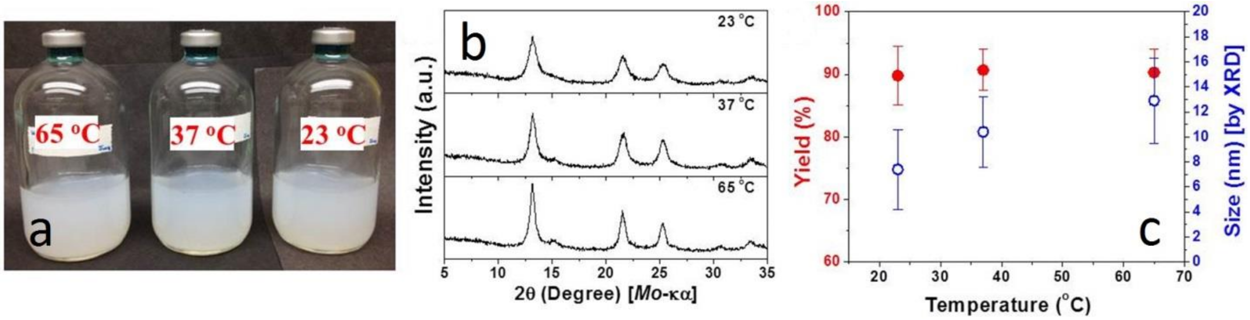

**Figure 2-7. Temperature-dependent reactions for the synthesis of ZnS nanoparticles. a) synthesis in 50 ml scale, b) X-ray diffraction patterns, and c) temperature-dependent yield and size of ZnS nanoparticles**

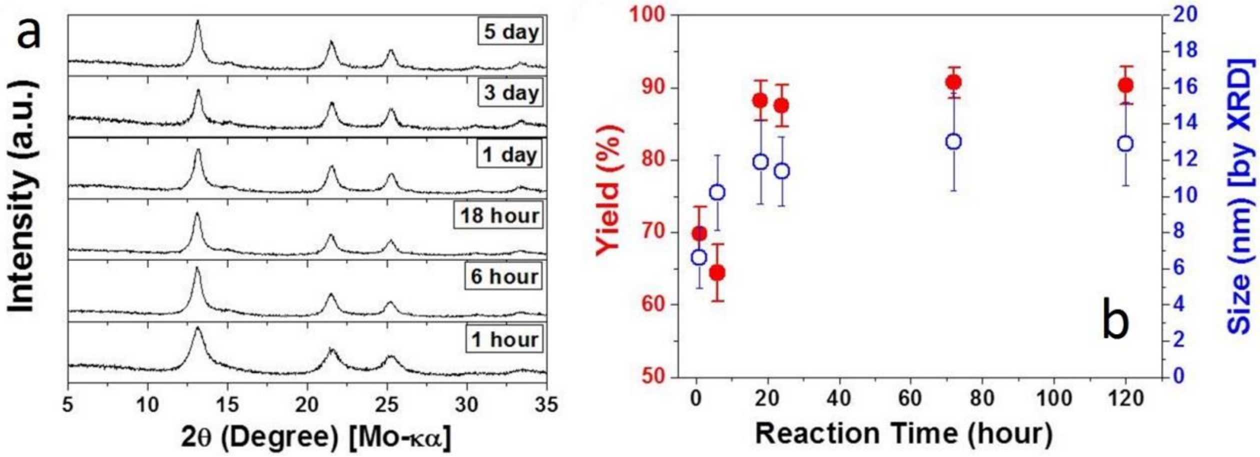

**Figure 2-8. ZnS synthesis by Eh/pH depending on reaction time. a) X-ray diffraction patterns and b) reaction time-dependent yield and ACS**

In addition to reducing reaction time as an approach to enhance yields, increasing reactant concentration has been studied. As shown in Figure 2-9, the concentration of $ZnCl_2$ precursor was varied from 5 mM to 25 mM in the fixed volume of 50 mL. The discrete dosing of 25 mM $ZnCl_2$ (5 times dosing of 5 mM/day based on the previous reaction time study) shows 5 times increase in yields with slight increase of ACS.

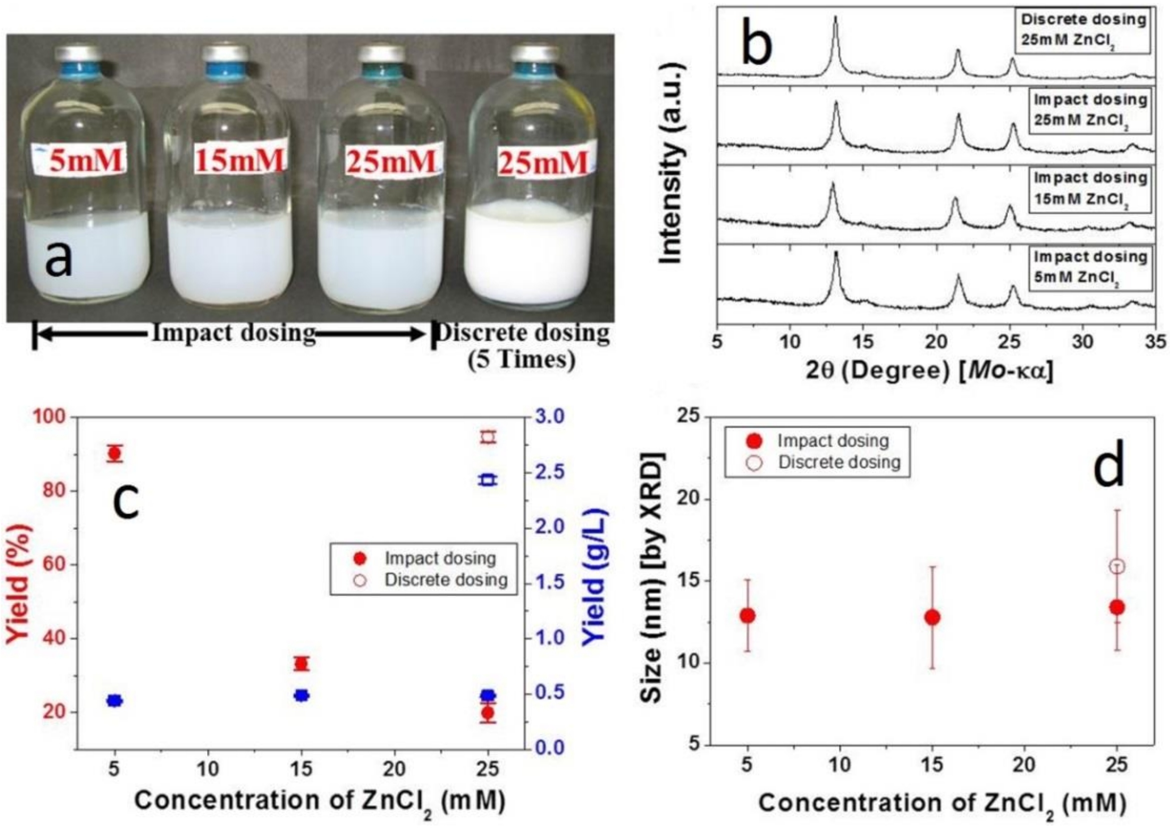

**Figure 2-9. ZnS synthesis depending on impact dosing and discrete dosing of $ZnCl_2$ with different concentration: reaction time. a) dosing different concentration with $ZnCl_2$ in 50 ml scale, b) X-ray diffraction patterns, and c) yield and d) size of ZnS nanoparticles depending on concentration**

Moreover, the ACS of ZnS has been modulated by the control of the ratio of cysteine to $Na_2S$ from 1:1 to 1:50. The Cys-S complex plays dual roles as a reducing agent and a surfactant for the synthesis of ZnS. The ACS of ZnS nanoparticles were characterized by XRD and TEM analysis. The difference of ACS between TEM and X-ray diffraction patterns might be due to the broader peaks measured by the X-ray instrument. However, the trend of TEM size variation depending on the ratio of cysteine to $Na_2S$ corresponds with XRD analysis resulting in the size change from 4.2 nm to 10.7 nm.

### 2.2.5 Identify the second new nanoparticle product for upscaling from altered $E_h$/pH experiments

The new products were synthesized from an electrochemical approach, as another electron donor using a direct current (DC), in gram quantities. Our focus was exceeded in that we realized the electrochemical production of >1 g quantities of Cd particles heretofore not possible through our bacterially based low temperature syntheses. Importantly, the process has been submitted as a patent application "Electrochemical Method for Synthesizing Metal-Containing Particles and Other Objects". The subject provisional patent application was filed in the U.S. Patent and Trademark Office on March 12, 2013 and has been assigned U.S. Serial No. 61/777,009.

To expand the pH-$E_h$ regime beyond conditions that microbes can create we adapted our patent pending electrochemical synthetic process. Growth of CdS nanoparticles was electrochemically initiated as follows: cadmium chloride and sodium thiosulfate were dissolved in an acetate buffer comprised of: 8 mM $CdCl_2$, 10 mM sodium thiosulfate, and 340 mM sodium acetate. The pH was adjusted to 4.5 because acidic conditions usually required less reductive conditions so that we could detect the reaction more easily. The acetate also acted as both a buffer and a chelator to help control nanoparticle particle growth. A graphene electrode with about 1.5 $cm^2$ surface area was placed into the solution and held at -850 mV vs. Ag/AgCl (-645 mV vs. standard hydrogen electrode) using platinum wire netting as a counter-electrode and a Ag/AgCl reference electrode. The solution was sparged with nitrogen gas for 20 minute before the reaction as well as continuously throughout the experiment. The solution was stirred at 150 rpm.

The graphene electrode was prepared as follows: graphene nanopetals were grown at ~800 $^{o}$C in a direct-current plasma, chemical vapor deposition reactor. Growth was on a silicon wafer either directly or on a nickel layer on top of the silicon wafer, using methane as a carbon source, with trace ammonia vapor present to assist in the reaction. The growth reaction required about 10 minutes. The wafer was then cooled, removed and cleaved, before use. The graphene nanopetals assisted in making nanoparticles that sloughed off from the electrode in contrast the more typical electroplating that could have occurred instead of nanoparticle formation. During this run, based on 50 mL precursor solution, we added an additional 1.5 mL of 1M $CdCl_2$ solution to get more CdS. After maintaining the potential for 30 hours, we obtained 0.173 g of black precipitate, which was identified as elemental cadmium using XRD (Figure 2-10). This represented about 81% recovery of the input amount. This verified the electrochemical mimicking of nanoparticle formation.

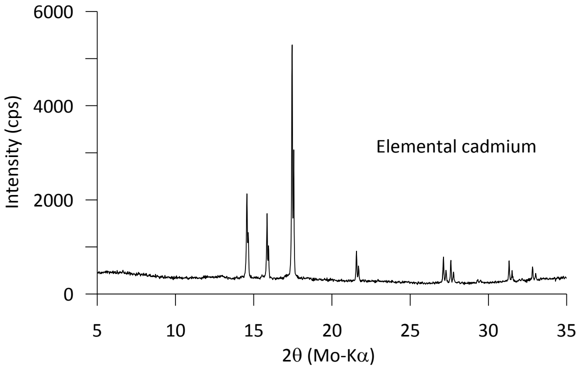

**Figure 2-10. X-ray diffraction patterns of black precipitation from the electrochemically driven production of nanoparticles mimicking our biological low temperature synthesis technique**

We attempted to upscale the process (Figure 2-11a and b) using the same conditions in a 360 mL volume except no additional Cd was added and the reaction was continued for 24 hours. With less reaction time of 24 hr compared to 30 hr, the system produced 0.071 g, which was about 22% recovery.

As an improvement to increase the yield and recovery of the 360 mL system we clearly defined the working electrode area by painting enamel on the electrode as insulator (Figure 2-11c). The graphene working electrode produced particles, which mostly end up in solution but a small amount remained bound to the electrode, so we added sonication. Sonication was accomplished using a cycle composed of 1 second on- and 59 seconds off-duty at 500 watt/20kHz using a 6 mm diameter sonication horn hanging adjacent to the grapheme electrode. For these experiments we used 300 mL precursor solution and 20 mL of 1M $CdCl_2$ stock solution (Figure 2-12a).  Because of the sufficient off-duty cycle time with only short bursts of energy there was no buildup of heat above room temperature, yet the vibrational energies were sufficient to remove particles from the grapheme and dispersed them into the solution as shown in Figure 2-10.

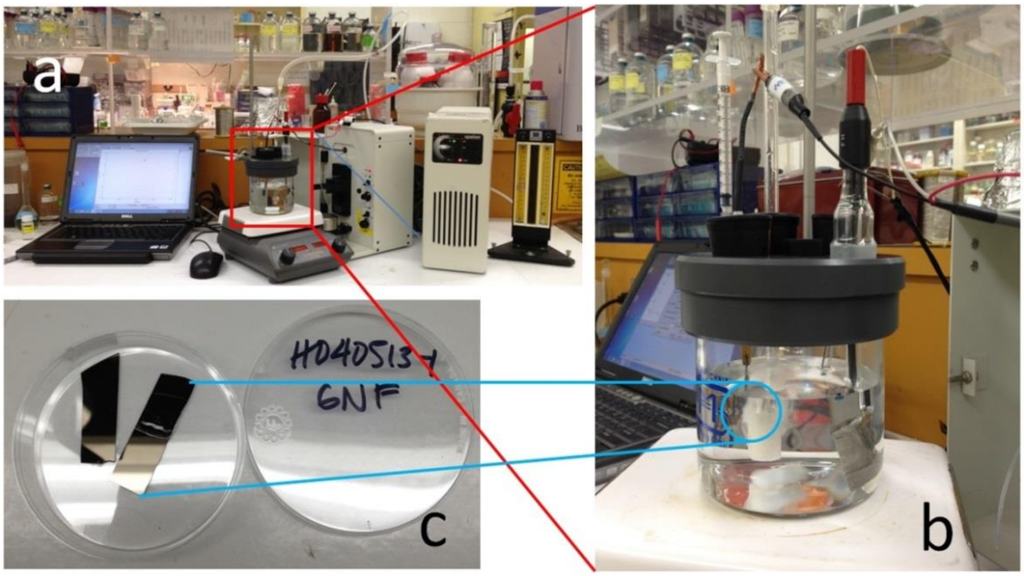

**Figure 2-11. a) electrochemistry system to produce CdS quantum dots, b) reaction cell including 360 mL precursor solution, and c) graphene working electrode with 1.5 cm$^2$ surface on silicon wafer**

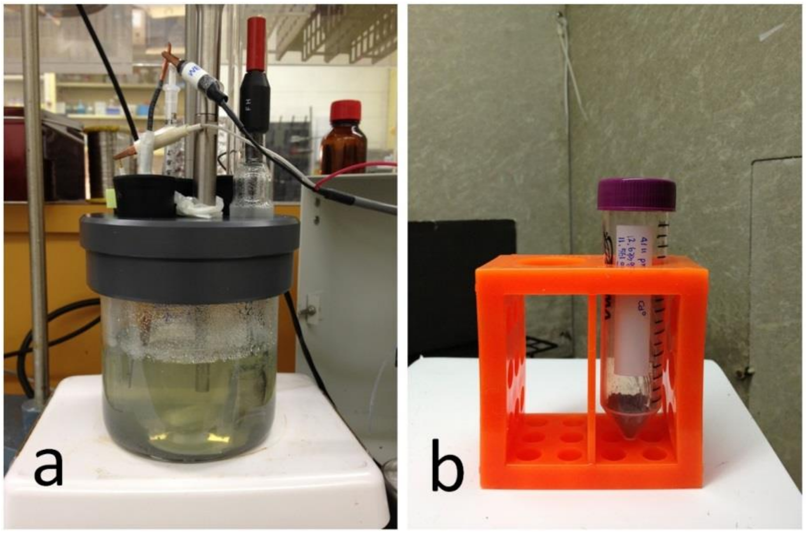

**Figure 2-12. Electrochemical synthesis of elemental cadmium. a) Reaction cell equipped with sonicator, b) harvested 1.07 g of elemental cadmium**

Even though scale-up using increased volume or increased concentration can increase the amount of precipitate, the recovery percentage was decreased, because the reaction kinetics were proportional to the electrode surface area. We increased the graphene electrode area from 1.5 cm$^2$ to 2.27 cm$^2$ with the same auxiliary platinum electrode and the particles attached to the electrode were sloughed off every minute. This produced more than 1 g of elemental cadmium particles with a yield of 41.7% (Figure 2-12b), even though the volume and concentration were increased.

A key factor of the sonication can be evidenced by current flow on the electrode surface under controlled potential electrolysis. Without sonication the layer of Cd deposited on the electrode hindered more reduction of cadmium ions on the surface, but the use of sonication-enforced detachment facilitated more reaction. Importantly we realized the electrochemical production of 1.07 g quantities of particles heretofore not possible through our bacterially based low temperature syntheses. However, a key factor of the electrochemistry producing elemental cadmium was that overly loaded reduced cadmium sloughed off from the previously deposited elemental cadmium layers on the graphene electrode. Also the graphene electrode lost its surface property after around 72 hr of use. Also noteworthy is that the reaction is proportional to the surface area of the electrode, which may make scale-up difficult. Importantly, we now have more flexibility in our nanoparticle production capabilities.

### 2.2.6 Demonstrate >1g batch from the second new product from altered $E_h$/pH experiments

The expansion of the $E_h$/pH regime through the electrochemical production route produced new types of nanomaterials such as >1 g of zero-valent Cd. The milestone of >1 g was achieved using the process pictured in Figure 2-11 and 2-12. The yield and quality were subsequently improved as a process was developed for making predominantly $Cd^0$ as shown in Figure 2-13. Previously, mixtures of CdS or $Cd(OH)_2$ were produced but now $Cd^0$ is the only major predominant product at >1 g yield.

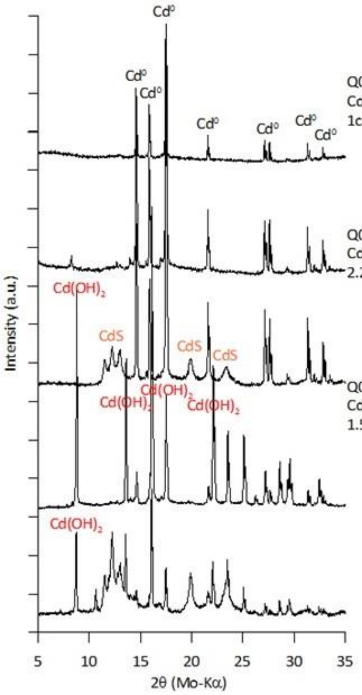

**Figure 2-13. Electrochemical production of $Cd^0$. XRD data show the procedure for $Cd^0$ production**

Another major focus was to demonstrate a new approach to expand the pH- $E_h$ regime as a means to produce multiple types on nano-dimensioned metal-oxides. Controlled oxidation could open a new paradigm using our NanoFermented particles. The fundamental idea is that our nanoparticles as starting materials would keep their nano-dimension size even after oxidation such as annealing or pulsed thermal processing. The synthesis of ZnO NPs has emerged as a fast-growing field. Zinc oxide is an n-type wide bandgap (3.37eV) semiconductor material. The potential application areas include transparent electronics, UV light emitters, piezoelectric devices, biosensors, gas and chemical sensors, and photocatalysis. This indicates that well-defined metal oxide phases can be produced by controlled post-growth oxidation using NanoFermented metal sulfide nanoparticles as starting materials. As shown in Figure 2-14, well-defined crystalline ZnS NPs (Figure 2-14a) were not influenced by controlled annealing in an oxygen atmosphere at 400 °C (Figure 2-14b). However, 30 minute annealing at 600 °C resulted in a highly crystalline ZnO phase (Figure 2-14c).

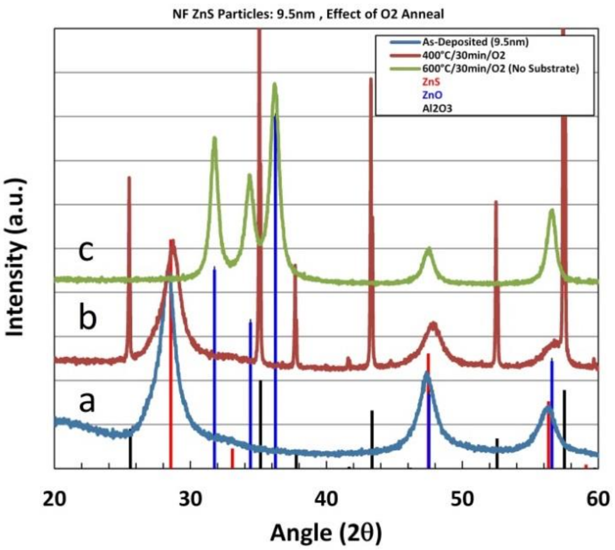

**Figure 2-14. X-ray diffraction patterns of phase change from ZnS to ZnO after controlled annealing**

We attempted to apply this controlled oxidation process to CuS and SnS. Controlled oxidation successfully produced metal oxides such as CuO and $SnO_2$ (Figure 2-15a and b). CuO is attractive for catalytic, solar cell, optoelectronic, and gas sensing applications. Studies on cupric oxide nanomaterials have grown substantially in recent years, because of its direct bandgap (1.2 eV) and intrinsic p-type behavior and good electrochemical properties. The sizes of annealed $SnO_2$ nanoparticles were relatively small compared to CuO.

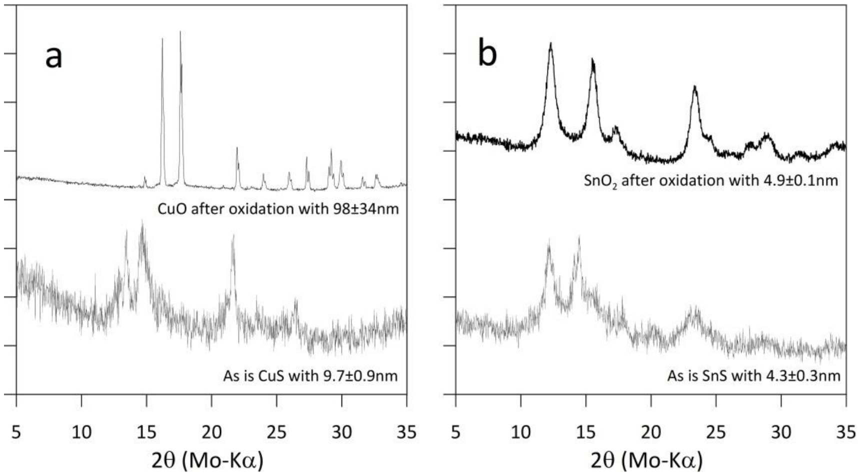

**Figure 2-15. X-ray diffraction patterns of controlled oxidation of a) CuS to CuO and b) SnS to $SnO_2$**

This approach was expanded to produce various metal oxides such as nickel oxide and cobalt oxide. We tested the production of nickel sulfide and cobalt sulfide (Figure 2-16a and b) that can be used in attempts to make their metal oxides. Depending on medium composition and condition, some nickel sulfide trace was identified at the test tube 10-mL scale. A 1-L scale was also produced (Figure 2-16c). These oxide materials are attractive for high-energy storage capacitors, carrier-selective interlayers in organic solar cells, catalytic activators, and thermistor applications. Nickel oxide is a wide bandgap (3.6–4.0 eV) transition metal oxide semiconductor. Depending on the composition, nickel oxides are good capacitors, but can also act as resistors and even as insulating materials. Pure nickel oxides are good high-temperature insulators. In combination with other metals, nickel oxide can act as a conductor. CoO has an energy bandgap of 2.2–2.8 eV whereas $Co_3O_4$ is 1.4–1.8 eV. Pure phase NiS and CoS will undergo controlled oxidation process in trying to make their oxides in future planned experiments.

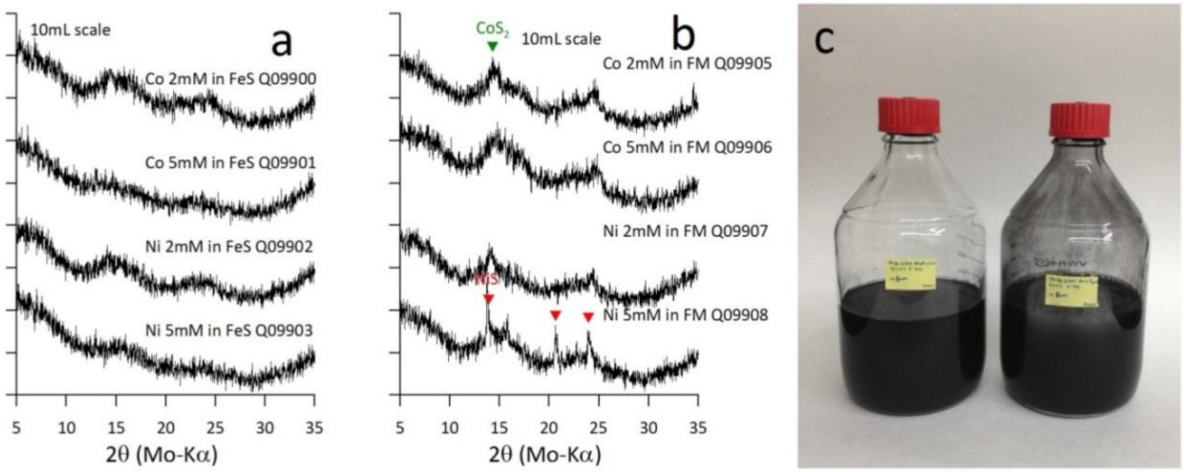

**Figure 2-16. Test tube scale (10mL) of Cobalt sulfide and nickel sulfide in different medium (a and b) and 1L (c) under investigation**

### 2.2.7 Demonstrate upscaling >1g batches from expanded $E_h$/pH platform

More than 1 g products of a second new $E_h$ /pH product were made, 1.4 g of nickel sulfide. Cobalt sulfide was also successfully produced but the yield was only 0.67g. Quality was improved by varying dosing method and timing. The best 1 L FM medium bottles produced a high quality Ni-S complex of 0.76g $Ni_3S_4$ with crystallite size of ~5nm, in contrast Co-S complex using 1 L medium scale produced a 0.67g batch of $CoS_2$ (Figure 2-17).

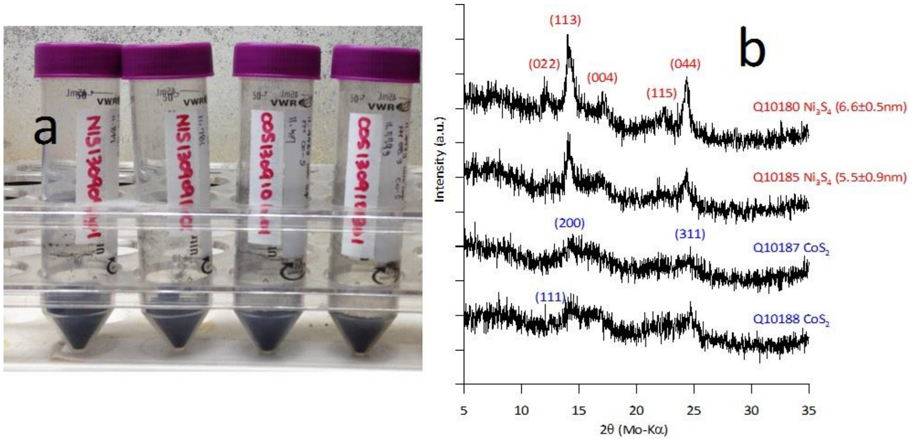

**Figure 2-17. Freeze dried Ni-S and Co-S complex precipitates and X-ray diffraction patterns**

Ni-S and Co-S complexes were not found in stoichiometric NiS and CoS with 1:1 ratio. A reasonable explanation might be that the solubility products of these sulfides likely play roles determining the final products. For example, CdS ($8\times10^{-28}$), CuS ($6\times10^{-37}$), SnS ($1\times10^{-26}$), and ZnS ($2\times10^{-25}$) have low solubility products in contrast to CoS ($4\times10^{-21}$) and NiS ($3\times10^{-19}$). Therefore the former group could be easily determined as their stoichiometric phases, but the latter group resulted in non-stoichiometric complexes.

We also pursued the synthesis of size-controlled elemental copper (Cu). Currently, Cu and copper oxide ($Cu_2O$) particles are synthesized in abiotic and biotic conditions. General preparation protocols including cell enrichment conditions, dosing of Cu precursor (cupric chloride) and its incubation time were followed by the previous elemental Cu powder synthesis method. Various chemical additives and their optimized nanoparticle (NP) growth conditions were examined in order to control average crystal size and stabilize elemental Cu NP from oxidation under ambient environment. XRD patterns and in situ UV-vis absorption measurements showed that the inoculated cupric ions were reduced to Cu NPs via extracellular fermentation at 3 days in Figure 2-18(2) and their growth rate was facilitated by an addition of chelating agent (NTA; nitrilotriacetic acid) in Figure 2-18(3). For biotic Cu NPs, during 3 days incubation, a representative blue cupric solution, as shown in inset Figure 2-18(1), changed to yellow reddish color and fine red powders were precipitated as illustrated in inset Figure 2-18(2).

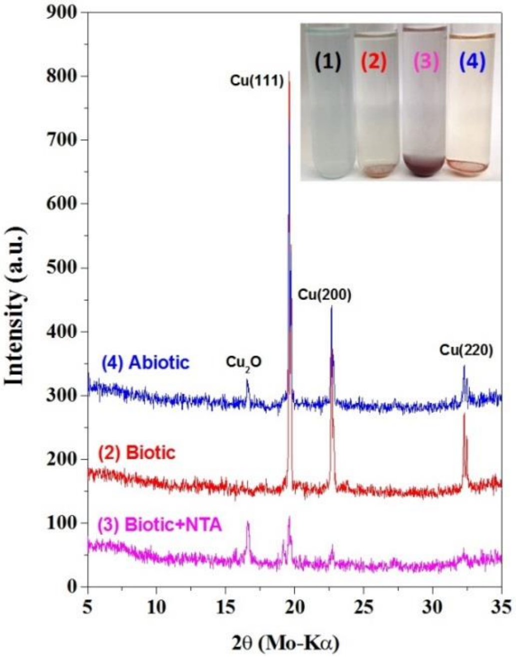

**Figure 2-18. XRD patterns for powders separated from NanoFermentation. Inset is a photograph of Cu NP formation procedure; (1) Precursor ($CuCl_2$) inoculation, (2) Cu incubation for 3 days [Biotic Cu NP], (3) NTA inoculation during 2 days Cu incubation [Facilitated biotic Cu NP], and (4) Abiotic Cu incubation for 2 days [Abiotic Cu NP].**

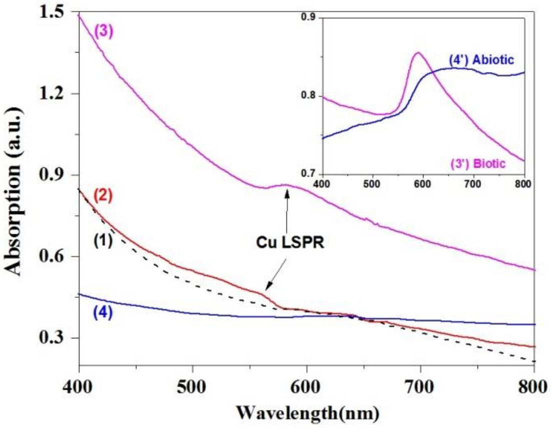

**Figure 2-19. Corresponding in situ absorption spectra of each Cu NP formation; Inset is spectra of redispersed Cu NPs in methanol. ((3') NTA facilitated biotic Cu NP& (4') Abiotic Cu NP)**

In situ UV-vis absorption spectra indicated that the Cu precursor solution (Figure 2-19(1)) formed biotic Cu NPs exhibiting a representative Cu localized surface plasmonic resonance (LSPR) peak at ~560 nm in Figure 2-19(2). Also, XRD suggested that the harvested powders were elemental Cu with over 100 nm of ACS (Figure 2-18(2)). To facilitate the growth of Cu NP, NTA as a chelating agent was inoculated at 2 day Cu incubation. After NTA addition for 60 min, the blue precursor solution gradually turned to reddish and burgundy color. After 48 hrs, the suspended burgundy powders were precipitated as facilitated biotic Cu NP. In situ absorption showed the LSPR of facilitated biotic Cu NPs at ~590 nm in Figure 2-19(3). XRD of the facilitated biotic Cu NPs, as shown in Figure 2-18(3), exhibited elemental Cu and $Cu_2O$ peaks due to surface oxidation during post the harvesting procedure. NTA, as an initiator and a capping agent, facilitated growth of Cu NP in 2 days with ~50 nm ACS.

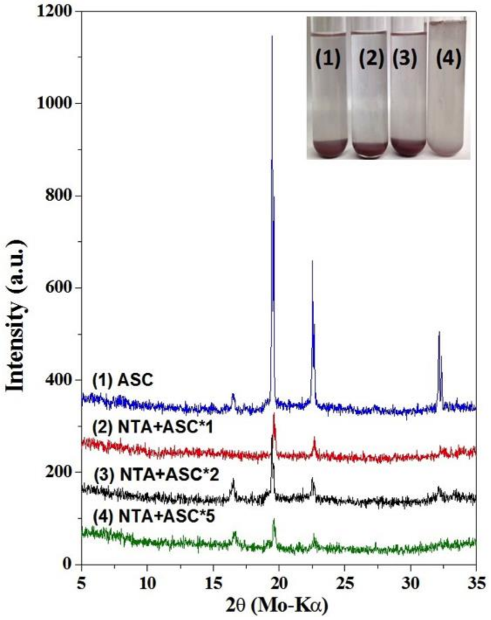

**Figure 2-20. XRD patterns of facilitated Cu NPs with addition of mixture of NTA and different ascorbic acid amounts**

Also, we found abiotic Cu NPs could be formed in the media at 65 °C. After addition of Cu precursor into the media, the blue color of the $CuCl_2$ solution gradually disappeared and became colorless during 1 day incubation. After 2 days incubation, red brownish coloration appeared in the solution and red powders were precipitated. The absorption spectra exhibited a featureless band between 400 and 800 nm in Figure 2-19(4), because of fast precipitated large abiotic Cu NPs. XRD of the abiotic Cu NPs exhibited a mixture of elemental Cu and $Cu_2O$ peaks in Figure 2-18(4). The ACS of abiotic Cu NPs was more than 100 nm. Both the smaller ACS-biotic and the larger abiotic Cu NP were centrifuged, washed, and re-dispersed in methanol. The re-dispersed facilitated biotic Cu NPs (with smaller ACS), as shown in inset of Figure 2-19(3), exhibited clear LSPR characteristics at 588 nm. For the re-dispersed abiotic Cu NP, the LSPR peak red-shifted to ~630 nm due to their larger particle size.

Based on the results with NTA, we developed a protocol to produce air-stable, ultrafine, biotic Cu NPs with ~30 nm size. Various chemical additives such as NTA as a chelating agent, ascorbic acid as an antioxidant, oleic acid as an anionic surfactant, and their combination were examined to prepare air-stable biotic Cu NPs with a limited ACS of less than 50 nm as well as a single-phase production. Figure 2-20(1) showed that addition of 5 mM ascorbic acid formed a mixture of Cu and $Cu_2O$ NPs with >100 nm. In spite of bigger ACS size, the oxidation took place post harvesting. However, as shown in Figure 2-20(2), the combination of additives (successive addition of 0.5mM ascorbic acid after NTA inoculation) developed air-stable elemental Cu NPs with ~53 nm of ACS. Increases of ascorbic acid amounts (×2, ×5) could not reduce ACS effectively and $Cu_2O$ was observed. NTA addition, as shown in Figure 2-21(1), did not prevent oxidation of Cu during washing and harvesting. Interestingly, successive addition of oleic acid after NTA inoculation, as shown in Figures 2-21(2)~(4), effectively stabilized elemental Cu NPs with a limited ACS. We found the possible optimized co-surfactant ratio (NTA+oleic acid×2) allowed ultra-fine elemental Cu NPs with ~28 nm of ACS. All properties of synthesized Cu NPs were summarized in Table 2.

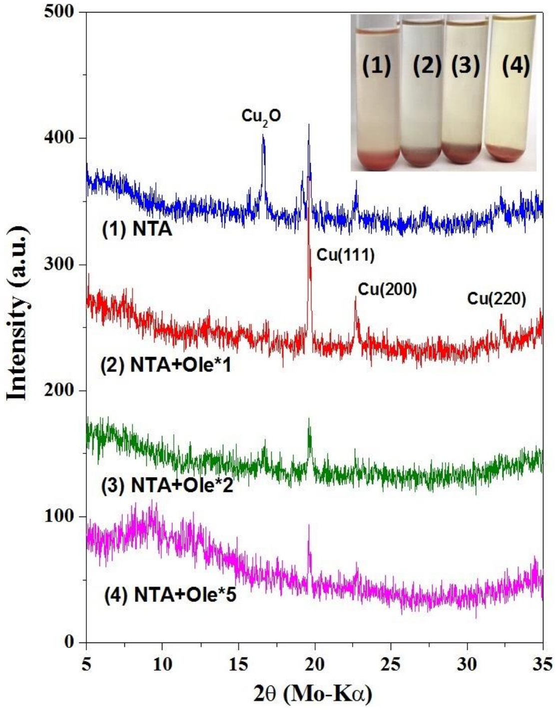

**Figure 2-21. XRD patterns of facilitated Cu NPs with addition of mixture of NTA and different oleic acid amounts**

**Table 2-1. Summary of various bio-synthesized Cu NPs**

| **Cu NPs** | **Incubation Time** | **Surfactant** | **XRD analysis** | **Cu LSPR peak** | **Average Crystal size** |
|---|---|---|---|---|---|
| **Abiotic** | 48hr | N/A | $Cu^0$ | 560 nm | >100 nm |
| **Biotic** | 72~120hr | N/A | $Cu^0$ | - | >100 nm |
| **Facilitated I** | 48+1hr | NTA*1 | $Cu^0 + Cu_2O$ | 590 nm | ~50nm |
| | 48+1hr | NTA*2 | $Cu^0 + Cu_2O$ | - | ~54nm |
| | 48+1hr | NTA*5 | Phase transition to $CuCl_2$ | - | N/A |
| **Facilitated II** | 48+1hr | Asc*1 | $Cu^0 + Cu_2O$ | - | >100 nm |
| | 48+1hr | NTA+Asc*1 | $Cu^0$ | - | ~53 nm |
| | 48+1hr | NTA+Asc*2 | $Cu^0 + Cu_2O$ | - | ~71 nm |
| | 48+1hr | NTA+Asc*5 | $Cu^0 + Cu_2O$ | - | ~44 nm |
| **Facilitated III** | 48+1hr | Ole | No reduction | - | N/A |
| | 48+1hr | NTA+Ole*1 | $Cu^0$ | - | ~70 nm |
| | 48+1hr | NTA+Ole*2 | $Cu^0$ | - | ~28 nm |
| | 48+1hr | NTA+Ole*5 | $Cu^0$ + Phase transition to $CuCl_2$ | - | ~56 nm |

### 2.2.8 Demonstrate upscaling to >10g batches from expanded $E_h$/pH platform

Significant scale-up was accomplished by demonstrating >10 g batches of a second new $E_h$/pH product (Ni-S or Co-S phase) resulting in 10.9 g of nickel-sulfide as a $Ni_3S_4$ form. Cobalt sulfide, close to the $CoS_2$ form, was also successfully produced but the yield was up to 9.9 g. The synthetic route of these sulfide materials and potential scale up >1 g were identified previously. Like previously demonstrated CuO and $SnO_2$ conversion from CuS and SnS through a controlled oxidation, these Ni- or Co-sulfide complex NPs were expected to produce oxide materials well-known to be attractive for high energy storage capacitors, carrier-selective interlayers in organic solar cells, catalytic activators, and thermistor applications. Nickel oxide is a wide bandgap (3.6–4.0 eV) transition metal oxide semiconductor. Depending on the composition, nickel oxides are good capacitors, but can also act as resistors and even as insulating materials. Pure nickel oxides are good high-temperature insulators. In combination with other metals, nickel oxide can act as a conductor. CoO has an energy bandgap of 2.2–2.8 eV whereas $Co_3O_4$ is 1.4–1.8 eV. Pure phase Ni- or Co-sulfides were planned to undergo controlled oxidation processes to produce their oxides.

We scaled up to 24 L to produce Ni- and Co- sulfide NPs >10 g. At first we examined the scale-up of Ni-sulfide with a 24-L reactor following the optimized protocol with 6 mM thiosulfate and 5 mM $Ni^{2+}$ to produce Ni-sulfide (Figure 2-22a). When we used a 1 psi Swagelok check valve, the same procedure and chemical concentrations from 24 L produced $Ni_3S_4$ NPs of 4.6 g (Figure 2-22b *i*) with ACS of ~5 nm. In contrast, the experiment in a closed system (closing check valve) after reaching 65 $^{o}$C of system and adding all ingredients except $Ni^{2+}$ produced 10.9 g of $Ni_3S_4$ NPs (Figure 2-22b *ii*) with ACS of ~8nm. One possible explanation is likely due to the solubility products of these sulfides. For example, CdS ($8\times10^{-28}$), CuS ($6\times10^{-37}$), SnS ($1\times10^{-26}$), and ZnS ($2\times10^{-25}$) have low solubility products in contrast to CoS ($4\times10^{-21}$) and NiS ($3\times10^{-19}$). Another explanation is stoichiometries of Ni- or Co-sulfide. Their phases were not metal:sulfide=1:1, therefore the NPs required greater than stoichiometric amounts of sulfide, such as $Ni_3S_4$=3:4 and $CoS_2$.=1:2. Therefore Ni- or Co-sulfide NPs likely require higher hydrogen sulfide concentration in the medium. $CoS_2$ phase products from a closed system (Figure 2-22b *iii*) had very poor crystallinity (Figure 2-22b *ii* vs. *iii*) and were loose after harvest and freeze drying. Therefore the final volume of 9.93 g of this product was greater than 10.9 g of $Ni_3S_4$.

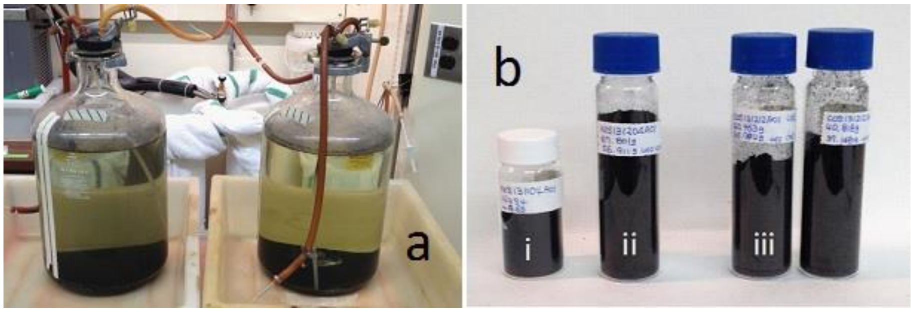

**Figure 2-22. a) Ni-S complex NP production using a dual parallel 24L reactor and b) freeze-dried final product of (*i*) $Ni_3S_4$ from the first reaction, (*ii*) $Ni_3S_4$ from the second reaction, and (*iii*) $CoS_2$ from a closed system**

Five surfactants such as ascorbic acid, L-cysteine, oleic acid, oleylamine and ammonium sulfur were intensively evaluated as capping agents for Cu NPs, because the air stability of colloidal NP dispersions is a key factor for post treatment such as separation, washing, ink preparation, and downstream applications such as NP film formation. We found that addition of NTA facilitated NP formation and reduced the size with colloidal stability in anoxic microbial medium. However, it did not sustain its stability during air exposure after separation and washing procedures. In order to improve the air stability against agglomeration and oxidation, several capping agents were added to the reaction media after NTA addition.

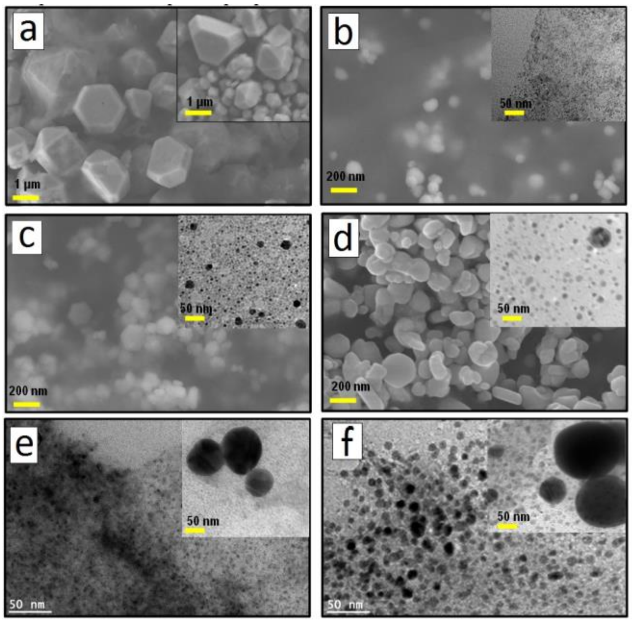

**Figure 2-23. TEM and SEM images of as-synthesized Cu nanocrystallites: a) Biotic Cu NPs (BCu); inset Abiotic Cu NPs (AbCu) and NTA facilitated Cu NPs including b) Cu+NTA (CuN), c) Cu + NTA + Cysteine (CuNC), d) Cu +NTA+ Ascorbic acid (CuNA), e) Cu + NTA + Oleic acid (CuNO), and f) Cu + NTA + Oleyamine (CuNM)**

**Table 2-2. Properties of various bio-synthesized Cu NPs**

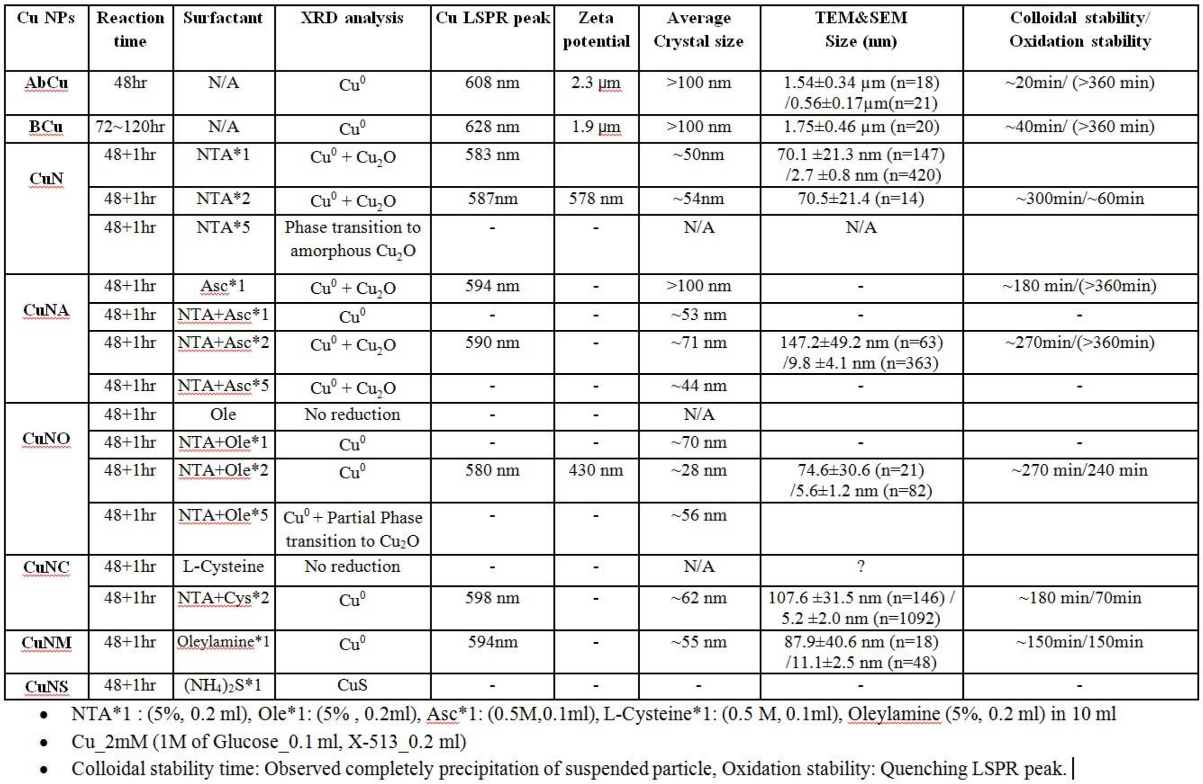

| Cu NPs | Reaction time | Surfactant | XRD analysis | Cu LSPR peak | Zeta potential | Average Crystal size | TEM&SEM Size (nm) | Colloidal stability/ Oxidation stability |
|---|---|---|---|---|---|---|---|---|
| AbCu | 48hr | N/A | $Cu^0$ | 608 nm | 2.3 µm | >100 nm | 1.54±0.34 µm (n=18)<br>/0.56±0.17µm(n=21) | ~20min/ (>360 min) |
| BCu | 72~120hr | N/A | $Cu^0$ | 628 nm | 1.9 µm | >100 nm | 1.75±0.46 µm (n=20) | ~40min/ (>360 min) |
| CuN | 48+1hr | NTA*1 | $Cu^0 + Cu_2O$ | 583 nm |  | ~50nm | 70.1 ±21.3 nm (n=147)<br>/2.7 ±0.8 nm (n=420) |  |
|  | 48+1hr | NTA*2 | $Cu^0 + Cu_2O$ | 587nm | 578 nm | ~54nm | 70.5±21.4 (n=14) | ~300min/~60min |
|  | 48+1hr | NTA*5 | Phase transition to amorphous $Cu_2O$ | - | - | N/A | N/A |  |
| CuNA | 48+1hr | Asc*1 | $Cu^0 + Cu_2O$ | 594 nm | - | >100 nm | - | ~180 min/(>360min) |
|  | 48+1hr | NTA+Asc*1 | $Cu^0$ | - | - | ~53 nm | - | - |
|  | 48+1hr | NTA+Asc*2 | $Cu^0 + Cu_2O$ | 590 nm | - | ~71 nm | 147.2±49.2 nm (n=63)<br>/9.8 ±4.1 nm (n=363) | ~270min/(>360min) |
|  | 48+1hr | NTA+Asc*5 | $Cu^0 + Cu_2O$ | - | - | ~44 nm | - | - |
| CuNO | 48+1hr | Ole | No reduction | - | - | N/A |  |  |
|  | 48+1hr | NTA+Ole*1 | $Cu^0$ | - | - | ~70 nm | - | - |
|  | 48+1hr | NTA+Ole*2 | $Cu^0$ | 580 nm | 430 nm | ~28 nm | 74.6±30.6 (n=21)<br>/5.6±1.2 nm (n=82) | ~270 min/240 min |
|  | 48+1hr | NTA+Ole*5 | $Cu^0$ + Partial Phase transition to $Cu_2O$ | - | - | ~56 nm |  |  |
| CuNC | 48+1hr | L-Cysteine | No reduction | - | - | N/A | ? |  |
|  | 48+1hr | NTA+Cys*2 | $Cu^0$ | 598 nm | - | ~62 nm | 107.6 ±31.5 nm (n=146) /<br>5.2 ±2.0 nm (n=1092) | ~180 min/70min |
| CuNM | 48+1hr | Oleylamine*1 | $Cu^0$ | 594nm | - | ~55 nm | 87.9±40.6 nm (n=18)<br>/11.1±2.5 nm (n=48) | ~150min/150min |
| CuNS | 48+1hr | $(NH_4)_2S$*1 | CuS | - | - | - | - | - |

- NTA*1 : (5%, 0.2 ml), Ole*1: (5% , 0.2ml), Asc*1: (0.5M,0.1ml), L-Cysteine*1: (0.5 M, 0.1ml), Oleylamine (5%, 0.2 ml) in 10 ml
- Cu_2mM (1M of Glucose_0.1 ml, X-513_0.2 ml)
- Colloidal stability time: Observed completely precipitation of suspended particle, Oxidation stability: Quenching LSPR peak.

The formation of Cu nano-crystallites with various capping agents was confirmed by TEM and SEM analysis. Figure 2-23 and each inset shows that micron and nanometer-size Cu crystallites were formed by chemical reduction as shown in the inset of Figure 2-23a, Abiotic Cu NP (AbCu), anaerobic microbial mediated process a) biotic Cu NP (BCu) and capping agent coated biotic Cu NPs including b) NTA (CuN), c) NTA+L-Cysteine (CuNC), d) NTA+Ascrobic acid (CuNA), e) NTA+Oleic acid (CuNO), and f) NTA+Oleyamine (CuNM). The addition of capping agent formed bimodal-sized Cu NPs. Specific properties of Cu NPs including size, composition and optical properties are summarized in Table 2.2.

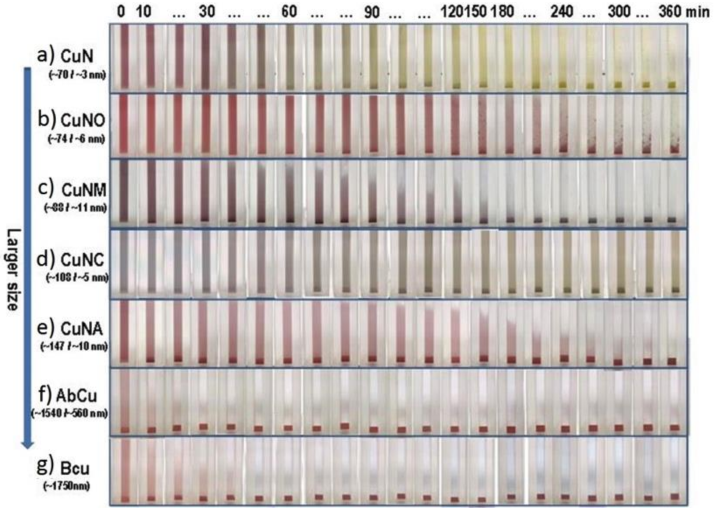

**Figure 2-24. Time course photographs show color and precipitation changes of colloidal Cu nanocrystals during air exposure.**

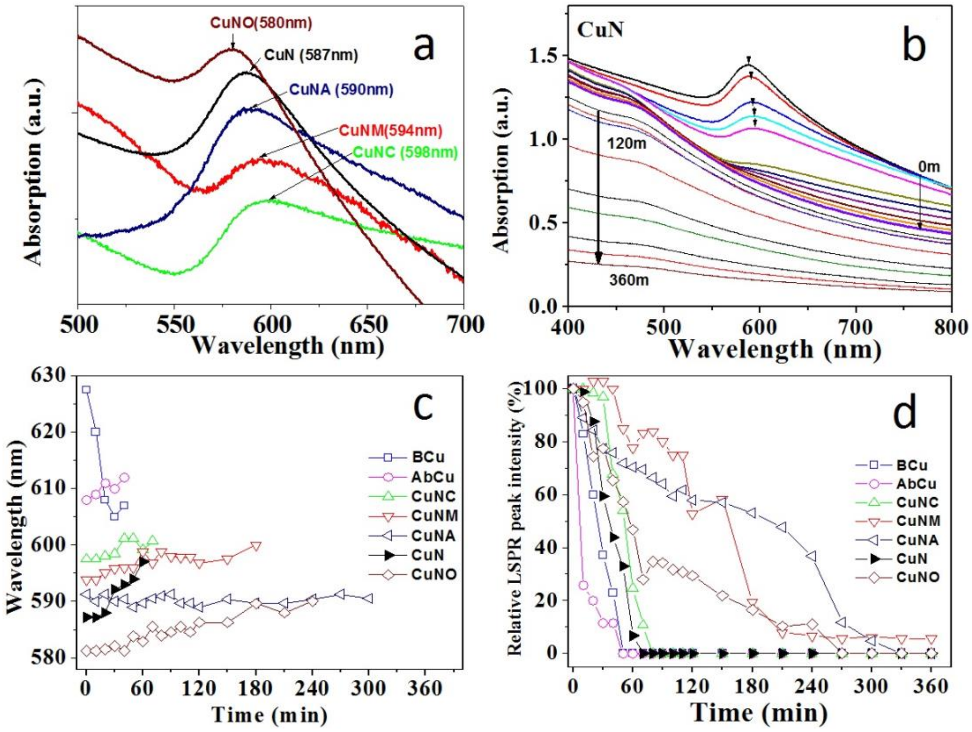

**Figure 2-25. a) Optical absorbance spectra of various colloidal Cu NPs at 0 min, b) Corresponding time coursed spectra change of CuN NP under oxidization, c) Changes in peak position of corresponding Cu NPs during oxidation process, and d) Relative LSPR peak intensity (%) changes during oxidation process.**

Figure 2-24 shows time course photographs of color and colloidal changes of various Cu NPs in aqueous solution during air exposure. These colloidal Cu NPs were prepared by washing four times using centrifugation, collecting supernatant, and re-dispersing in aqueous solution in an anoxic globe box. These Cu NPs in cuvettes were sealed from air until spectral measurements in an open-air environment. Photographs and UV-Vis absorption spectra were taken every 10 min for 6 hrs. Figure 2-25 exhibits the corresponding absorption spectra and localized surface plasmon resonance (LSPR) features.

The LSPR features of the suspended Cu NPs, peak position and peak intensity, were significantly affected by the presence of copper oxide layer and agglomeration of particles. Specifically, the oxidation of reddish colloidal Cu NPs (due to a localized surface plasmon feature at 560–610 nm) changes to greenish colloidal amorphous and/or crystallite $Cu_2O$ NP (due to an excitonic feature at 720–750 nm corresponding to the band gap of the $Cu_2O$ nanocrystals). Also, an increase of aggregate size of colloidal Cu NPs led to red-shifting of the Cu LSPR and finally quenching the plasmonic feature of the nanometer size regime via agglomeration into bulk Cu.

The red colloidal CuN NPs at 0 min (Figure 2-24a), changed to dark red around 30 min and gradually turned to green and whitish green at 180 min. However, they appeared well suspended for 90 min and gradually precipitated by 300 min during air exposure, attributed to oxidation of CuN NP. At 360 min, all green particles were precipitated on the bottom. XRD of the green slurry shows no crystallite peaks due to phase change to amorphous solid (data not shown). The corresponding time course UV-Vis absorption spectra of CuN (Figure 2-25a and b) show that the LSPR peak at 587 nm at 0 min red-shifted to 598 nm by 60 min. The peak intensity also dramatically decreased within 50 min and finally disappeared after 60 min. However, the overall absorption band was stable for 120 min. After 180 min, the overall absorption band clearly decreased. It indicates that full oxidation from Cu to amorphous $Cu_2O$ proceeded within 60 min, but colloidal amorphous $Cu_2O$ NPs were suspended up to 180 min and then precipitated via NP agglomeration.

Depending on coated capping agents (Figure 2-25a), colloidal Cu NPs exhibited tunable LSPR peaks from 580 nm to ~600 nm due to different size and refractive index induced by different chemi-adsorped organic layers. Specifically, addition of ascorbic acid (CuNA) exhibited the longest stability against oxidation and agglomeration. Figure 2-25c shows CuNA sustained the LSPR feature for 300 min within ~2 nm of red-shifting, which is 15 times longer than CuN (>5 nm shifting after 20 min). CuNA had a bimodal particle distribution. For the initial 10 min, the larger particles (~147 nm) appeared to be quickly agglomerated and precipitated. However, small particles (~10 nm) were well dispersed and slowly precipitated over 300 min. Also, the densely packed layer of long carbon chain oleic acid and oleylamine molecules effectively enhanced suspension of all colloidal NPs. For CuNO, noticeable precipitation of partial NPs was recognized after 120 min. LSPR of CuNO and CuMN red-shifted within ~10 nm and gradually quenched for 150 min and 240 min, respectively. For CuNC, visible precipitation was noticed at 90 min with color change. A reduced red-shifting LSPR feature within ~5 nm suggested that oxidation stability appeared to be improved three times longer compared with CuN, whereas visible and LSPR colloidal stability (relative peak intensity) were similar to CuN. Larger micron-size particles of AbCu and BCu (Figure 2-24f and g) appeared to be easily precipitated within 10 min. Also, the LSPR peak position and relative LSPR peak intensity (Figure 2-24c and d) are quickly quenched in one hour due to fast precipitation. Characterization of ammonium sulfur, inorganic surfactant, was excluded because of formation of copper sulfide NPs.

## 2.3. UPSCALE NANOFERMENTATION TO INDUSTRIAL PILOT SCALE

This task designed, fabricate and demonstrate an approximately 800 liter pilot plant, representing a 20X increase in production capability. The first year of effort focused on facility design, safety, training, and initiating fabrication of the industrial pilot scale fermentation and product recovery system. The second year effort focused on installation and operations of the 100L pilot plant with nanoparticle recovery. The third year effort was focused on installation and operation of a pilot-scale 900-L reactor.

### 2.3.1 Identify space, safety, training and waste issues with ORNL Subject Matter Experts (SMEs)

To set up operating facilities, we identified space, safety, training and waste issues with ORNL Subject Matter Experts (SMEs). Laboratory bench scale safety summaries have been updated and a new Research Safety Summary (RSS) was initiated for the Task 3 upscaling. Training was up-to-date and training modules were identified for new researchers. Meetings regarding upscaling safety included ORNL and external SMEs. The Room 8 laboratory in building 1504 was selected for the pilot facility. The lab needed to be share with other projects, ensuring qualified personnel will be in the space on a daily basis – yet lightly utilized. Some equipment such as the walk-in fume hood was selected for ordering. An advantage of the chosen laboratory was its loading dock height providing ease for fermentor and equipment installation. The lab was on an exterior wall with a >3 foot elevation drop to the ground surface. This drop in elevation provides space for waste storage or spill containment external to the building. In addition there was a 3×10 ft area immediately adjacent to the planned fume hood ideal for storage of wastes within the laboratory. The lab also contained an underutilized cold room for storage of water, media, and precursor solutions, as well as a gassing station and stainless steel (SS) distribution lines. Importantly, the lab has ~200 Amps at 220 V of underutilized power that is also on the emergency generator. Overall the lab is adequate space in along an external wall next to a loading dock and with a cold room and computer links as well as a pre-wired (6 line – four of which are not used) warning notification system to a PI's cell phone should there be a power or equipment failure.

### 2.3.2 Submit Research Safety Summary (RSS) draft for SME and management reviews

In parallel to the pilot plant engineering, a draft RSS for subject matter experts and management was submitted for administrative review. The laboratory RSS was approved and is fully operational. The scale-up RSS was drafted and reviewed by ORNL SMEs and management. Electrical upgrades were made to support the pilot plant and new HEPA walk-in fume hood. The 100-L fermentor was custom-built for delivery around late July or early August in 2012. Final design modifications were made on the 800-L fermentor plans, and it was ordered for delivery in late 2012.

### 2.3.3 Submit draft engineering designs for operations and management review

The drafts of engineering design of pilot-plant reactors for operations were submitted and went to management review. The draft design of the 800 L pilot plant was complete, operations and safety procedures were reviewed by management, and the pilot plant facility was initiating the development phase with equipment being delivered and installations proceeding. Pictured in Figure 3-1 is the 100-L fermentor that arrived at ORNL in late September 2012 and was planned to undergo mock trials (without nanoparticles) during fall 2012. Importantly, as we gained more experience with the bench scale operations we see evidence that the estimated cost of NanoFermentation may be further declining based on the successful production of about 2 g/L/month using the 12–20L laboratory vessels.

**Figure 3-1. 100-L fermentor**

### 2.3.4 Complete final engineering design and safety summaries

Submitted draft for engineering design for operations and management review were completed. The safety summary document for the development of the pilot plant is in the hands of management and undergoing final management review. Extensive meetings were held numerous times with subject matter experts and all felt we were more extensive in safety than expected and far better than required. The electrical engineering design was complete with the final new circuits being added with the proper voltages, phases of power and receptacles for each of the associated items. They were estimated to be complete by January in 2013; the final three 208–220 volt electrical lines and one of which was 3-phase 30 Amp line to power the two 208 V × 9 Amp heating-circulating units to heat the fermentor vessels. A second 220 V × 20 Amp line will power the centrifuge in the fume hood. The third will power the autoclave. Two more 110 V lines are installed, including one that will hang from the ceiling. The hanging 110 V line will be used to power the fermentor stirring mechanisms eliminating the use of extension cords overhead from the fume hood power supply.

The plumbing design was complete and the floor covering was ordered. The layout design was complete and once the electrical panels are in place and the floor covering laid equipment will be placed in proper position. Consequently, the draft design of the 800-L pilot plant was complete as well as operations and safety procedures were being reviewed by management, and the pilot plant facility was initiating the development phase with equipment being delivered and installations proceeding. The 100L fermentor was ready for placement.

### 2.3.5 Initiate installation of 100L pilot plant and product recovery equipment

The installation of various pilot plant components was initiated. All electrical and gas lines were in place and the installation was following the designed layout. The 100-L fermentor was in position, as shown in Figures 3-2 and 3-3. Figure 3-2 shows the overall view of the pilot plant area. The sealed liner pad is 45 mm reinforced polypropylene industrial pond liner that is sealed with specialty tape. In case of a large leak the fluids will be drained from the lab and out of the building into a holding tank on a concrete pad. The raised lip of the containment area was made from 4in × 4in pressure treated wood and the liner was taped to the floor, making it readily moveable if required. Above the fume hood are the HEPA filters. The recently installed differential air pressure gauge can indicate any clogging or change in the HEPA filtering efficiency over time. Also note the snorkel from the fume hood, which can be placed above an operating fermentor so as to catch any release of NP or hydrogen sulfide gas if that should ever occur. The stir motor and paddle were tested and installed on the 100-L fermentor later. To the left of the laboratory is a loading dock. On the loading dock is our 85 L autoclave with its dedicated 220 V line. Sterilized media will transfer from a vessel residing in the autoclave to the fermenters via a low pressure nitrogen gas flushing, thereby avoiding any moving parts or pumps. The rack on the left side of the hood will house the pH controller, pH adjusting pumps, dosing solutions for the fermenters and other fermentation supplies. Under the bottom shelf is a cooling unit that will be described later for use in cooling product fluids immediately prior to centrifugation. To the left of the hood is the future location of the heating unit for the 800-L fermenter, which itself will reside in the large open area in front of the hood. To the right of the hood is our cold room where distilled water and solutions will be stored at 4 °C prior to use. In the lower right of the photo one can see our tool table, complete with a 5 inch vise, tools, and a solid working surface. To the right is a total of 14 ft of linear bench space for process working, assembly and disassembly of fermentation accessories. Behind the cold room is a chest freezer for sample storage. The room is equipped with an extra air handler providing dehumidified and conditioned air to offset the air removed by the room vent fan and by the hood.

**Figure 3-2. Pilot facility construction is in progress. The spill pad is in place as are the 100-L fermentor and processing equipment. Note that all processing will occur in the HEPA filtered hood (filters on top of hood) with a snorkel placed over the fermentor in case of leaks**

Figure 3-3 shows a closer-in view of the pilot equipment. The 100-L fermentor is set on its plexiglass platform to protect the spill liner from wear. The fermentor has two external water jackets for heating to the required 65 °C; the primary water jacket is exterior of the vessel along the vertical side of the fermentor and a separate water jacket is exterior to the collecting cone at the bottom of the vessel. One can note an indentation of the fermenter wall at the top of the neck. That indentation is essentially the fermentor wall and the bulging below that point represents the outer dimensions of the exterior water jacket. In addition there is a ½ inch looped SS line inside of the vessel that can be used either for supplemental heating or cooling the interior of the fermenter. All heating and cooling lines are temperature stable reinforced flexible lines equipped with Swagelok quick-release fittings.

**Figure 3-3. The 100-L fermentor is on right next to its heating unit. The centrifuge is inside the HEPA filtered fume hood. Next to the centrifuge is a 35gal SS drum for centrifuged media. White pail on floor is a cooling unit to cool the fermentation broth with NP prior to centrifugation**

To the left of the fermenter is the heating unit that will recycle ~65 °C water to and from the water jackets in a closed-loop such that the internal temperature of the 100-L fermentation volume can be maintained at 65 °C. The heated water will enter the bottom of each jacket and exit the top, thereby avoiding development of air pockets, prior to returning to the heating unit. NP-containing fluids exiting the bottom of the fermentor pass through valves attached to a flexible line followed by a stainless steel (SS) line going to a sealed 5-gallon pail. This is a cooling system designed to cool the NP fluids close to room temperature prior to centrifugation. The NP fluids will enter the pail and pass through 50 ft of coiled SS tubing. The pail is filled with water that then is cooled by a 50 ft coil of copper tubing that is chilled such that the NP-containing fluids exiting the pail and headed to the centrifuge will be near 20 °C an ideal temperature for the centrifuge (centrifuge specifications suggest temperatures of input fluids to be less than 40 °C). The cooling unit for the cooling coil is located under the storage rack on the left side of the hood (Figure 3-2 above). Immediately in front of the centrifuge will be a peristaltic pump that will draw NP-fluids from the fermentor, through the cooling coil and then pump them into the centrifuge at a defined rate. We purchased two peristaltic pumps suited for this most important task. NPs will be centrifuged from the medium with the NPs held in the centrifuge rotor. After approximately 2 kg of NP recovery the centrifuge will be stopped and the rotor emptied with the NPs stored in polyethylene containers. Fluids exiting the centrifuge will enter the poly-lined SS drum to the left of the centrifuge. This drum will have Swagelok fittings for fluid input (from the centrifuge) as well as a gas vent to a gas trap. The gas trap was installed but not visible in the photos. The system is integrating nicely and no major setbacks have occurred. Based on our experiences setting the 100-L fermentor we made minor modifications in the holes in the lid of the planned 800-L fermentation vessel.

### 2.3.6 Complete installation of 100-L pilot plant

A considerable effort was focused on getting sufficient flow through the HEPA-filtered fume hood. We had an unforeseen difficulty with backup power in that whenever the cold room compressor kicked in the flow through the hood was insufficient. It turned out that the motor driving the suction of air through the HEPA filter was overly sensitive to power draws from the emergency backup line when the cold room compressor activated. No other fume hood in the 1504 building was adversely affected. The outcome has been the rewiring of the HEPA-filter exhaust fan motor from emergency power to regular power. This rewiring has brought the hood into compliance but still not up to ideal specifications. Further modifications are being considered. The only downside of this rewiring is that whenever normal power goes out in the building the fume hood will cease operation and any harvesting in progress would also have to cease. This will not be hindrance since all fermentation and auxiliary processing would also cease during power failures.

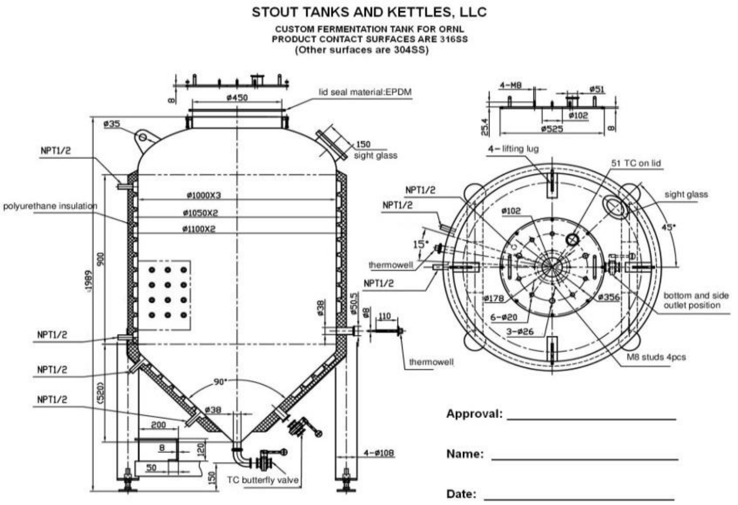

**Figure 3-4. Design of the 800-L fermentation vessel for delivery in fall 2013**

The final design and ordering of the 800-L vessel (Figure 3-4) was completed. The design was completed, specifications were completed, quotes received, and procurement finalized. Fabrication initiated in mid-June with its delivery and installation planned for fall of 2013.

Safety documents and work-aids were approved and posted. As this was occurring testing of the various components has commenced. The water heater and coolers worked well and did in fact heat the 100-L fermentation vessel to optimal temperature in less than half of a day and hold the temperature for week intervals. The sulfide monitor was also installed and is in working order. The actual calibration and continual operation commenced in July. Based on our experiences setting the 100-L fermenter (Figure 3-5), we made minor modifications in the holes in the lid of the planned 800-L fermentation vessel. Although this large reactor was designed to contain 800 L of medium, we later found that the practical working volume of this reactor was 900 L. Therefore this nominally 800-L reactor is referred to as a 900-L reactor in this report.

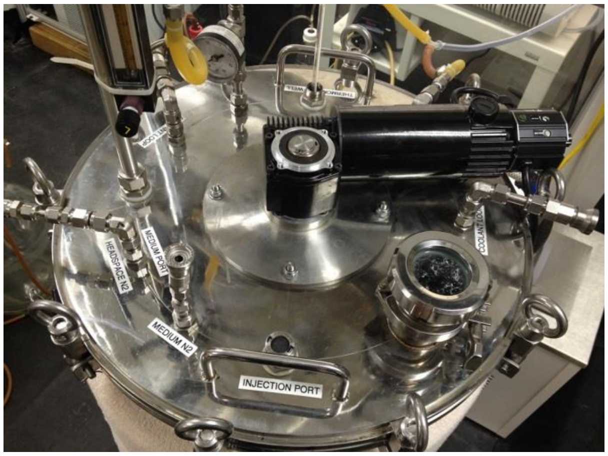

**Figure 3-5. Modified lid equipped with additional components and ports**

### 2.3.7 Successful operation of 100 L pilot plant with nanoparticle recovery

Based on the last minor room modifications, a considerable effort continued to be focused on getting sufficient flow through the HEPA-filtered fume hood. After we rewired the HEPA filtered walk in fume hood the flow was legally sufficient but marginal. It was obvious that with several months of operation, after the filter started to plug with dust, that the flow would be problematic. Engineers endeavored to increase the 'draw' through the HEPA filter by increasing the fan speed, blade angles, or upsizing the fan motor.

Figure 3-6 shows the operation of the centrifuge concentrating a pellet of previously made magnetite. Bottles containing 100 ml of 10 % magnetite were centrifuged at 4000 rpm for 30 min resulting in a hard pellet at the bottom of each container. The centrifuge worked well and no problems were noted. Other aspects of the pilot plant did pose challenges. Transporting NPs from the fermentation vessel to the centrifuge requires a peristaltic pump. The most gas impermeable tubing for peristaltic pumps is of Viton, but Viton is soft and broke within 30 L of pumped fluids. For most applications Viton is ideal and the tubing is moved a few inches so that it does fail after long usage. However for our applications we need the tubing to last an hour each operating mode prior to the emptying of the continuous centrifuge rotor. Consequently we have opted for longer lasting Neoprene-Food-Grade tubing.

**Figure 3-6. Operation of the centrifuge recovering and concentrating NPs inside of the HEPA-filtered walk-in fume hood**

Neoprene is more gas permeable so we are using thicker walled tubing that successfully operates for an entire 100L run without excessive wear. Our operational procedures will call for moving the tubing a few inches upstream of the peristaltic pump rollers after each centrifuge run (~30–50 L) to ensure safety margins for the tubing life.

A major pilot plant design concern was transporting the sterilized media from the autoclave to the fermentor. We successfully used a sterile nitrogen-gas drive system to push the hot fluids to the 100-L fermentor without any moving parts or human handling. There were several design alternatives for this transfer but avoiding pumps, moving parts or man-handling was ideal and accomplished. We applied 7 psi of nitrogen gas pressure to a retrofitted quick connect hose to the autoclave pressure chamber. [The autoclave model we procured provided us 2 × 3/8 inch NPT threaded ports into to the pressure chamber so we made no modifications to the pressure chamber.] The nitrogen gas was filtered through a 0.2 μm filter immediately in front of the autoclave so that the gas was sterile. Nitrogen gas then pressurized the entire autoclave pushing the media contained in our SS vessel (actually a small SS drum) out via a dip tube and 3 m over to the fermentor, all as a closed system. The nitrogen-gas drive worked beautifully as a closed system with no moving parts, no pumps and requiring no lifting of handling of hot fluids. We had hoped that <5 psi of pressure would have been sufficient to pump the fluids but it took more pressure to close the autoclave vent valve. Accordingly <5 psi nitrogen could be used for our fermentation vessel and as a driver for sealed liquids transfer from bottles to the fermentor. As a result we had to add yet another low pressure regulator at the fermentor reducing the 7 psi gas to 4 psi for use at and around the fermentor.

When we ordered our 15 gal SS drum as a medium autoclaving vessel we ordered it with a butyl rubber gasket in the lid seal so that it would tolerate repeated autoclaving. Unfortunately, the manufacturers used temperature sensitive silicone-type glue. Several hours were spent cleaning melted gelled glue from the SS drum. Turns out we do not need a gasket liner at all. Such are the unexpected nuances of building prototype pilot plants.

### 2.3.8 Complete installation of 800-L pilot plant

We focused on installation of the 800-L pilot plant and we implemented minor modifications with the feedback from running the 100-L reactor. Lessons learned from 100 L dry run were discussed. A considerable effort continued to be focused on ensuring safe operations before NanoFermentation startup. Activities in the pilot plant including a dry run using only deionized water revealed several issues related to sensors that would detect leakage of hydrogen sulfide, laminar flow of the walk-in fume hood, and operation of the continuous-flow centrifuge. Hydrogen sulfide sensors produced false alarms when no $H_2S$ was present; therefore we ordered new sensor components for replacement. The HEPA-filtered walk in fume hood sometimes registers low flow when a refrigeration compressor in the room cycles on despite isolated circuits; ORNL electricians investigated necessary repairs. Finally, a sensor in the centrifuge had malfunctioned; a repair request was issued.

**Figure 3-7. Installed 900-L reactor with completed plumbing to water jacket awaiting commissioning (left) and 100-L reactor (right) in dry operation using deionized water**

A major pilot plant design concern was transporting the sterilized media from the autoclave to the fermentor. We had demonstrated a sterile nitrogen-gas drive system to push the warm fluids to the fermentor. Subsequently, we began to simplify this process due to a decrease in flow rate after a couple of liters had been transferred from the specially designed autoclave. The improved processes aimed to avoid pumps, moving parts or strenuous lifting and pushing activities. A couple of change were made and successfully tested in a 1 L bench scale.

For the 100-L pilot plant, the original design was to mix 75 L of deionized, deoxygenated and autoclaved water with 25 L of sterilized (121 $^{o}$C/17 psi, 2 hour) concentrated medium. As an alternative, we placed 1-L nonsterilized and oxic medium in a 2-L vessel and pasteurized (65 $^{o}$C, 2 days) with nitrogen gas, purging to make the medium anoxic (Figure 3-8a). This medium was dosed with sterile 10 mM glucose, 6 mM thiosulfate, and 20 mL of a mid-log growth phase X513 cell stock solution and was incubated at 65 $^{o}$C for 2 days (Figure 3-8b). Then 5 mM of Zn$^{2+}$ was dosed to produce ZnS (Figure 3-8c). As observed previously, dosed Zn$^{2+}$ incorporated with developed hydrogen sulfide ions to produce white ZnS precipitate immediately. After 24 hours, harvested and washed samples exhibited a similar yield to that from the original protocol.

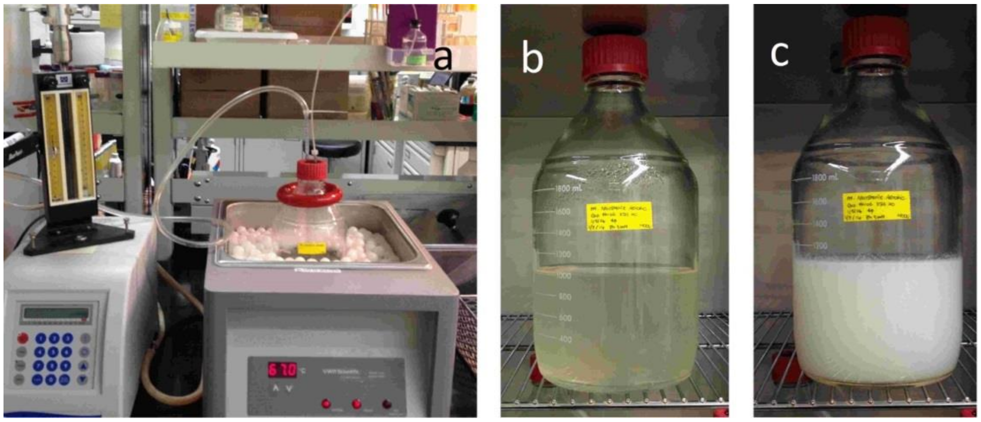

**Figure 3-8. Pasteurization approach applicable to 100-L and 800-L reactions. a) Degassing process, b) Enrichment using pasteurized medium prepared from oxic, nonsterile medium, c) NanoFermented ZnS samples**

**Table 3-1. Comparison between the original sterilization plan and a new pasteurization process show the new process to be more efficient for commercialization**

| | Original design | Tested new design |
|---|---|---|
| Medium preparation | • Autoclave (121 °C/17 psi, 2 hr) for sterilization/deoxygenation | • Pasteurization (65 °C, 3 days)<br>• Sparging for deoxygenation |
| Medium transfer | • Pushing 7 psi nitrogen drive | • Using 7 psi nitrogen drive /filter |
| Advantages | • Short preparation time | • Short connection lines<br>• Compact and easy process<br>• No handling hot fluids |

### 2.3.9 Complete shakedown of 800 L pilot plant

We began operating the 100-L reactor to produce >50 g ZnS after resolving several problems including replacing $H_2S$ detector, repairing the continuous flow centrifuge, and controlling air flow in a walk-in chemical fume hood. 3 of 4 planned consecutive batches of ZnS NanoFermentation were completed in the 100-L vessel during the first quarter of operation. Results from operating the 100-L reactor would inform operations using the 800-L reactor. A considerable effort continued to be focused on ensuring safe operations. We continuously improved our safety and simplified work flow including:

- Updating work aids and protocols to prevent spills or accidents during 100-L batches (Figure 3-9a)
- Implementing sedimentation tanks for cooling and NP precipitation to avoid using a cooling unit and prevent tubing failure that is common at high temperatures (Figure 3-9b)
- Changing the waste stream collection by direct accumulation in the walk-in-fume hood and reducing wastewater by recycling ~65 L of used medium (Figure 3-9c)
- Controlling pH using base titration instead of the expensive organic buffer that was used in small-scale experiment up to 24 L.

**Figure 3-9. Operational work-aid, practice, and outcome through actual runs of 100-L reactor**

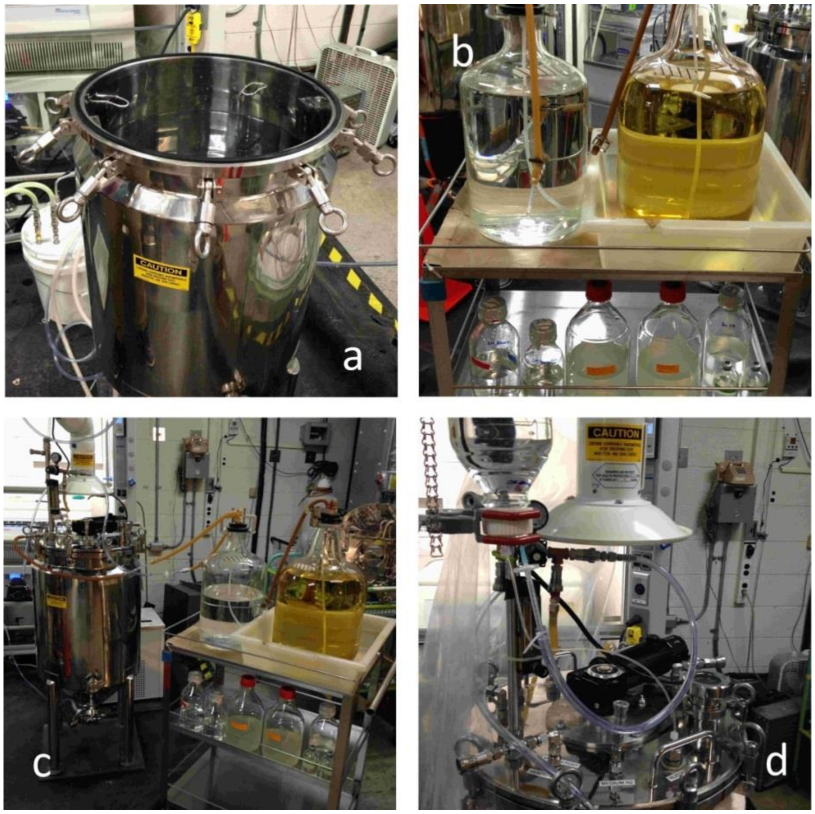

**Figure 3-10. Operational work-aid, practice, and outcome through actual runs of 100-L reactor**

The first 100-L batch was started by mixing 75 L of in-house distilled water with 20 L of concentrated medium in the vessel, followed by pasteurization and deoxygenation at 65 °C for 3 days (Figure 3-10a). The pasteurized medium was then dosed with nutrient, thiosulfate, mid-logarithmic growth phase X513 cells and incubated for 2 days and then dosed with $ZnCl_2$. For the second run, we compensated for lost volume by adding deionized water and 60% ingredient equivalent medium (sterilized 121 °C/17 psi, 2 hour) with other injection solutions including sterile 10 mM glucose, 6 mM thiosulfate, and 2 L of a mid-log growth phase X513 cell stock solution. This second batch was incubated at 65 °C for 2 days (Figure 3-10b). Solutions in carboys were transferred through the headspace purging line and (Figure 3-10c), and solutions in bottles were added using the injection port with double-ended needles (Figure 3-10d). Cells were incubated with $Zn^{2+}$ for 24 hours; afterwards the reactor was shut down and cooled (Figure 3-11). Precipitates were harvested using a peristaltic pump at 110 mL/min to transfer the slurry to a sedimentation tank without disturbing precipitates at the bottom of the vessel. Through the reactor window, we continuously observed inside the reactor and confirmed the process such as recycled medium with pH titration, inoculation and enrichment and ZnS formation.

The first ZnS batch from the 100-L pilot-plant reactor used a higher $ZnCl_2$ dose (6 mM) compared to small batches (5 mM), resulting in an increased yield of 62 g of ~5 nm ZnS NPs. This result indicates that increasing the $ZnCl_2$ dose and scaling up production to 100 L did not affect the ZnS precipitates (Figure 3-12). The second batch with an increased 7mM $ZnCl_2$ dose resulted in a reduced 55 g ZnS yield. Therefore we increased the incubation time during the 3rd batch and planned to add 100% ingredient-equivalent condensed solution at the 4th batch to obtain >70 g ZnS. This media recycling method was likely to reach the enhanced manufacturing goal of ~500g/month/100L pilot plant.

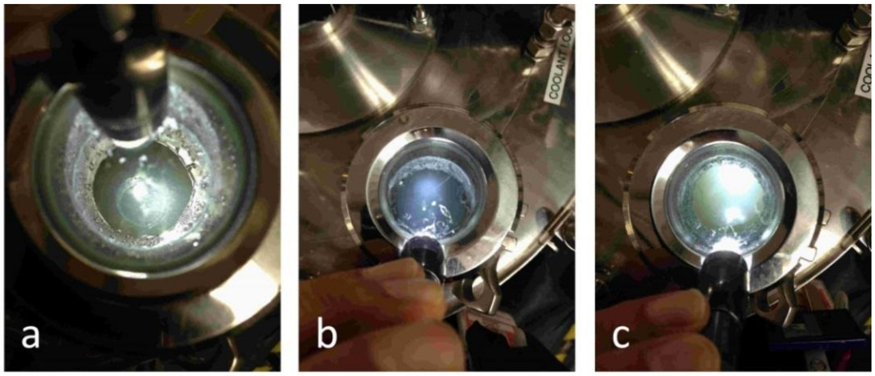

**Figure 3-11. Visualizing NP formation through the reactor window. a) Before inoculation of X-513 just with pH titration to used medium, b) 2-day incubation after inoculation of nutrition and bacteria showing typical blue tint, c) After dosing $ZnCl_2$ into the 100-L pilot plant exhibiting dense white color of ZnS suspension**

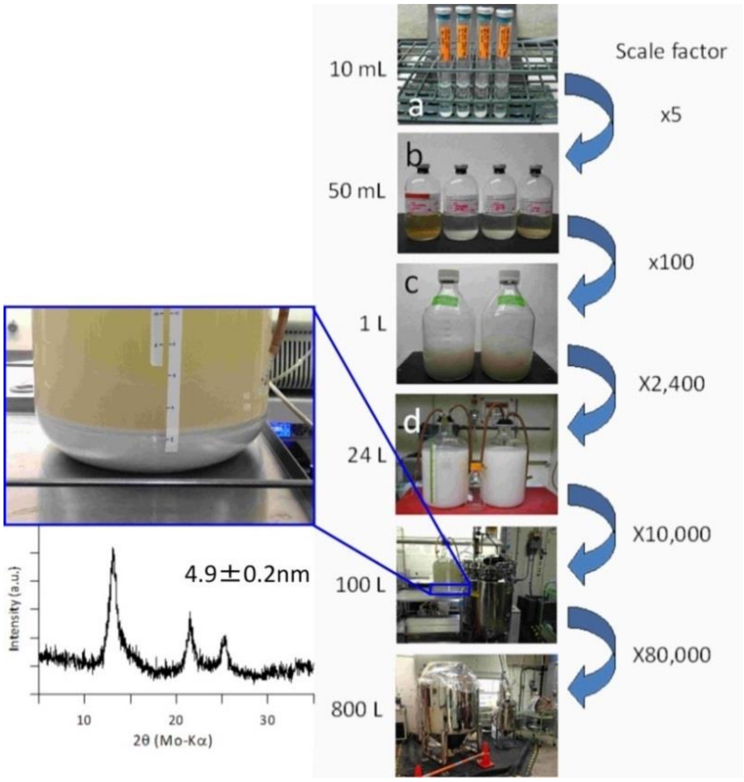

**Figure 3-12. A batch process in the 100-L reactor with a 10,000 scale factor resulted in more than 2 L of precipitated material and ~5 nm average crystallite size, similar to ZnS NPs from small batches**

To safely place the 800-L pilot plant and remove the vessel lid, connection hardware and stirring motor, a pulley system was developed for installation on the pilot plant ceiling trusses (Figure 3-13a). Installation was completed shortly after the end of March of 2014, enabling vessel operations. Safety protocols for a 2-person lift process using this pulley system were created and documented. Activities in the pilot plant including a dry run using only deionized water in the 800-L pilot plant scale reactor, checking the leakage of hydrogen sulfide or solution, testing the laminar flow of the walk-in fume hood, and evaluating linked operation of the continuous-flow centrifuge right after the complete installation of the whole rigging equipment such as pulley system and spacious ceiling. A simplified shakedown for checking leakage during water circulation from the water bath (Figure 3-13b) was executed.

**Figure 3-13. a) 800-L reactor protected by plastic sheeting during overhead construction. Enhanced waste streaming was seen by series of poly-lined drum canisters. One canister directly accumulates nanoparticle waste from the sedimentation tanks in the walk-in-fume hood. 30-gallon drum canisters can be removed using a handtruck to roll the bleach-treated drum over the metal bridge spanning the containment berm in the pilot plant and b) Simplified shakedown for checking leakage during hot water circulation from water bath**

### 2.3.10 Demonstrate reproducibility of pilot plant upscaling with >300 g /month

The 100-L reactor was operated to produce >50 g ZnS successfully after resolving several problems related to the infrastructure, and we obtained 2 out of 4 consecutive batches. Consecutive runs using recycled media were continued to reduce wastewater and production costs. We completed the 4 consecutive batches of ZnS NanoFermentation in the 100-L vessel (Table 3-2). Results from operating the 100-L reactor reliably were essential for operating the 800-L reactor successfully.

**Table 3-2. Consecutive ZnS batches from the 100-L reactor**

| Batch | Incubation condition (based on 10 mM glucose, 6 mM thiosulfate) | Zinc input | Yield (g) | ACS (nm) |
|---|---|---|---|---|
| 1st | 1day in fresh medium | 6mM | 62.9 | 4.9±0.2 |
| 2nd | 1day in 60% ingredient equivalent refresh medium | 7mM | 55.5 | 8.2±0.3 |
| 3rd | 5day in 60% refresh medium | 7mM | 46.4 | 4.8±0.2 |
| 4th | 1day in 100% refresh medium | 7mM | 30.5 | 6.3±0.2 |

*2-day cell enrichment and hydrogen sulfide development before $ZnCl_2$ dose.

We draw several conclusions from the results in Table 3-2. First, consecutive runs in a batch using recycled media had lower yields, even with the replacement of 40% medium. Second, the average crystallite size of the product varied, depending on changes in conditions as well as the efficiency of NP harvest from the reactor. Suspended and unrecovered fine ZnS particles can lead to a larger crystallite size in subsequent batches, because they act as seeds. Third, the final product was much darker than previous final products (Figure 3-14a).

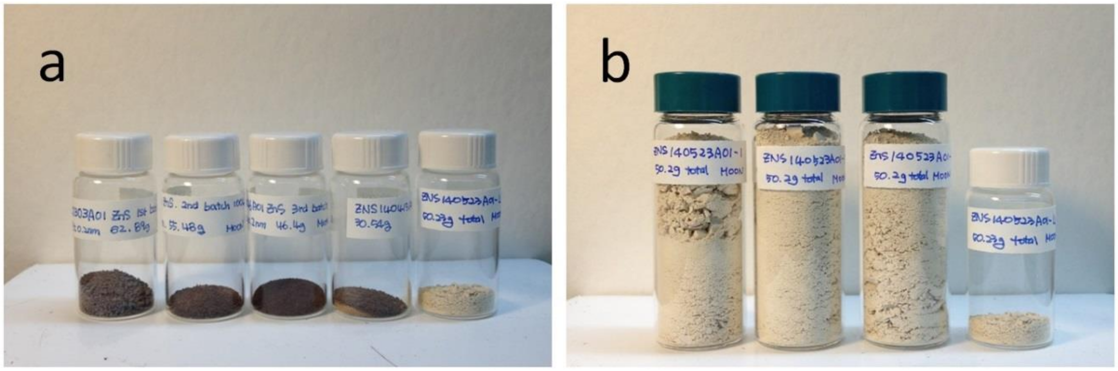

**Figure 3-14. Freeze dried ZnS final products. a) The first four vials came from 4 consecutive runs, while the fifth came from the first reproducibility test. b) Bright 50.2 g of ZnS from the first reproducibility test**

To understand the source of the dark brown coating, we examined the quality of the building's distilled water supply. These experiments used 1-L scale reactors with different water sources, varying exposure time to air after harvesting, or pH buffers (Table 3-3). After ZnS was formed there was no difference caused by air-exposure time. However, the use of high-quality deionized water (Type 1; >18 MΩ/cm) produced lighter colored ZnS material, more similar to the product from small-scale experiments. FeS medium using HEPES buffer instead of MOPS in the conventional TOR-medium recipe also produced less discoloration. Therefore a new series of experiments to test reproducibility was initiated with deionized water and 100% fresh medium for each run. The first and the second runs for produced 50.2 g and 53.4 g of ZnS as the usual, light-colored product (Figure 3-14b).

**Table 3-3. Examination of water quality impacted on nanoparticle precipitates**

| | **Deionized water** | | | | **Distilled water** | |
|---|---|---|---|---|---|---|
| Medium by used buffer | (1) FM | (2) FeS | (3) FM | (4) FeS | (5) FM | (6) FM |
| Oxygen removal by | boiling | boiling | boiling | boiling | purging | boiling |
| Air-contact after harvest | 2 hr | 2 hr | 24 hr | 24 hr | 2 hr | 2 hr |
| Freeze dried color | 10YR 8/4 | 2.5Y 8/2 | 10YR 8/3 | 2.5Y 8/2 | 2.5Y4/2 | 2.5Y 7/1 |
| | 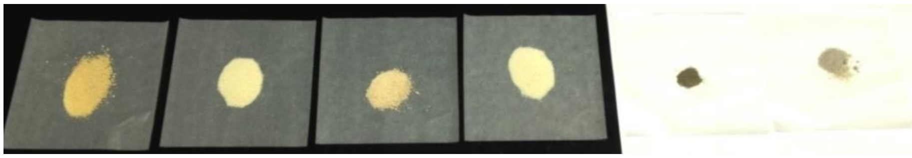 | | | | | |

Subsequently, we found a mixture of metal debris in the product, caused by the corrosion of metal parts from the gas-tight stirring motor (Figure 3-15a) on the top lid of reactor. We removed the corroded metal parts and replaced with a silicon gasket rated at 260°C (Figure 3-15b).

Finally, a specially manufactured Viton gasket was introduced to isolate the stirring motor from corrosives in the reactor. The reproducibility test of multiple single runs based on the same starting condition with 100% fresh medium in the 100-L reactor was completed using this Viton gasket that exhibited very similar yields and fine ACS (Table 3-4). The consecutive runs resulted in lower yields using recycled media and the average crystallite size of the product varied, depending on changes in conditions as well as the efficiency of NP harvest from the reactor. The reproducibility test resulted in much narrower crystallite size distribution and consistent production yields.

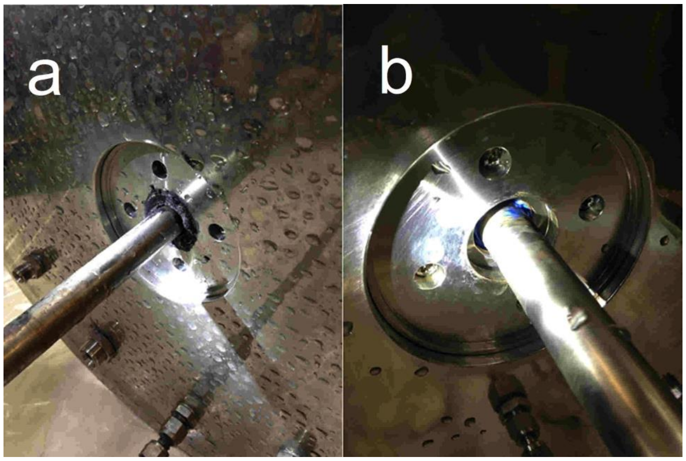

**Figure 3-15. a) Corrosion of a metal part from the stirring motor inside the reactor and b) silicon gasket maker to reduce corrosion resulted in silicon debris**

**Table 3-4. Reproducibility test using consecutive ZnS batches from the 100-L reactor**

| Batch | Incubation condition (based on 10 mM glucose, 6 mM thiosulfate) | Zinc input | Yield | ACS (nm) |
|---|---|---|---|---|
| 1st | Fresh medium buffered with HEPES | 6mM | 50.2 g | 2.1±0.1 |
| 2nd | Fresh medium buffered with HEPES | 6mM | 53.4 g | 2.2±0.1 |
| 3rd | Fresh medium buffered with HEPES | 6mM | 33.2 g | 1.8±0.1 |

During this period, we tried to reduce organic coatings on the ZnS NPs by controlling medium composition. Yeast extract is required to provide nutrients in the medium, but it contains amino acids that can interact with nanoparticle surfaces. Medium omitting yeast extract was prepared and dosed from 0 to 0.05% (the standard concentration). Reducing yeast extract caused a decrease in cell growth. Another experiment replacing yeast extract with ammonium chloride (0.1% to 0.5%) resulted in very poor enrichment (Figure 3-16).

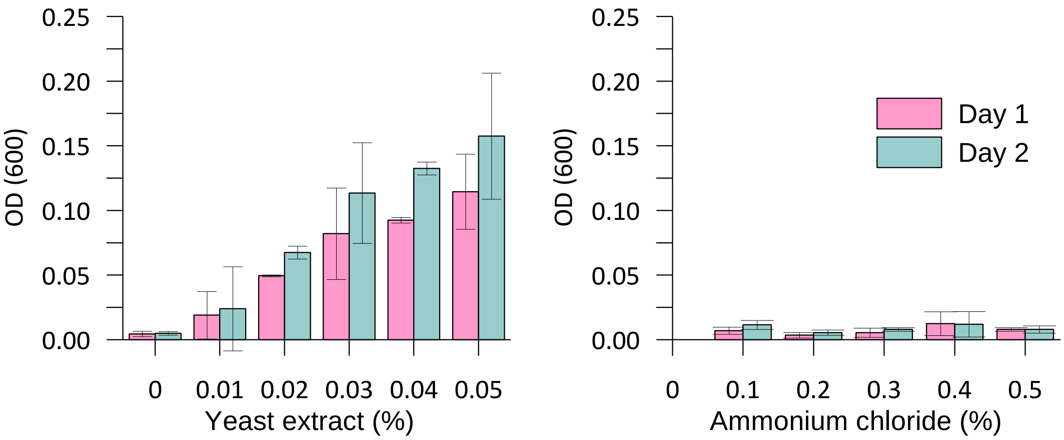

**Figure 3-16. Explored condition by controlling yeast extract and ammonium chloride concentration**

To test whether the increased salt concentration enhanced or inhibited cell growth during media recycling, another batch was tested with twice the usual concentration of NaCl. After one day of growth in 2X-NaCl FeS medium (FeS2) and FM medium, duplicate 10-mL aliquots containing a low cell turbidity were removed and filtered. Aliquots of 5-mL filtered medium were added to new 2X-concentrated medium (5 mL) and then inoculated with a 2% volume of turbid cell suspension. Cells grew well in both media, and the increased NaCl concentration enhanced cell growth (measured by turbidity). Therefore the increased NaCl concentration in recycled medium containing HEPES buffer and 2X-NaCl for up to 3 serial transfers did not hinder microbial activities (Figure 3-17a). These positive results could not explain the decreased yield of ~50 g NPs from the 100-L batch reproducibility test using FeS2 medium buffered with HEPES, compared to the >62 g yield from the first batch.

However, the cells growing in recycled media were impaired in their ability to form NPs. Tubes containing cells growing in HEPES buffer with either 1X-NaCl (1 g) or 2X-NaCl (2 g) produced less ZnS compared to cells grown in FM medium buffered with MOPS, even though the cells grown with thiosulfate reached a higher turbidity. The smell of sulfide from cultures reducing thiosulfate during growth in FeS2 medium was mild compared to the severe smell in the consecutive batch using FM medium with MOPS. Therefore recycling media containing HEPES buffer might inhibit ZnS NP formation. Therefore the MOPS buffer was planned to be used in future 900-L experiments.

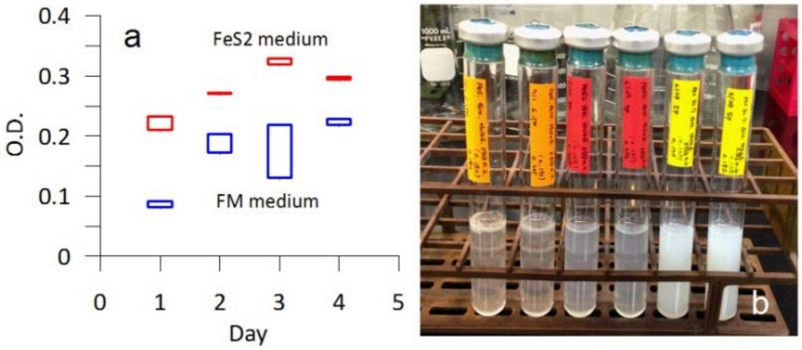

**Figure 3-17. a) Cells grown in recycled $FeS_2$ medium with 2X-NaCl reached a higher turbidity (optical density) compared to cells grown in FM medium. b) Cells grown in fresh FeS medium (orange label) produced less ZnS than cells grown in $FeS_2$ medium (red label) or FM medium (yellow label)**

**Figure 3-18. The 900-L reactor (left) was tested with water, while the 100-L reactor (right) was producing ZnS nanoparticles. Inset shows the inside of 900-L reactor while filling up with deionized water**

The larger 900-L reactor in the MDF pilot plant was bleached, washed, and filled with water using a flow meter. To fully immerse all pipes and sensors from the lid, 900 L of water was added to the reactor (inset of Figure 3-18). A purging line was extended and a sampling loop was added. The reactor went through a test run, demonstrating that the heated, circulating water bath had enough capacity to hold the reactor temperature at 65°C for 2 weeks without any spill or leak. The stirring motor was upgraded with a custom-made gasket and new shaft design, as described for the 100-L reactor, above.

### 2.3.11 Demonstrate 900 L pilot plant showing 20X increase in production (kg vs. 10 g batches)

The nominal 800-L reactor in the MDF pilot plant was adjusted to a 900-L volume after measuring the volume of liquid required to immerse the impeller, stirring arms, and all sampling ports. The safe work flow procedures for the pilot plant 900-L reactor were updated and strengthened, because one order scale up from 100-L to 900-L can increase the severity of hazards (Figure 3-19). The actual first run of 900-L pilot plant reactor was initiated by filling the vessel with >700L deionized water (>18 MΩ) and pasteurized at 65 ºC for one week (Figure 3-20). The remaining volume was filled with additional sterilized and degassed deionized water and condensed, sterile media using a nitrogen gas-flushed anoxic connector. At the same rate used for the small scale reactor, 6 mM of sodium thiosulfate as a sulfide source, 10 mM of glucose, and 18 L of seed bacteria stock solution in the mid-log growth phase were added when the reactor solution temperature reached 65 ºC. After 48 hour enrichment of *Thermoanaerobacter* X513 with $H_2S$ development, a 5 mM zinc chloride stock solution was dosed. All lines and tubing were purged with nitrogen gas, and needles were used on both ends. After 24 hour, a milky suspension formed in the reactor, consistent with the targeted ZnS product phase (Figure 3-20).

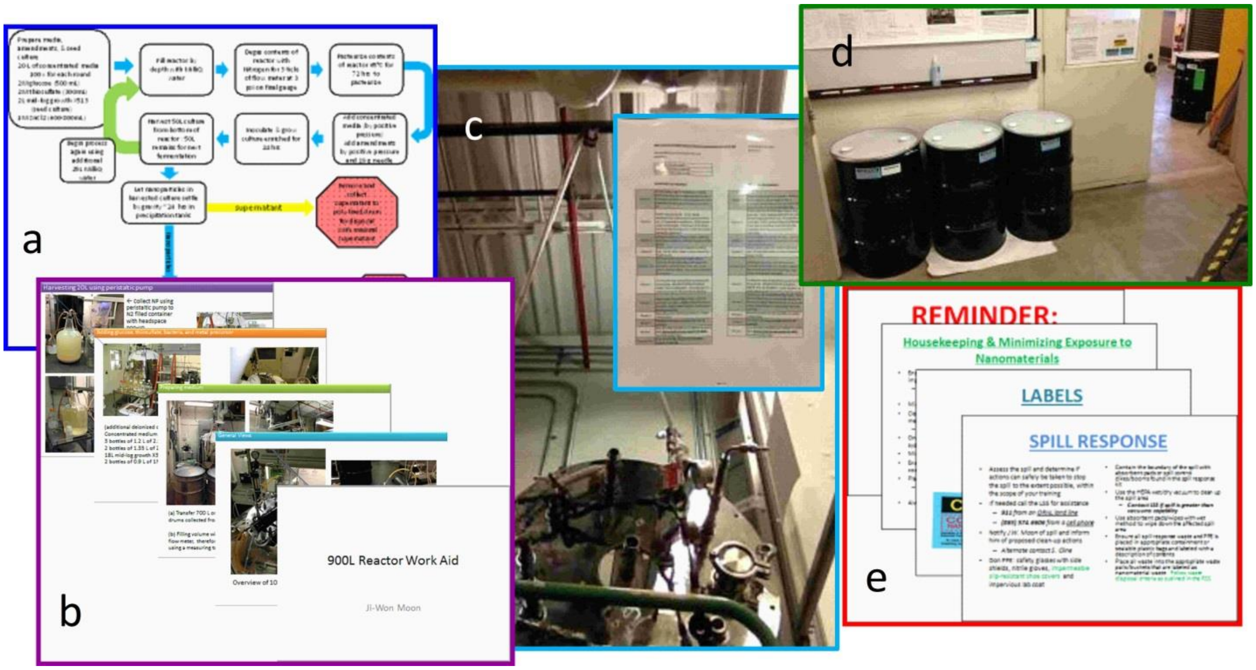

**Figure 3-19. Updated safety tools: a) experimental work flow, b) 900-L reactor run work aid that is continuously updated with troubleshooting information, c) hoist and rigging work aids, d) waste stream, and e) emergency spill response**

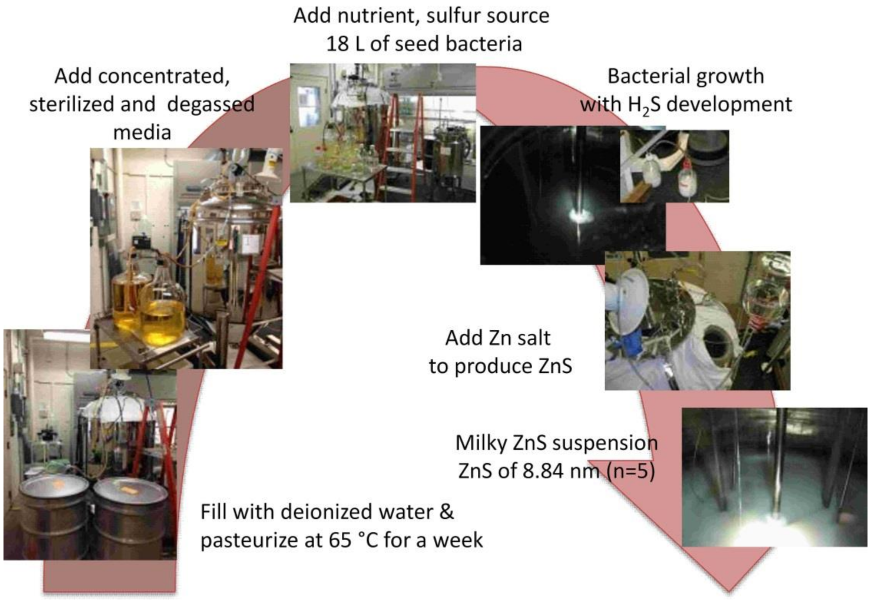

**Figure 3-20. Experimental work flow for the first run of 900-L pilot plant reactor**

During the harvesting/washing stage, several problems were identified that were not found in the 100-L scale reactor. At first, the precipitate acted like a slurry, not a crystalline phase (Figure 3-21a). Centrifugation appeared to separate the product into heterogeneous phases (Figure 3-21b). Samples concentrated in ~6 L of liquid exhibited a pinkish brown color (Figure 3-21c). Even after repeated harvesting of material using a peristaltic pump to draw liquid from the bottom of the reactor, a large volume of NPs remained on the shallow slope of the fermentor cone (Figure 3-21d). We assumed that the continuous cell growth (usually 3 days to stationary phase) coincided with further $H_2S$ development due to the slow rate of cooling the large-volume reactor to room temperature. A small subsample exhibited a much brighter color when abrupt cooling and nitrogen gas purging were deployed to suppress microbial activity and accumulation of $H_2S$ (Figure 3-21e). The pinkish brown color might have come from enriched cell and organic residue produced during prolonged incubation due to the slow cooling and harvesting, followed by crystal growth of suspended and unrecovered ZnS fines. Despite the different color, all final phases (N=5) were ZnS but the average crystallite size was 8.8 nm compared to the conventional 2-3 nm size.

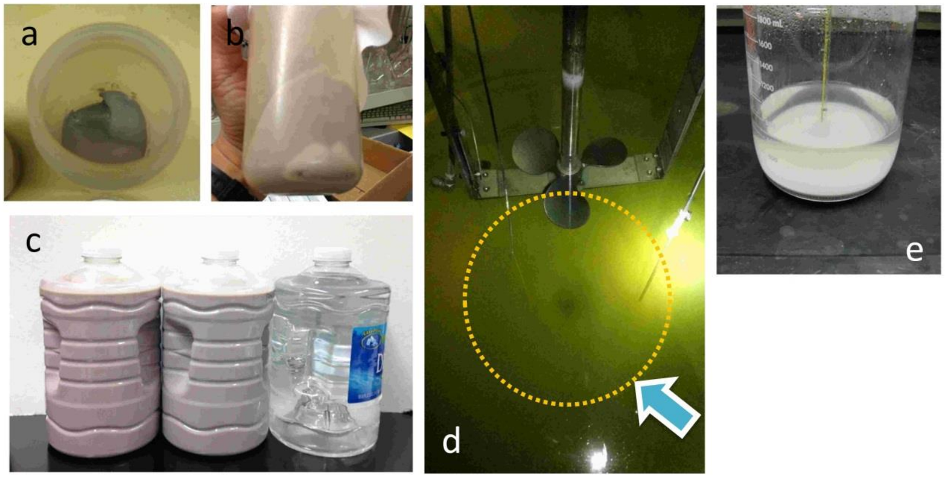

**Figure 3-21. The physical properties and behavior of final product from the first run of 900-L reactor**

With an updated experimental design, we started the second run of the 900-L reactor. Reaction progress was monitored through the reactor window, and continuous manual pH titration during incubation was performed with 10 M anoxic NaOH (Figure 3-22a). To terminate cell growth and associated reactions, the system was cooled rapidly (Figure 3-22b) to emulate the rate of cooling used to transfer small-scale reactions from a 65 ºC incubator into 20 ºC room temperature. The cooling process involved a) switching heating from 65 ºC to 5 ºC cooling in the circulating water bath, b) exchanging the 65 ºC bath water with 3 ºC deionized water kept in the cold room, and c) adding frozen packs of blue ice that can keep the circulation water at no more than 40 ºC. This procedure dramatically cooled the reactor to 5 ºC overnight compared to a 48-hour air-cooling process that reduced the temperature to 30ºC. A much smaller amount of unreacted hydrogen sulfide was detected in the zinc acetate trap (Figure 3-22c & d). This indicated that no excess Zn ions carried over to the next consecutive batch. As shown in Figure 3-22e, the sample volume after one-day of settling is much larger than the 1st run (inset of Figure 3-22e) and had a brighter color.

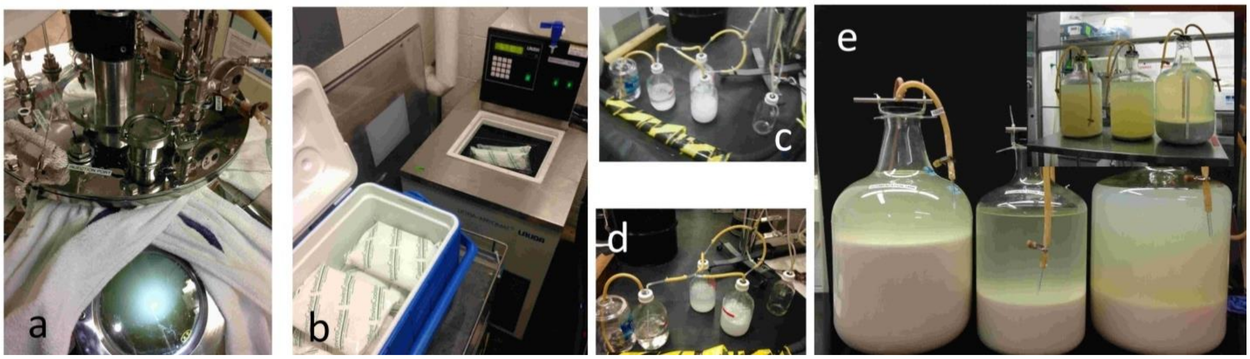

**Figure 3-22. Rapid cooling procedure produced conventional ZnS NPs from the 900-L fermentor**

As mentioned earlier, the compacted 6-L volume of ZnS from the 1st run (Figure 3-23a) weighed 275 g after freeze-drying (Figure 3-23b), which was only 61% of the expected scale-up yield of 450 g based on results from small-scale and 100-L scale experiments. For the 2nd run, post-treatment including washing produced a cleaner and brighter final product (Figure 3-23c), which had roughly 15 L of settled volume. This product could increase the yield by 250% compared to the first run (Figure 3-23d).

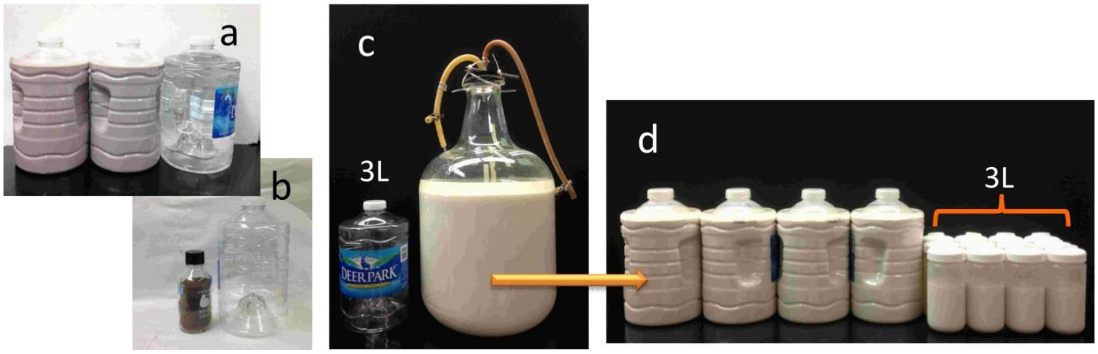

**Figure 3-23. Rapid cooling procedure regained conventional properties of ZnS final products**

The previous series of consecutive batches at the 100-L scale showed interference by high organic carbon from the building's distilled water supply and a shortage of nutrients in successive batches. Therefore we planned to run a third batch in the 900-L fermentor using 100% nutrient replacement to determine whether recycling the used medium is beneficial to the production cost, quality and yield of final products or not.

### 2.3.12 Successful coupling 100 L and 800 L fermentors

The mean value of average crystallite size measured from 5 subsamples from the first run of 900-L pilot plant reactor was 8.8 nm (Table 3-5). Potential causes of differences between the 100-L and 900-L scale experiments were tracked down and resolved. While the shallow slope of the 900-L fermentor cone retained precipitates after several harvests, slow cooling due to the high heat capacity of the reactor promoted continuous growth of cells, and the production of excess hydrogen sulfide interfered with crystal growth and purity. The second consecutive run adapted rapid cooling by switching the heating unit to a cooling unit, replacing hot water in the circulating bath with refrigerated deionized water, adding ice packs to keep the temperature below 40 °C where the thermophilic bacteria are inactive, and purging the system with a high flow rate of nitrogen for 3 days to displace hydrogen sulfide gas.

**Table 3-5. Bio-ZnS production using 900-L reactor with the continuous batch mode**

| Batch | Size (L) | $S_2O_3$ (mM) | $Zn^{2+}$ (mM) | Medium | size | yield |
|---|---|---|---|---|---|---|
| 1st | 900 | 4 | 5 | Fresh | 8.84 nm (n=5) | 273 g (60.7% of Est. yield) |
| 2nd | 900 | 5.33 | 5 | 33% new ingredient | 2.98 nm (n=4) | 322 g (71.6% of Est. yield) |
| 3rd | 900 | 6 | 8 | 100% new ingredient | - | Terminated with little crystalline phase |

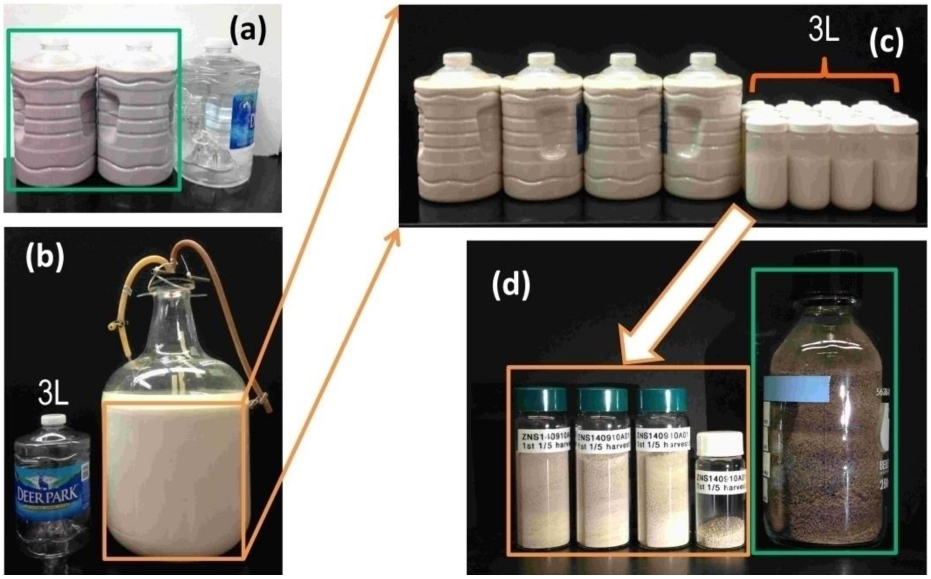

**Figure 3-24. The 900-L reactor production and process. (a) 6-L volume precipitate from the first run; (b) 15-L volume precipitate from the second run; (c) Dispensed into 3-L container for washing process taken one and half month; (d) comparison of final product between first and second run**

The second consecutive 900-L batch produced a condensed nanoparticle slurry with 250% greater volume of ~15 L compared to 6 L (Figure 3-24b). Repeated centrifugation/dispersion for one and half months finished the complete washing process of harvested bio-ZnS. Averaged crystallite size of bio-ZnS from 5 dispensed samples was 2.98 nm (Figure 3-24c), which was close to the normal range of 2–3 nm, and it had a brighter color by adapting a sonication probe for washing. The first portion of the 2nd run with 33% refreshment of nutrients produced 58 g of nanoparticles (Figure 3-24d), and the full batch had 322g in total (Table 3-5).

Improvements to quickly cool the reactor, suppress crystal growth, and remove residual hydrogen sulfide gas increased the yield in the second batch by 18 % (322 g of ZnS nanoparticles). This yield increased despite adding only 33 % new ingredients and precursor chemicals to the recycled medium at the beginning of the second batch. This modification reduced the crystallite size from 8.8 nm to 3.0 nm, which is typical of smaller scale batches.

A 3$^{rd}$ batch with 100 % nutrient refreshment was examined but it was terminated due to little crystalline phase during washing stage. However, we successfully confirmed process up-scaling by biologically producing more than a half-kilogram of ZnS nanoparticles in consecutive batches using the 900-L reactor.

To confirm the reproducibility of the chemical composition and characterize the effects of additional dopants or trace elements on composition, we selected representative samples according to i) the reactor size such as 1-L, 24-L, 100-L, 900-L, ii) the biological pH buffer such as HEPES or MOPS, iii) either consecutive or multiple batch, and iv) changing washing water/solid ratio (Table 3-6). These samples were produced using the same recipe. The samples were shipped to a testing laboratory for inductively coupled plasma/optical emission spectroscopy (ICP-OES) analysis of selected metals.

**Table 3-6. Conditions of bio-ZnS synthesis with respect to reactor size, biological buffer, and material of reactor**

| No. | Description | Buffer | Material of reactor |
|---|---|---|---|
| 1 | Reproducibility test 3rd run at 24L: 5 day incubation | HEPES | Glass |
| 2 | Exposure comparison at 1L | MOPS | Glass |
| 3 | Consecutive run 1st at 100L | MOPS | Stainless Steel |
| 4 | Reproducibility test 1st run at 100L | HEPES | Stainless Steel |
| 5 | Consecutive run 1st at 900L | MOPS | Stainless Steel |
| 6 | Consecutive run 2nd at 900L-3rd bottle, more washed | MOPS | Stainless Steel |

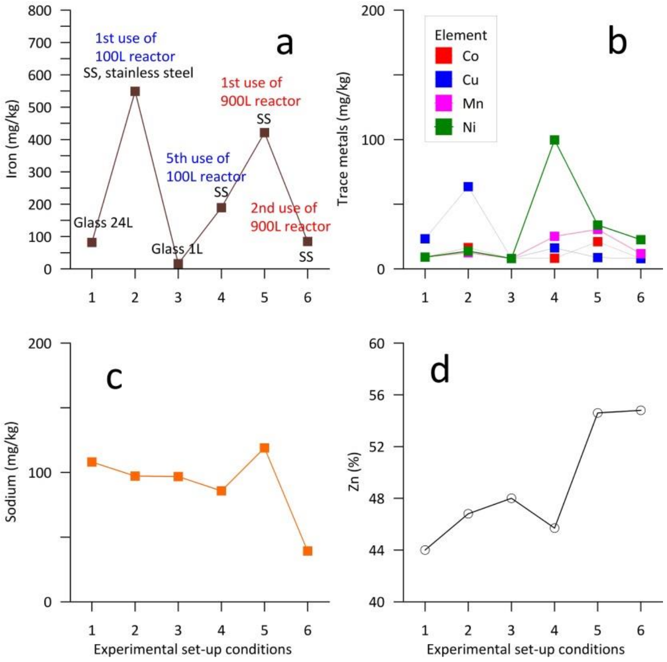

**Figure 3-25. Rapid cooling procedure regained conventional properties of ZnS final products**

One of the dominant metal impurities was iron (Figure 3-25a); however, it appeared as a contaminant only in the first batches from the 100-L and 900-L stainless steel reactors. At the second usage the impurity level went down to normal. Low levels of metal contamination can be caused by impurities in reagent chemicals. The purities of chemicals used to make basal medium, vitamin and mineral solutions in media varied from 97 % to 99.5 %. Most transition metals including Co, Cu, Mn, and Ni were more abundant in nanoparticles from stainless steel reactors than glass as expected (Figure 3-25b), but the two anomalous peaks of Cu and Ni seem to be artifacts caused by serial dilution and high detection limits (close to 90–100 ppm). The concentration of sodium in the biological growth medium was at least 20,000 ppm, but sodium was easily washed away to 100 ppm. Treatment by sonication probe could further reduce sodium levels by half by aggressive breaking of aggregates during the washing step (Figure 3-25c). The Zn contents had two trends: the ZnS samples produced in small reactors appeared relatively sulfur-enriched, while the two samples from the 900-L reactor appeared sulfur-deficient (Figure 3-25d). We cannot rule out the possibility that these differences in Zn composition reflect an analytical artifact due to dilution error required to prepare the ppm-concentration samples that are suitable for ICP-OES analysis.

Another success was achieving the milestone of coupling 100-L and 900-L fermentors to increase the efficiency of nanoparticle production. While nanoparticles were harvested from the larger reactor, the smaller reactor was used to pasteurize fresh water or growth medium (Figure 3-26a). This prepared solution was subsequently added to the recycled medium in the larger fermentor using a peristaltic pump while purging the headspace of the smaller reactor (Figure 3-26b).

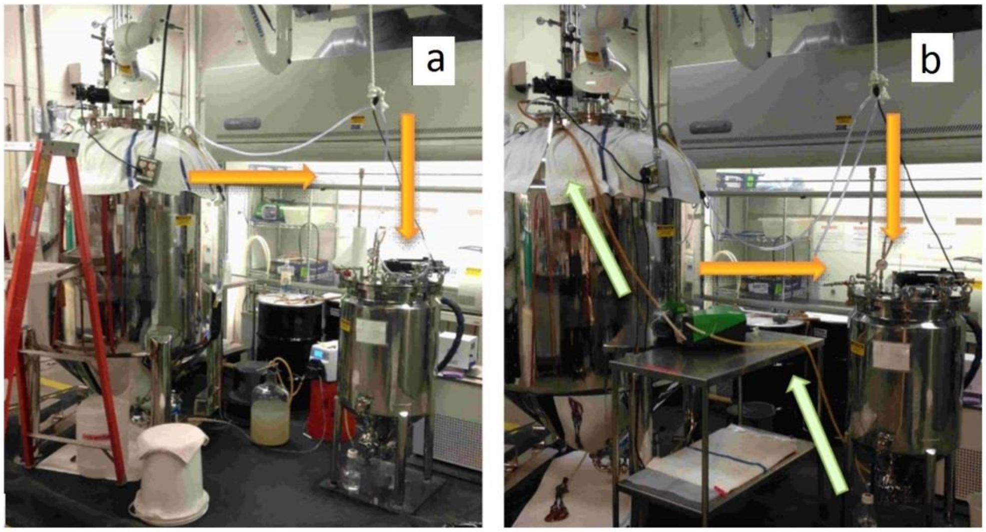

**Figure 3-26. Coupling 100-L and 900-L fermenters to enhance the efficiency**

### 2.3.13 Automatic pH control with minimal organic buffers

A new NanoFermentation method using an automatic pH-titrating instrument to produce silver-doped ZnS was tested to reduce the cost of production while trying to improve nanoparticle quality and yield. In a 100-L reactor with appropriate probes and sampling ports, controlling pH using a concentrated sodium hydroxide solution cost ~1.65 cents/L in reagents, compared to 66–79 cents/L using organic Good buffers. The new process reduces the cost of chemicals for pH control by almost ~98 %.

A pH probe was installed at the base of a 100-L reactor, and the growth medium was stirred at ~40 rpm (Figure 3-27a inset). For the first batch, the pH was measured regularly using the probe inside the reactor, as well as a second external probe. The fluctuation of pH resulted in 6.5 ± 0.3 nm average crystallite size (ACS) of 5% Ag-doped ZnS with a dry weight of 22.3 g (Figure 8b upper inset). For the second batch we continuously added 0.1–0.3 mL/min of 10 M sodium hydroxide solution using a peristaltic pump by controlling the speed depending on external pH measurements recorded every 30 min for 36 hours (Figure 3-27a).

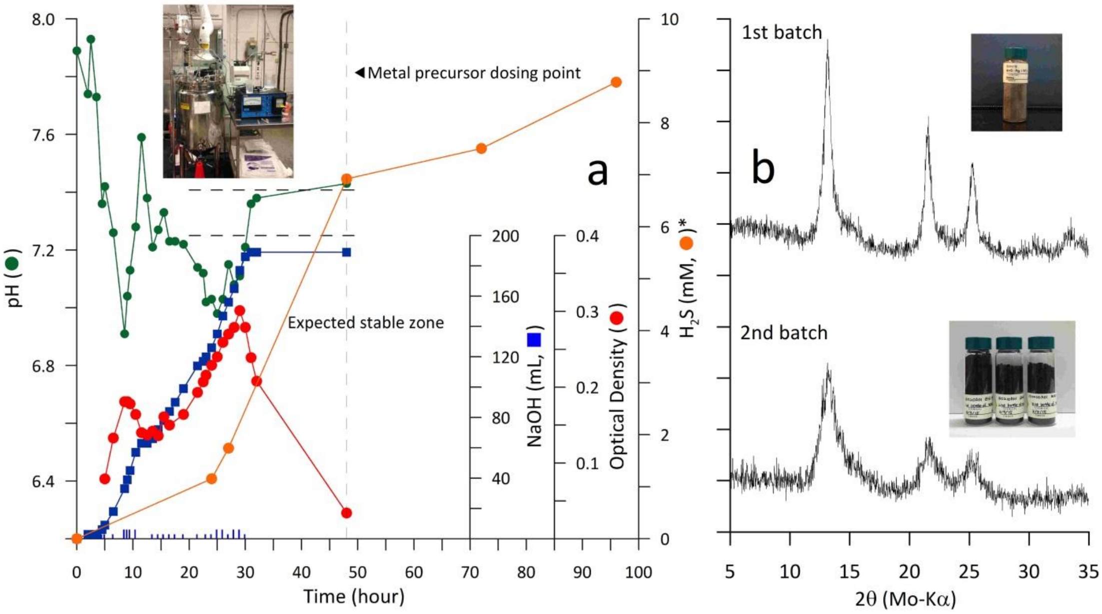

**Figure 3-27. a) Timecourse profile of pH, addition of NaOH (per 30 min and cumulative), and optical density during the synthesis of ZnS:Ag 10%. The inset shows the auto-titrator adjacent to the 100-L reactor, b) X-ray diffraction patterns from the 1st batch of 5% Ag-doped ZnS and 2nd batch of 10% Ag-doped ZnS, insets illustrate the yields**

The second batch with stabilization of pH and an increased silver doping rate resulted in smaller nanoparticles with 2.2 ± 0.1 nm ACS of 10 % Ag-doped ZnS. The yield substantially increased to 57.08 g of dry weight. ZnS:Ag (10 %) is expected to be 4.3 % heavier than the straight ZnS. Considering a previous 100-L reaction resulting in 51.8 g (average of 2 runs) of straight ZnS, ZnS:Ag (10 %) should have 54.02 g from 100 L. Therefore 57.08 g demonstrated great reproducibility with 5.6 % deviation, even though we used NaOH at < 3 % cost fraction of biological buffers.

The third auto-titrated batch in the 100-L reactor produced straight ZnS to compare the current automatic pH-titrating process to previous conventional NanoFermentation of ZnS. Therefore we can evaluate the scalability and reproducibility with an automatic pH-titrating technique compared to the case of expensive organic biological buffers. This straight ZnS batch from 100L produced 27.9 g of 2.3 ± 0.1 nm ZnS. The production rate after freeze drying approached only ~60 % of expected production amount. We cautiously added the 10 M sodium hydroxide based on 1st and 2nd titrating record, however, the pH log at the third batch exhibited an unexpected high peak overnight between 12 and 24 hour (Figure 3-28). After that the straight ZnS synthesis profile resembled that of the ZnS:Ag 10% batch: the pH gradually decreased to the ideal range of 6.8–7.0 for dosing $ZnCl_2$ stock solution to make small size ZnS (2–3 nm). The required volume of 10 M sodium hydroxide solution was also reduced from 189 mL to 145.8 mL by 23%. A qualitative sedimentation experiment using NaOH-buffered ZnS demonstrated improved potential for dispersion compared to biological-buffered ZnS (Figure 3-29). In conclusion, tight pH control that can maintain an ideal pH range was confirmed to yield a high production rate.

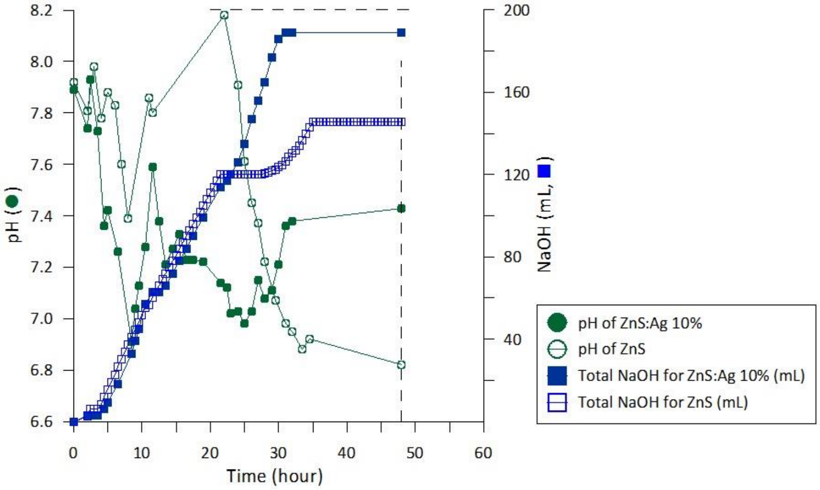

**Figure 3-28. Monitoring pH and addition of NaOH during the synthesis of straight ZnS as compared to the previous ZnS:Ag 10%**

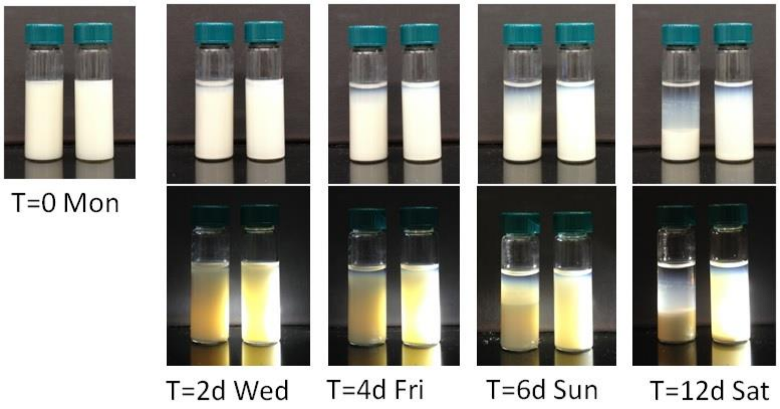

**Figure 3-29. Sedimentation timecourse experiment using NaOH-buffered ZnS; Left, dense sample right after washing; Right, sonicated ZnS from automatic pH-titrating supported NanoFermentation. The NaOH-buffered ZnS with appropriate sonication showed greater dispersion after more than 10 days. The bottom row shows the dispersion with a hand-held LED light source**

### 2.3.14 Product characterization compared to commercial product

We evaluated our randomly selected ZnS final products from the pilot plant reactors and their converted ZnO through controlled oxidation compared to general commercial products that can be easily accessible by public customers. The ZnO samples were obtained from the Roll-to-Roll team of MDF, used for their device fabrication; these originated from analyzed ZnS samples. Samples (Table 3-7 and Figure 3-29).

**Figure 3-30. Picture of analyzed ZnO and ZnS samples for comparison study.**

**Table 3-7. Analyzed sample description for ZnO and ZnS**

| Sample Names |
|---|
| ***ZnO*** |
| ZnO #1: transformed from ZnS of 2nd batch of continuous running 900-L reactor |
| ZnO #2: transformed from ZnS produced using new method (Invention disclosure DOE SN S-138,128) |
| ZnO #3: transformed from ZnS using automatic pH-titrating process |
| ZnO #4: nanoparticle dispersion (< 100 nm particle size) – Commercial with coating in suspension |
| ZnO #5: nanoparticle dispersion (< 100 nm particle size) – Commercial with coating in freeze-dried |
| ZnO #6: bulk material – Commercial |
| ZnO #7: nanoparticle (10-30 nm) – Commercial |
| ***ZnS*** |
| ZnS #8: from ZnS 2nd batch of continuous running 900-L reactor as-is without post or in situ treatment |
| ZnS #9: from ZnS produced using new method (Invention disclosure DOE SN S-138,128) |
| ZnS #10: from 100-L with an automatic pH-titrating process |
| ZnS #11: bulk material (10 μm) - Commercial |

Specific descriptions of commercial products were found from certificates of analysis according to the lot numbers. The color was read compared to a Munsell color chart and surfactant-covered ZnO (#5) and ZnS (#8 and #10) that were produced with the aid of direct microbial nucleation had readable color beyond the visibly white (Table 3-8). The pH values were obtained after 24 hr shaking from the mixture of solid:water = 1:10 ratio. Both commercial ZnO (#7) and ZnS (#11) had very high (9.56) or very low (3.07) pH compared to most NanoFermented or commercial products. The newly invented process resulted in a little acidic product (#9 at pH 4.97).

The average crystallite size was calculated by Scherrer's equation from the obtained XRD patterns. Particle (aggregate) sizes were analysis by dynamic light scattering (DLS) used the slurry mixed with deionized water after 24-h shaking and 5-min sonication in iced water. Among ZnO samples NaOH-titrated (#3) and commercial products (#4 and #5 irrespective of freeze-drying as well as #7) exhibited less than 100 nm aggregated particle sizes. In contrast, as-is bio ZnS samples regardless of methods (#9 and #10) that had been recently filed as invention disclosures showed ~50 nm size which is very close to the previous champion result after tons of post-treatment (~25 nm).

**Table 3-8. Basic physicochemical properties of ZnO and ZnS**

| Sample | Manufacturer's Description | Measured Color (Munsell Color Chart) | pH | Crystallite size | Meas. PS |
|---|---|---|---|---|---|
| ZnO #1 | | White (GLEY1 9/10Y) | 7.18 | 84.7 ± 10.7 nm | 3.47 ± 0.195 μm |
| ZnO #2 | | White | 7.25 | 121.6 ± 20.3 nm | 363 ± 31.3 nm |
| ZnO #3 | | White | 7.79 | 99.6 ± 14.9 nm | 94.0 ± 7.2 nm |
| ZnO #4 | Off White to Tan | 10YR 7/4 | 7.55 | | 60.6 ± 0.4 nm |
| ZnO #5 | | | 7.53 | 34.6 ± 1.8 nm | 62.3 ± 0.1 nm |
| ZnO #6 | | White | 7.62 | | 215 ± 4.7 nm |
| ZnO #7 | Milky White | White | 9.56 | | 49.9 ± 1.6 nm |
| ZnS #8 | | 10YR 7/2 | 5.62 | 1.9 ± 0.1 nm | 3.63 ± 3.93 μm |
| ZnS #9 | | White | 4.97 | 1.9 ± 0.1 nm | 53.3 ± 0.9 nm |
| ZnS #10 | | 2.5YR 8/1 | 7.64 | 2.1 ± 0.1 nm | 46.5 ± 1.8 nm |

| | | | | | |
|---|---|---|---|---|---|
| ZnS #11 | White to Yellow | White | 3.07 | 35.9 + 1.9 nm | 192 ± 1.7 nm |

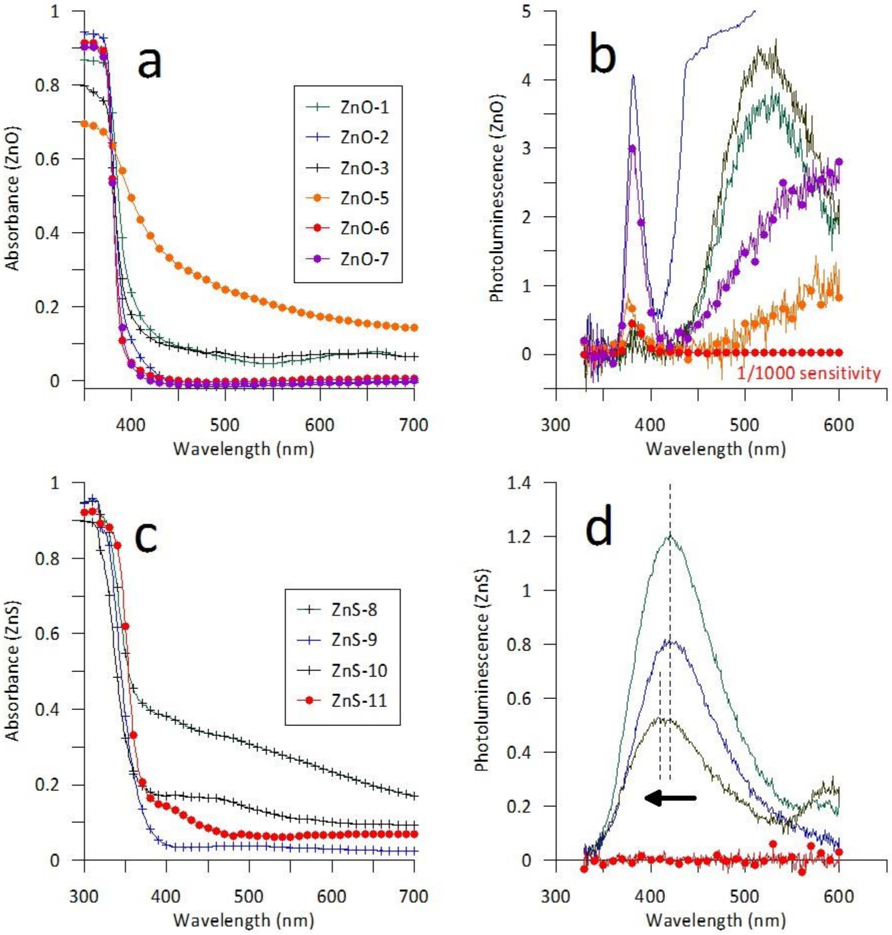

**Figure 3-31. Optical properties of ZnO and ZnS. a) absorbance and b) photoluminescence of ZnO, c) absorbance and d) photoluminescence of ZnS**

The most common application of ZnO and ZnS is to optical devices, therefore basic absorbance and photoluminescence excited by a He-Cd laser at 325 nm were measured. As shown in Fig. 3-31, among ZnO, the procedure described in a new-invention disclosure produced less defects, close to commercial (circle) having low background in absorbance except the surfactant coated commercial product (#5). Photoluminescence measurements of ZnO samples exhibited that only the new invention disclosure sample and commercial #7 had expected ZnO emission. However, no NP sample matches bulk size, single crystalline ZnO in emission in 2 orders of magnitude. Among ZnS samples the new-invention disclosure exhibited a low background in absorbance compared to a commercial bulk phase sample, indicating less defects, smaller size, and homogeneous size distribution. However, NaOH-titrated ZnS samples (#10) showed a blue-shift by smaller particle size and homogeneous size distribution.

To confirm the surface structure modified by coatings, FTIR analysis tried to identify differences among ZnS samples including conventional NanoFermentation (#8), new-invention disclosure (#9), and NaOH-titrated NanoFermentation (#10) samples. As shown in Fig 3-32, there was no predominant difference among samples prepared by bacterial nucleation-aided NanoFermentation. However the new process dominantly removed the amine bands, which are caused from protein and lipid (Fig. 1-57).

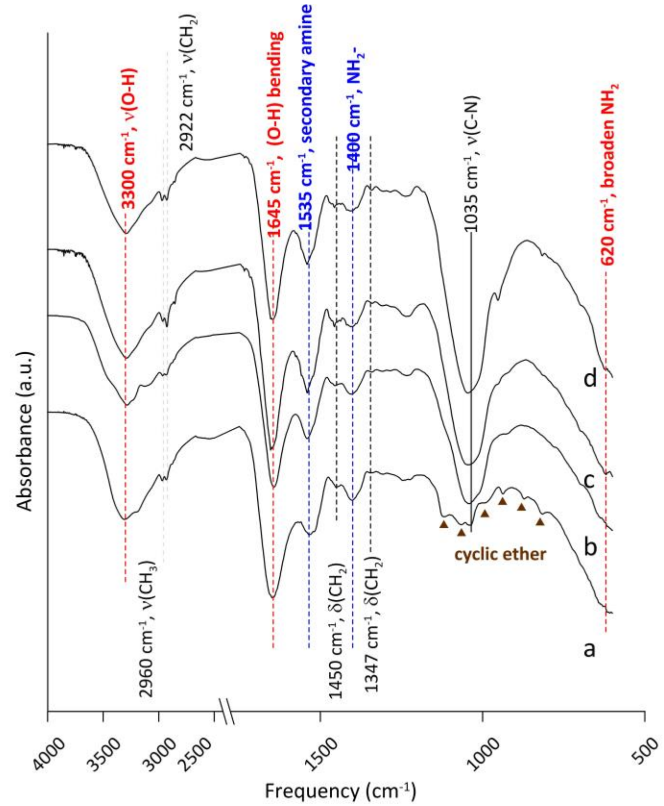

**Figure 3-32. Comparative FTIR analysis of the ZnS NPs from (a) FM medium (MOPS buffer) and (b) FS medium (HEPES buffer), (c) 10% ZnS:Ag (NaOH titration) and (d) ZnS (NaOH titration)**

We could differentiate the existence of amine, but the relative amounts of carbon and nitrogen were unclear by FTIR. Carbon and nitrogen determination exhibited only one commercial ZnO showed least surface residue (Fig. 3-33). In contrast, the new invention disclosure sample has C and N similar to commercial bulk ZnS, and NaOH-titrated ZnS had higher C & N than conventional NF synthesis.

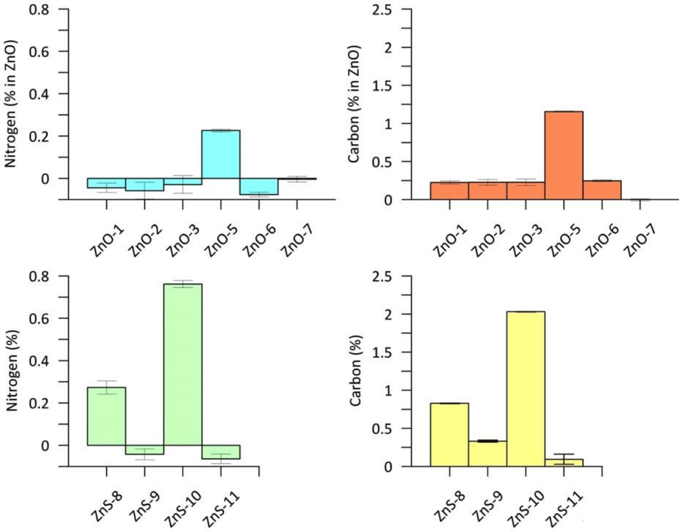

**Figure 3-33. Carbon and nitrogen determination**

# 3. ACCOMPLISHMENTS AND CONCLUSIONS

## 3.1 NANOMATERIAL PRODUCTION USING NANOFERMENTATION

Tasks in this project produced twelve new types of nanoparticles using NanoFermentation and shared them with collaborators and industrial partners for testing and device fabrication (Table 4-1). Furthermore, nine more nanomaterials that were previously produced by this method were up-scaled or improved in the MDF project, creating larger quantities of enhanced quality nanoparticles for energy-relevant applications. In addition to these collaborative research activities, results from this work were disseminated through numerous invention disclosures, patents, publications, presentations and commercialization activities described below.

**Table 4-1. Summary of new nanoparticles manufactured by NanoFermentation.**

| Nanoparticles | Maximum scale of production | Max. reactor volume | Average crystallite size (ACS*) | Property[#] | Collaborator /Industrial partner | Application |
|---|---|---|---|---|---|---|
| **Substituted Magnetites** | | | | | | |
| Cobalt-doped magnetite ($Co_{0.3}Fe_{2.7}O_4$) | 25 g (wet) | 1 L | 25-50 nm | lower Curie temperature | ORNL Additive Manufacturing | Polymerization Magnetism |
| Manganese-doped magnetite ($Mn_{0.6}Fe_{2.4}O_4$) | 20 g (wet) | 1 L | 25-50 nm | lower Curie temperature | ORNL Additive Manufacturing | Polymerization Magnetism |
| Zinc-doped magnetite ($Zn_{0.6}Fe_{2.4}O_4$) | 3 × 100 g | 30 L | ~20 nm | magnetism | NPMR | Magnetic |
| Zinc-doped magnetite (Zn 1%, 5% and 10%) | 2 × ~3 g | 500ml | 15.3-30.7 nm,12.3-25 nm 12.6-17.7 nm | Precursor for Iron nitride | ARPA-e project: AMC, Univ. of Minnesota, ORNL | Magnetic, memory |
| Ga- and Ho-doped magnetites | < 5 g | 1 L | 25-50 nm | lower Curie temperature | ORNL MDF | Polymerization Magnetism |
| **Metals** | | | | | | |
| Elemental cadmium (electrochemical) | 1.07 g | 250mL | | Anti-corrosion | | Batteries, aeroplane |
| Elemental copper (capped) | 0.1 – 0.2 g | 1 L | 28 - >100 nm | Electrical conductivity | | Electric board, capacitors |
| **Metal Gallates** | | | | | | |
| Co-doped Zinc gallate | 14.8 g | 24 L | 3.0-3.4nm | Blue emission | Testing at PKNU<br>MDF R2R | Phosphor |
| Cr-doped Zinc gallate | 13.9 g | 24 L | 3.0-3.4nm | Red emission | Testing at PKNU<br>MDF R2R | Phosphor |
| Mn-doped Zinc gallate | 14.3 g | 24 L | 3.0-3.4nm | Green emission | Testing at PKNU<br>MDF R2R | Phosphor |

| Nanoparticles | Maximum scale of production | Max. reactor volume | Average crystallite size (ACS) | Property | Collaborator /Industrial partner | Application |
|---|---|---|---|---|---|---|
| **Metal Sulfides** | | | | | | |
| Cadmium sulfide (capped) | >45 g | 24 L | 4-5 nm | Emission | Testing | Quantum dots |
| Cobalt sulfide | 0.67 g | 1 L | | Precursor of metal oxide | TMDF R2R | Insulator, resistor |
| Copper antimony sulfide | | < 50mL | | Thermoelectric | Testing | Thermoelectric |
| Copper sulfide | 13.1 g | 24 L | 12.3 nm | Binary CZTS component of photovoltaic | DuPont | photovoltaic |
| Nickel sulfide | 6.7-9.2 g | 24L | 6.7-7.3 nm | Precursor for NiO | MDF R2R | High temp. insulator,<br>NiO precursor |
| Tin sulfide | 17.1 g | 24 L | 10.2 nm | Binary CZTS component of photovoltaic | DuPont | Photovoltaic, SnO precursor |
| Zinc sulfide | 2 × 300 g<br>3 × 50 g | 900 L<br>100 L | 2-3 nm<br>2.1-2.2 nm | Emission | TopFive Inc., Nano-elements LLC, MDF R2R | Solid state light, ZnO precursor |
| Zinc sulfide (NTA-treated) | 5.8 g | 24 L | <5 nm | Enhanced emission | DuPont | Solid State Light<br>Flat display |
| Zinc sulfide (capped) | 33 g | 24 L | 2.5 nm | Enhanced emission | Testing | Quantum dots |
| **Substituted Zinc Sulfides** | | | | | | |
| Copper-doped ZnS (Cu 0.8%) | 0.5-1 g | 1 L | 6.5-10 nm | Green emission | MDF R2R | Flat display |
| Silver-doped ZnS (Ag 5% and 10%) | 22.3 g<br>57 g | 100L | 6.5 nm<br>2.2 nm | Antibacterial<br>Antifungal agent precursor | CNMS<br>Iowa State Univ.<br>Texas Tech Univ. | Gels, creams, wound dressing composites |

## 3.2 PATENTS

Invention disclosures

- Invention #3291 (S-124,904) “Biogeochemically selective extraction of REE and Metal from Geothermal Brines”
- Invention #3337 (S-124,957) “Microbially-mediated method for nanoparticle formation and films thereby”
- Invention #3497 (S-138,128) “Improved properties of nanomaterials using complementary NanoFermentation technique”
- Invention #3501 (S-138,132) “Low-cost precursor for synthesis of Fe-N magnet powders”
- Invention #3514 (S-138,146) “Bacterially Synthetized Particles for (Multifunctional Antibacterial/Antifungal etc. Applications) in Powders, Solutions, Gels, Creams, Wound Dressing Composites”

Patents

- U.S. #8,759,053 awarded Jun 24, 2014. Phelps, J.J., Lauf, R.J., Moon, J.-W., Rondinone, A.J., Love, L.J., Duty, C.E., et al. “Microbially-mediated method for synthesis of non-oxide semiconductor nanoparticles”
- U.S. 61/777,005, "Controllable Reductive Method for Synthesizing Metal-Containing Particles"
- U.S. 61/777,009, "Electrochemical Method for Synthesizing Metal-Containing Particles and Other Objects”
- U.S. 61/777,012, "Method for Synthesizing Metal Oxide Particles"

## 3.3 PUBLICATIONS AND PRESENTATIONS

Publications

- Moon, J.-W., Ivanov, I.N., Duty, C.E. Love, L.J., Rondinone, A.J., Wang, W., Li, Y.-L., Madden, A.S., Mosher, J.J., Hu, M.Z., Suresh, A.K., Rawn, C.J., Jung, H., Lauf, R.J., Phelps, T.J. “Scalable economic extracellular synthesis of CdS nanostructured particles by a non-pathogenic thermophile” J. Ind. Microbiol. Biotechnol. 2013, 40, 1263-1271.
- Moon, J.-W., Ivanov, I.N., Joshi, P.C., Armstrong B.L., Wang, W., Jung, H., Rondinone, A.J., Jellison Jr., G.E., Meyer III, H.M. Jang, G.G., Meisner, R.A., Duty, C.E., Phelps, T.J. “Scalable production of microbially-mediated ZnS nanoparticles and application to functional thin films” Acta Biomater. 2014, 10, 4474-4483.
- Jang, G.G., Gresback, R.G., Ivanov, I.N., Meyer III, H.M., Kidder, M., Phelps, T.J., Graham, D.E., Moon, J.-W. “Size tunable elemental copper nanoparticles: extracellular synthesis by thermoanaerobic bacteria and capping molecules” J. Mater. Chem. C, 2015, 3, 644-650.
- Jang, G.G., Jacobs, C.B., Ivanov, I.N., Joshi, P.C., Meyer III, H.M., Kidder, M., Armstrong, B.L., Datskos, P.G., David E. Graham, D.E., Moon, J.-W. “In situ capping for size control of monochalcogenide (ZnS, CdS and SnS) nanocrystals produced by anaerobic metal-reducing bacteria” Nanotechnol. *In press.*
- Moon, J.-W., Phelps, T.J., Fitzgerald Jr., C.L., Lind, R.F., Jang, G.G., Joshi, P.C., Kidder, M., Elkins, J.G., Armstrong, B.L., Watkins, T.R., Graham, D.E. “Manufacturing demonstration of bio-zinc sulfide nanostructure using pilot-plant scaled NanoFermentation” Acta Biomater. (in preparation)
- Jung, H., Phelps, T.J., Rondinone, A.J., Jellison Jr., G.E., Duty, D.E., Moon, J.-W. Expandable one-pot process of water-soluble ZnS nanocrystals with the tailored size. Chem. Phys. Chem. (in preparation)

Presentations

- Moon, J.-W., Ivanov, I.N., Duty, C.E., Love, L.J., Wang, W., Li, Y.-L., Madden, A.S., Mosher, J.J., Suresh, A.K., Rondinone, A.J., Rawn, C.J., Lauf, R.J., Phelps, T.J. (2012) Bacterially precipitated nanoparticulate cadmium sulfide quantum dot production. The annual meeting of the American Society for Microbiology in June 16-19, San Francisco, CA.
- Moon, J.-W., Ivanov, I.N., Joshi, P.C., Jung, H., Rondinone, A.J., Jellison Jr., G.E., Armstrong, B.L., Jang, G.G. Wang, W., Duty, C.E., Phelps, T.J. (2014) Bioproduction of ZnS nanoparticles with copper doping for tunable emissions. General meeting of American Society of Microbiology, May 17-20, Boston, MA.
- Moon, J.-W., Ivanov, I.N., Joshi, P.C., Armstrong, B.L., Wang W., Jung, H., Rondinone, A.J., Jellison Jr., GE., Meyer III, H.M., Jang, G.G., Meisner, R.A., Duty, C.E., Phelps, T.J. (2014) Microbiologically produced ZnS nanoparticles and functional thin film for photovoltaic applications. Annual Meeting of Society of Industrial Microbiology and Biotechnology, July 20-24, St Louis, MO.
- Jang, G.G., Gresback, R.G., Ivanov, I.N., Meyer III, H.M., Kidder, M., Graham, D.E., Phelps, T.J. Moon, J.-W. Air-stable elemental copper nanoparticle synthesis by anaerobic bacteria controls size and enables scalability in aqueous solutions. 248th ACS National Meeting & Exposition, August 10-14, San Francisco, CA.
- Jang, G.G., Ivanov, I.N., Meyer III, H.M., Kidder, M., Graham, D.E., Moon, J.-W. (2014) Scalable process control of highly luminescent and environmentally friendly ZnS quantum dot synthesis by anaerobic bacteria in aqueous solutions. 14AlChE Annual Meeting, November 16-21, Atlanta, GA.

## 3.4 COMMERCIALIZATION

This project demonstrated a low temperature materials synthesis, called NanoFermentation, can be an alternative scalable green manufacturing process that requires low cost of raw materials and input energy for production. Related new invention disclosures were filed such as cost-saving and enhancing properties of final products. This technology was licensed by TopFive, Inc. on September 2014 and NanoElements LLC was established. The Low Temperature Materials Synthesis team won the 2014 Technology Commercialization Award from ORNL. Throughout the course of the Low Temperature Materials Synthesis project, the team has engaged in discussions and sharing of samples under Material Transfer Agreements with commercial teams.

## 3.5 RECOMMENDATIONS

- Scale-up and optimize two-phase NanoFermentation to reduce or modify surface coatings and produce new materials incompatible with bioreactors
- Optimize production without pH buffer to reduce organic coatings and lower cost
- Test new applications for substituted magnetite nanoparticles
- Evaluate NanoFermentation potential to capture critical materials from geothermal fluids and waste streams